

February 3, 2008 (submitted to ApJ November 28, 2007)

VARIATIONS OF THE MID-IR AROMATIC FEATURES INSIDE AND AMONG GALAXIES

Frédéric Galliano

*Observational Cosmology Lab., Code 665, NASA Goddard Space Flight Center, Greenbelt
MD 20910, USA*

Department of Astronomy, University of Maryland, College Park, MD 20742, USA

`galliano@astro.umd.edu`

Suzanne C. Madden

Service d'Astrophysique, L'Orme des Merisiers, CEA/Saclay, 91191 Gif-sur-Yvette, France

Alexander G. G. M. Tielens

NASA Ames Research Center, Mail Stop 245-3, Moffett Field, CA 94035, USA

Els Peeters

NASA Ames Research Center, Mail Stop 245-6, Moffett Field, CA 94035, USA

SETI Institute, 515 N. Whisman Rd, Mountain View, CA 94043, USA

*and Physics & Astronomy Dept., University of Western Ontario, PAB 213, London ON
N6A 3K7, Canada*

and

Anthony P. Jones

Institut d'Astrophysique Spatiale, Université de Paris XI, 91405 Orsay, France

ABSTRACT

We present the results of a systematic study of mid-IR spectra of Galactic regions, Magellanic H II regions, and galaxies of various types (dwarf, spiral, starburst), observed by the satellites *ISO* and *Spitzer*. We study the relative variations of the 6.2, 7.7, 8.6 and 11.3 μm features inside spatially resolved objects (such as M 82, M 51, 30 Doradus, M 17 and the Orion bar), as well as among

90 integrated spectra of 50 objects. Our main results are that the 6.2, 7.7 and 8.6 μm bands are essentially tied together, while the ratios between these bands and the 11.3 μm band varies by one order of magnitude. This implies that the properties of the PAHs are remarkably universal throughout our sample, and that the relative variations of the band ratios are mainly controlled by the fraction of ionized PAHs. In particular, we show that we can rule out both the modification of the PAH size distribution, and the mid-infrared extinction, as an explanation of these variations. Using a few well-studied Galactic regions (including the spectral image of the Orion bar), we give an empirical relation between the $I_{6.2}/I_{11.3}$ ratio and the ionization/recombination ratio $G_0/n_e \times \sqrt{T_{\text{gas}}}$, therefore providing a useful quantitative diagnostic tool of the physical conditions in the regions where the PAH emission originates. Finally, we discuss the physical interpretation of the $I_{6.2}/I_{11.3}$ ratio, on galactic size scales.

Subject headings: dust – HII regions – ISM: structure – galaxies: dwarf, starburst – infrared: general

1. INTRODUCTION

The reprocessing of stellar light by dust in the infrared (IR) is widely used to probe embedded star formation. However, in the absence of other constraints, the physical properties which can usually be derived from an almost-featureless grain continuum emission is limited to global quantities, such as the dust mass and its average temperature. The ubiquity of numerous mid-IR aromatic features, in a wide variety of astrophysical objects and environments, potentially provides more articulate diagnostics of the physical conditions. Indeed, these features dominate the mid-IR spectra of evolved stars (e.g. Blommaert et al. 2005; Kraemer et al. 2006), the cool ISM (e.g. Abergel et al. 2005; Flagey et al. 2006; Povich et al. 2007), as well as whole galaxies (e.g. Verma et al. 2005; Smith et al. 2007), that have been extensively observed by the *Infrared Space Observatory (ISO)*, and are currently investigated with a higher sensitivity by the *Spitzer Space Telescope*. In our Galaxy, one third of the stellar light is reprocessed by dust, while this fraction can go up to 99% and higher, in starburst galaxies. At solar metallicity, roughly 15% of the cooling is radiated through the most powerful mid-IR bands, centered at 3.3, 6.2, 7.7, 11.3 and 12.7 μm .

Historically, these emission features were attributed to very small grains ($\simeq 10 \text{ \AA}$), transiently heated by single photon absorption, in order to account for the independence of the color temperature with the distance from the illuminating star, in several reflection nebulae (Sellgren 1984). In parallel, the central wavelengths of these bands were recognized to

coincide with the vibrational modes of aromatic material (Duley & Williams 1981). These features are now commonly attributed to the molecular modes of Polycyclic Aromatic Hydrocarbons (hereafter PAHs; Léger & Puget 1984; Allamandola et al. 1985, 1989), which are planar molecules made of $\simeq 10$ to 1000 carbon atoms, excited primarily by ultraviolet (UV) photons. With silicate and carbon grains, PAHs are a main component of dust models (Désert et al. 1990; Dwek et al. 1997; Draine & Li 2001; Zubko et al. 2004). Their absorption efficiency has been modeled using astrophysical observations, laboratory measurements and quantum theory (in particular Désert et al. 1990; Joblin et al. 1992; Verstraete et al. 2001; Li & Draine 2001; Mattiorda et al. 2005a,b; Draine & Li 2007; Mallocci et al. 2007). In addition to being major radiative coolants of the interstellar medium (ISM), PAHs are responsible for most of the photoelectric heating of the gas in photodissociation regions (hereafter PDRs) and the neutral interstellar medium, due to their high cumulative surface area (e.g. Bakes & Tielens 1994; Hollenbach & Tielens 1997). For the same reason, they probably play an important role in grain surface chemistry (e.g. Tielens & Allamandola 1987). In our Galaxy, they contain $\simeq 15 - 20\%$ of the depleted carbon (Zubko et al. 2004, with solar abundance constraints). As a consequence, they are believed to be part of the interstellar carbon condensation chain (Cherchneff et al. 2000; Dartois et al. 2005).

From an extragalactic point of view, the luminosity of the $6.2\ \mu\text{m}$ feature can be used as a tracer of star formation (Peeters et al. 2004b). However, this tracer is biased by global parameters such as the ISM metallicity. Indeed, PAHs are underabundant in low-metallicity galaxies (e.g. Galliano et al. 2003, 2005, 2008; Draine et al. 2007). There is a general correlation between the PAH-to-continuum intensity ratio and the ISM metallicity (Madden et al. 2006; Wu et al. 2006; O’Halloran et al. 2006; Smith et al. 2007), and consequently between the $\text{IRAC}_{8\mu\text{m}}/\text{MIPS}_{24\mu\text{m}}$ broadband ratio and the metallicity (Engelbracht et al. 2005). The origin of this trend has been attributed to radiative and mechanical destruction mechanisms by Madden et al. (2006) and O’Halloran et al. (2006) respectively. Conversely, from the detailed modeling of the spectral energy distribution (SED) of nearby galaxies, Galliano et al. (2008) showed that the PAH-to-gas mass ratio at different metallicities coincides with the relative amount of carbon dust condensed in the envelopes of low-mass stars, during the Asymptotic Giant Branch phase (AGB). This study suggests that PAHs are injected into the ISM by their progenitors, the AGB stars, several hundreds of Myr after the beginning of the star formation, when the gas has already been enriched by more massive stars. This delay corresponds to the time needed for AGB stars to evolve off the main sequence. Therefore, the delayed injection of AGB-condensed carbon dust into the ISM offers a natural explanation for the paucity of PAHs in low-metallicity environments.

From a cosmological point of view, the large luminosity in these IR emission features coupled with the high sensitivity of *Spitzer* has allowed the detection of PAHs in distant

luminous infrared galaxies out to redshift $z \simeq 2$ (e.g. Elbaz et al. 2005; Yan et al. 2005; Houck et al. 2005). Hence, understanding what controls the properties of the aromatic features on large scales is required, in order to properly interpret broadband surveys.

The detailed characteristics of the mid-IR features, such as their shape, their central wavelength or the intensity ratio between the different bands are known to vary (see Peeters et al. 2004a). Such variations are essentially due to modifications of the molecular structure of the PAHs, in different astrophysical environments. In particular, since each feature is attributed to a given vibrational mode, the ratio between these features will vary with quantities such as the charge, the hydrogenation or the size and shape of the molecule. The $3.3 \mu\text{m}$ PAH band arises from the radiative relaxation of CH stretching modes, while the $11.3 \mu\text{m}$ feature originates in the CH out-of-plane bending modes; CC stretching modes are responsible for the features between 6 and $9 \mu\text{m}$; CH in plane bending excitation produces part of the $8.6 \mu\text{m}$ band. Now, laboratory studies and quantum calculations shows that the CC modes are intrinsically weak in neutral PAHs, and become stronger when the PAHs are ionized (Langhoff 1996; Allamandola et al. 1999; Bauschlicher 2002; Kim & Saykally 2002). Therefore, the 6 to $9 \mu\text{m}$ bands will be much more intense for a PAH^+ than for a PAH^0 , while it will be the opposite for the 3.3 and $11.3 \mu\text{m}$. Consequently, the ratios between the CC and the CH feature intensities depend on the charge of the PAHs, which is directly related to the physical conditions (e.g. intensity of the ionizing radiation field, electron density, etc.) in the environment where the emission is originating.

Evidence of variations between features in different astrophysical environments have been reported by many authors. For example, Joblin et al. (1996) showed that the $I_{8.6}/I_{11.3}$ ratio decreases with increasing distance from the exciting star, in the reflection nebulae NGC 1333 – where I_λ is the integrated intensity of the feature centered at $\lambda \mu\text{m}$. Hony et al. (2001) found a good correlation between the 3.3 and $11.3 \mu\text{m}$ CH bands, in a sample of Galactic H II regions, YSOs, and evolved stars, while they reported variations of $I_{6.2}/I_{11.3}$ by a factor of 5. The observations of Galactic and Magellanic H II regions, presented by Vermeij et al. (2002), indicate that the ratios $I_{6.2}/I_{11.3}$, $I_{7.7}/I_{11.3}$ and $I_{8.6}/I_{11.3}$ are correlated. Furthermore, they suggest a segregation between the values of these ratios in the Milky Way and those in the Magellanic Clouds. Bregman & Temi (2005) studied the variation of $I_{7.7}/I_{11.3}$ in three reflection nebulae. Assuming that this variation is controlled by the charge of the PAHs, they could relate this band ratio to the ratio G_0/n_e between the integrated intensity of the UV field, G_0 , and the electron density, n_e . Similarly, Compiègne et al. (2007), studying the detailed variations of the mid-IR spectrum in the Horsehead nebula, attributed the high relative strength of the $I_{11.3}$ feature to a high fraction of neutral PAHs, due to the high ambient electron density. On the contrary, Smith et al. (2007) studied the variation of $I_{7.7}/I_{11.3}$ coming from the nuclear regions of the SINGS legacy program galaxies. They

find that this ratio is relatively constant among pure starbursts, but varies by a factor of 5 among galaxies having a weak AGN. They interpret this effect as a selective destruction of the smallest PAHs by the hard radiation arising from the accretion disk, ruling out the explanation in terms of ionization of the molecules, in these particular environments. This interpretation is also supported by the high $11.3\ \mu\text{m}$ and the weakness of the $3.3\ \mu\text{m}$ band in the *AKARI* spectrum of the giant elliptical galaxy NGC 1316 (Kaneda et al. 2007).

The previous considerations stress the diversity of the possible interpretation of the mid-IR feature variations in galaxies. We need to identify the main physical processes controlling the PAH bands, if we are to use them as diagnostic tools. This is the aim of this paper. It presents a quantitative analysis of mid-IR spectra (*ISO* and *Spitzer*) of Galactic regions, low-metallicity dwarf galaxies, quiescent spirals, starbursts and AGNs. To achieve our goal, we focus on identifying the main trends between the various PAH features, at different spatial scales and in different environments. We then link these variations to the physical conditions inside the studied region. Preliminary results of this study were published in Galliano (2004, 2007).

The paper is organized as follows. In §2, we present our sample and the data reduction. We discuss the spectral decomposition of the mid-IR spectrum, in §3. The results of this decomposition are presented in §4; we study the various trends between the band ratios within galaxies, and among different types of environment. Then, in §5, we provide a physical interpretation of these trends, when the structure of the ISM is resolved, and when it is not. Finally, we summarize our conclusions in §6.

2. OBSERVATIONS AND DATA REDUCTION

2.1. The Sample

In order to systematically study the properties of the mid-IR aromatic features, we include in our sample a wide variety of Galactic regions and galaxies, covering a large range of metallicities and star formation activities. We merge the *ISO* samples of starbursts and AGNs presented by Laurent et al. (2000), spirals by Roussel et al. (2001), Magellanic regions and dwarfs by Madden et al. (2006), and complement them by low-metallicity sources observed with *Spitzer*. We add to this sample, the *ISO*/CAM spectra of several Galactic regions, like M 17 (Cesarsky et al. 1996b), NGC 2023 (Abergel et al. 2002), NGC 7027 (Persi et al. 1999) and the Orion bar (Cesarsky et al. 2000), and the *ISO*/SWS spectra ($2.5 - 45\ \mu\text{m}$) of several compact H II regions published by Peeters et al. (2002b). The SMC B1#1 spectrum is the one presented by Reach et al. (2000).

The global properties of the selected sources are presented in Table 1. If relevant, the distances were homogenised to $H_0 = 71 \ h^{-2} \text{ km s}^{-1} \text{ Mpc}^{-1}$.

Table 1. General properties of the sample.

Name	R.A. (J2000)	Dec. (J2000)	Aperture	Mid-IR spectrograph	Distance (Mpc)	12 + log(O/H) [ref.]	Category
Haro 11	00 ^h 36 ^m 52 ^s .5	−33°33′19″	10″	<i>Spitzer</i> /IRS	92	7.9	[2] Dwarf
SMC B1#1	00 ^h 45 ^m 33 ^s .0	−73°18′46″	84″ – 36″	<i>ISO</i> /CAM	0.06	8.0	[3] Magellanic
NGC 253	00 ^h 47 ^m 32 ^s .9	−25°17′18″	40″	<i>ISO</i> /CAM	3.3	9.0	[4] SB/AGN
NGC 253 p	00 ^h 47 ^m 32 ^s .9	−25°17′18″	10″	<i>ISO</i> /CAM	3.3	9.0	[4] SB/AGN
NGC 253 e	00 ^h 47 ^m 32 ^s .9	−25°17′18″	40″ – 10″	<i>ISO</i> /CAM	3.3	9.0	[4] SB/AGN
SMC N 66	00 ^h 59 ^m 02 ^s .0	−72°10′36″	120″	<i>ISO</i> /CAM	0.06	8.0	[3] Magellanic
NGC 520	01 ^h 24 ^m 34 ^s .9	+03°47′31″	30″	<i>ISO</i> /CAM	27	...	Dwarf
NGC 613	01 ^h 34 ^m 17 ^s .5	−29°24′58″	60″	<i>ISO</i> /CAM	19	9.2	[5] Spiral
NGC 613 p	01 ^h 34 ^m 17 ^s .5	−29°24′58″	20″	<i>ISO</i> /CAM	19	9.2	[5] Spiral
NGC 891	02 ^h 22 ^m 33 ^s .4	+42°20′57″	200″	<i>ISO</i> /CAM	9.6	8.9	[6] Spiral
NGC 1068	02 ^h 42 ^m 40 ^s .6	−00°00′47″	60″	<i>ISO</i> /CAM	15	9.0	[7] SB/AGN
NGC 1068 p	02 ^h 42 ^m 40 ^s .6	−00°00′47″	20″	<i>ISO</i> /CAM	15	9.0	[7] SB/AGN
NGC 1068 e	02 ^h 42 ^m 40 ^s .6	−00°00′47″	60″ – 20″	<i>ISO</i> /CAM	15	9.0	[7] SB/AGN
NGC 1097	02 ^h 46 ^m 19 ^s .1	−30°16′28″	100″	<i>ISO</i> /CAM	12	9.0	[8] Spiral
NGC 1097 p	02 ^h 46 ^m 19 ^s .1	−30°16′28″	40″	<i>ISO</i> /CAM	12	9.0	[8] Spiral
NGC 1140	02 ^h 54 ^m 33 ^s .5	−10°01′44″	20″	<i>ISO</i> /CAM	25	8.0	[9] Dwarf
NGC 1365	03 ^h 33 ^m 35 ^s .6	−36°08′23″	100″	<i>ISO</i> /CAM	19	9.1	[10] Spiral
NGC 1365 p	03 ^h 33 ^m 35 ^s .6	−36°08′23″	40″	<i>ISO</i> /CAM	19	9.1	[10] Spiral
NGC 1365 e	03 ^h 33 ^m 35 ^s .6	−36°08′23″	100″ – 40″	<i>ISO</i> /CAM	19	9.1	[10] Spiral
IC 342	03 ^h 46 ^m 49 ^s .7	+68°05′45″	40″	<i>ISO</i> /CAM	3.8	8.9	[11] SB/AGN
IC 342 p	03 ^h 46 ^m 49 ^s .7	+68°05′45″	12″	<i>ISO</i> /CAM	3.8	8.9	[11] SB/AGN
IC 342 e	03 ^h 46 ^m 49 ^s .7	+68°05′45″	40″ – 12″	<i>ISO</i> /CAM	3.8	8.9	[11] SB/AGN
IC 342 map	03 ^h 46 ^m 49 ^s .7	+68°05′45″	3″	<i>ISO</i> /CAM	3.8	8.9	[11] SB/AGN
NGC 1569	04 ^h 30 ^m 49 ^s .1	+64°50′52″	120″	<i>ISO</i> /CAM	2.2	8.2	[12] Dwarf
NGC 1569 e	04 ^h 30 ^m 49 ^s .1	+64°50′52″	120″ – 12″	<i>ISO</i> /CAM	2.2	8.2	[12] Dwarf
NGC 1808	05 ^h 07 ^m 42 ^s .3	−37°30′47″	50″	<i>ISO</i> /CAM	11	9.1	[13] SB/AGN
Orion bar D8	05 ^h 35 ^m 18 ^s .2	−05°24′40″	14″ × 20″	<i>ISO</i> /SWS	475 pc	...	H II region
Orion bar D5	05 ^h 35 ^m 19 ^s .8	−05°25′10″	14″ × 20″	<i>ISO</i> /SWS	475 pc	...	H II region
Orion bar D2	05 ^h 35 ^m 21 ^s .4	−05°25′40″	14″ × 20″	<i>ISO</i> /SWS	475 pc	...	H II region
Orion bar	5 ^h 35 ^m 20 ^s .0	−05°25′20″	6″	<i>ISO</i> /CAM	475 pc	...	PDR
30 Doradus	05 ^h 38 ^m 34 ^s .0	−69°05′57″	120″	<i>ISO</i> /CAM	0.05	8.4	[3] Magellanic
30 Doradus p	05 ^h 38 ^m 34 ^s .0	−69°05′57″	40″	<i>ISO</i> /CAM	0.05	8.4	[3] Magellanic
30 Doradus e	05 ^h 38 ^m 34 ^s .0	−69°05′57″	120″ – 40″	<i>ISO</i> /CAM	0.05	8.4	[3] Magellanic
30 Doradus map	05 ^h 38 ^m 34 ^s .0	−69°05′57″	6″	<i>ISO</i> /CAM	0.05	8.4	[3] Magellanic
NGC 2023	05 ^h 41 ^m 38 ^s .3	−02°16′33″	14″ × 20″	<i>ISO</i> /SWS	475 pc	...	PDR
II Zw 40	05 ^h 55 ^m 42 ^s .7	+03°23′29″	24″	<i>ISO</i> /CAM	10	8.1	[14] Dwarf

Table 1—Continued

Name	R.A. (J2000)	Dec. (J2000)	Aperture	Mid-IR spectrograph	Distance (Mpc)	12 + log(O/H) [ref.]	Category
He 2-10	08 ^h 36 ^m 15 ^s .2	−26°24′34″	10″	<i>Spitzer</i> /IRS	8.7	8.9	[12] Dwarf
M 82	09 ^h 55 ^m 51 ^s .8	+69°40′46″	90″	<i>ISO</i> /CAM	3.6	9.0	[15] SB/AGN
M 82 p	09 ^h 55 ^m 51 ^s .8	+69°40′46″	24″	<i>ISO</i> /CAM	3.6	9.0	[15] SB/AGN
M 82 e	09 ^h 55 ^m 51 ^s .8	+69°40′46″	90″ − 24″	<i>ISO</i> /CAM	3.6	9.0	[15] SB/AGN
M 82 map	09 ^h 55 ^m 51 ^s .8	+69°40′46″	3″	<i>ISO</i> /CAM	3.6	9.0	[15] SB/AGN
NGC 3256	10 ^h 27 ^m 51 ^s .1	−43°54′17″	24″	<i>ISO</i> /CAM	37	8.9	[16] SB/AGN
NGC 3256 p	10 ^h 27 ^m 51 ^s .1	−43°54′17″	10″	<i>ISO</i> /CAM	37	8.9	[16] SB/AGN
NGC 3256 e	10 ^h 27 ^m 51 ^s .1	−43°54′17″	24″ − 10″	<i>ISO</i> /CAM	37	8.9	[16] SB/AGN
Mrk 33	10 ^h 32 ^m 31 ^s .9	+54°24′04″	10″	<i>Spitzer</i> /IRS	20	8.4	[16] Dwarf
Arp 299	11 ^h 28 ^m 31 ^s .0	+58°33′39″	24″	<i>ISO</i> /CAM	41	...	SB/AGN
UM 448	11 ^h 42 ^m 12 ^s .4	+00°20′03″	10″	<i>Spitzer</i> /IRS	70	8.0	[17] Dwarf
IR 12331	12 ^h 36 ^m 01 ^s .9	−61°51′04″	14″ × 20″	<i>ISO</i> /SWS	4.5 kpc	...	H II region
NGC 4945	13 ^h 05 ^m 26 ^s .2	−49°28′15″	60″	<i>ISO</i> /CAM	3.9	...	SB/AGN
NGC 4945 p	13 ^h 05 ^m 26 ^s .2	−49°28′15″	20″	<i>ISO</i> /CAM	3.9	...	SB/AGN
NGC 4945 e	13 ^h 05 ^m 26 ^s .2	−49°28′15″	60″ − 20″	<i>ISO</i> /CAM	3.9	...	SB/AGN
Centaurus A	13 ^h 25 ^m 28 ^s .0	−43°01′06″	30″	<i>ISO</i> /CAM	3.8	~ 9	[18] SB/AGN
Centaurus A e	13 ^h 25 ^m 28 ^s .0	−43°01′06″	10″	<i>ISO</i> /CAM	3.8	~ 9	[18] SB/AGN
M 51	13 ^h 29 ^m 52 ^s .7	+47°11′43″	140″	<i>ISO</i> /CAM	8.4	8.7	[19] Spiral
M 51 p	13 ^h 29 ^m 52 ^s .7	+47°11′43″	60″	<i>ISO</i> /CAM	8.4	8.7	[19] Spiral
M 51 e	13 ^h 29 ^m 52 ^s .7	+47°11′43″	140″ − 60″	<i>ISO</i> /CAM	8.4	8.7	[19] Spiral
M 51 map	13 ^h 29 ^m 52 ^s .7	+47°11′43″	6″	<i>ISO</i> /CAM	8.4	8.7	[19] Spiral
M 83	13 ^h 37 ^m 00 ^s .7	−29°51′58″	200″	<i>ISO</i> /CAM	4.5	9.2	[20] Spiral
M 83 p	13 ^h 37 ^m 00 ^s .7	−29°51′58″	50″	<i>ISO</i> /CAM	4.5	9.2	[20] Spiral
M 83 e	13 ^h 37 ^m 00 ^s .7	−29°51′58″	200″ − 50″	<i>ISO</i> /CAM	4.5	9.2	[20] Spiral
M 83 map	13 ^h 37 ^m 00 ^s .7	−29°51′58″	6″	<i>ISO</i> /CAM	4.5	9.2	[20] Spiral
Circinus	14 ^h 13 ^m 09 ^s .6	−65°20′21″	40″	<i>ISO</i> /CAM	4.0	...	SB/AGN
Circinus e	14 ^h 13 ^m 09 ^s .6	−65°20′21″	40″ − 10″	<i>ISO</i> /CAM	4.0	...	SB/AGN
Arp 220	15 ^h 34 ^m 57 ^s .2	+23°30′11″	20″	<i>ISO</i> /CAM	73	...	ULIRG
Arp 220 p	15 ^h 34 ^m 57 ^s .2	+23°30′11″	10″	<i>ISO</i> /CAM	73	...	ULIRG
IR 15384	15 ^h 42 ^m 17 ^s .1	−53°58′31″	14″ × 20″	<i>ISO</i> /SWS	2.7 kpc	...	H II region
NGC 6240	16 ^h 52 ^m 58 ^s .8	+02°24′06″	20″	<i>ISO</i> /CAM	98	...	SB/AGN
NGC 6240 p	16 ^h 52 ^m 58 ^s .8	+02°24′06″	10″	<i>ISO</i> /CAM	98	...	SB/AGN
M 17 map	18 ^h 20 ^m 22 ^s .0	−16°12′40″	6″	<i>ISO</i> /CAM	1.5 kpc	...	PDR
IR 18317	18 ^h 34 ^m 24 ^s .9	−07°54′47″	14″ × 20″	<i>ISO</i> /SWS	4.9 kpc	...	H II region
NGC 6946	20 ^h 34 ^m 51 ^s .2	+60°09′17″	140″	<i>ISO</i> /CAM	5.5	9.1	[21] Spiral
NGC 6946 p	20 ^h 34 ^m 51 ^s .2	+60°09′17″	40″	<i>ISO</i> /CAM	5.5	9.1	[21] Spiral

Table 1—Continued

Name	R.A. (J2000)	Dec. (J2000)	Aperture	Mid-IR spectrograph	Distance (Mpc)	12 + log(O/H) [ref.]	Category
NGC 6946 e	20 ^h 34 ^m 51 ^s .2	+60°09′17″	140″ – 40″	<i>ISO/CAM</i>	5.5	9.1 [21]	Spiral
NGC 7027	21 ^h 07 ^m 01 ^s .7	+42°14′09″	14″ × 20″	<i>ISO/SWS</i>	700 pc	...	PDR
IR 22308	22 ^h 32 ^m 45 ^s .9	+58°28′21″	14″ × 20″	<i>ISO/SWS</i>	5.5 kpc	...	H II region
IR 23030	23 ^h 05 ^m 10 ^s .6	+60°14′41″	14″ × 20″	<i>ISO/SWS</i>	5.2 kpc	...	H II region
IR 23133	23 ^h 15 ^m 31 ^s .4	+61°07′08″	14″ × 20″	<i>ISO/SWS</i>	5.5 kpc	...	H II region
IR 23128	23 ^h 15 ^m 46 ^s .0	−59°03′17″	20″	<i>ISO/CAM</i>	180	...	SB/AGN
IR 23128 p	23 ^h 15 ^m 46 ^s .0	−59°03′17″	10″	<i>ISO/CAM</i>	180	...	SB/AGN
NGC 7714	23 ^h 36 ^m 14 ^s .1	+02°09′19″	10″	<i>Spitzer/IRS</i>	37	8.5 [22]	Dwarf

References. — [2] Bergvall et al. (2000); [3] Dufour et al. (1982); [4] Zaritsky et al. (1994); [5] Alloin et al. (1979); [6] Otte et al. (2001); [7] Dutil & Roy (1999); [8] Storchi-Bergmann et al. (1995); [9] Heckman et al. (1998); [10] Roy & Walsh (1997); [11] Pilyugin et al. (2004); [12] Kobulnicky & Skillman (1997); [13] Ravindranath & Prabhu (2001); [14] Pérez-Montero & Díaz (2003); [15] Boselli et al. (2002); [16] Mas-Hesse & Kunth (1999); [17] Izotov & Thuan (1998); [18] Schaerer et al. (2000); [19] Bresolin et al. (2004); [20] Webster & Smith (1983); [21] Kobulnicky & Johnson (1999); [22] Gonzalez-Delgado et al. (1995).

Note. — The sources are ordered according to their right ascension. For *ISO/CAM* sources, the apertures are circular, centered on the coordinates listed in the second and third columns. For *ISO/SWS* sources, the beam is 14″ × 20″ (bands 1 and 2). The diameter of the aperture is given in the fourth column. When the diameter has the form $\theta_1'' - \theta_2''$, it means that we subtracted from the flux in the circular aperture of diameter θ_1'' , the flux in a concentric circular aperture of diameter $\theta_2'' < \theta_1''$. The sources which are followed by “map” are those for which the signal-to-noise of the spectral-image is good; in this case, the aperture refers to the pixel field of view. The letter after the name of the source designates the type of aperture: when there is no letter, most of the emission of the object is encompassed in the aperture; “p” is for peak emission; “e” for extended emission.

2.2. *ISO*/CAM Data Reduction

Most of the sources in Table 1 were observed with *ISO*/CAM (Cesarsky et al. 1996a) on board the *ISO* satellite (Kessler et al. 1996). We refer to the work of Madden et al. (2006) for a detailed description of the data reduction applied to all of the *ISO*/CAM data used in this study. The CVF performed spectral imaging using a 32×32 detector array, with a sampling of $3''\text{pixel}^{-1}$ or $6''\text{pixel}^{-1}$ in our cases, from $\lambda = 5 \mu\text{m}$ to $16.5 \mu\text{m}$ with one pointing of two CVFs, from $\lambda = 5$ to $9.5 \mu\text{m}$ and from $\lambda = 9.0$ to $16.5 \mu\text{m}$. The spectral resolution increases from $\lambda/\Delta\lambda = 35$ to 51 across the full spectra.

For the *ISO* data treatment, we used the CAM Interactive Reduction (CIR, version AUG01; Chaniel 2003). The subtraction of the dark currents was performed using the Biviano et al. (1998) model which predicts the time evolution for each row of the detector, taking into account drifts along each orbit and each revolution. We masked the glitches using multi-resolution median filtering (Starck et al. 1999) on each block of data after slicing the cube. Additional deglitching was performed manually, examining the temporal cut for each pixel. We corrected the systematic memory effects using the Fouks-Schubert method (Coulais & Abergel 2000). We computed a hybrid flat-field image placing a mask on the source and computing a flat field outside this mask from the median of the temporal cut for each pixel. For the pixels which were on-source, the flat-field response was set to the corresponding calibration flat-field. The conversion from Analog to Digital Units to mJy/pixel was performed using the standard in-flight calibration data base. To remove the sky contribution, sources smaller than the array were masked and, for a given wavelength, the median of the pixels which are off-source were subtracted from each pixel. For the more extended sources, we subtracted an independently observed zodiacal spectrum. The contribution of this spectrum was a free parameter varied in order to match the properly sky subtracted fluxes in the LW2 ($6.7 \mu\text{m}$) and LW3 ($14.3 \mu\text{m}$) broadbands. The final product is a 3D spectral-image. We integrated the spectrum using an aperture encompassing the entire galaxy, and obtained a 1D spectrum. When the angular size of the source was larger than the array, we scaled the spectrum by matching *IRAS*_{12 μm} broadband flux with that derived from convolving the spectrum with the *IRAS*_{12 μm} bandpass.

2.3. *Spitzer*/IRS Spectrum Extraction

Several of the low-metallicity sources in Table 1 were not observed by *ISO*/CAM, thus we complemented our database with mid-IR spectra from the *Spitzer*/IRS spectrometer (Houck et al. 2004b) on board the *Spitzer Space Telescope* (Werner et al. 2004), when these data were released. Among these galaxies, the spectrum of SBS 0335-052 has been published

by Houck et al. (2004a), NGC 7714 by Brandl et al. (2004), NGC 5253 by Beirão et al. (2006), Haro 11 and I Zw 18 by Wu et al. (2006). We refer to these studies for a detailed presentation of their mid-IR properties. We considered only low-resolution data, taken with the SL (Short-Low) module, from $\lambda = 5.2 \mu\text{m}$ to $14.5 \mu\text{m}$, and the LL (Long-Low) module, from $\lambda = 14.0 \mu\text{m}$ to $38.0 \mu\text{m}$, both with a spectral resolution of $\lambda/\Delta\lambda \simeq 64 - 128$.

We retrieved the Basic Calibrated Data (BCD) that have been preprocessed by the Spitzer Science Center (SSC) data reduction pipeline. They have been converted to flux density, corrected for stray light and flatfielded. The extraction of the spectra from the 2D space/wavelength images was performed with the Spectral Modeling, Analysis and Reduction Tool (SMART, version 5.5.6; Higdon et al. 2004). We first inspected the BCD images and identified the hot pixels which had not been masked out by the SSC. We replaced them by the median of their neighbors. For each module, one order is on-source and the other is off-source, at a time. Then the positions are switched. We subtracted the off-source spectrum from that of the source, in order to remove the sky emission. The extraction of the 1D spectrum was performed inside a column whose width varies with wavelength. We have excluded the bonus order. Then, the various frames, for each nod position, were coadded. Since the long wavelength end of the SL module and the short wavelength end of the LL module were not systematically overlapping, we finally scaled the SL module, in order to obtain a continuous spectrum. This scaling factor can be as large as 50%. At the time of this publication, the *Spitzer*/IRS data handbook recommends that the signal to noise ratio not be derived from the uncertainties generated by the pipeline. Instead, we adopted the recommended systematic error of 20%. To take into account these statistical variations, we smoothed the spectra into a $\Delta\lambda \simeq 0.2 \mu\text{m}$ window (4 points), and took the standard deviation inside this window as the error. As we did with the *ISO*/CAM spectra (§2.2), in order to compensate for the fact that we may be overlooking some extended emission, we scaled the spectrum to match the *IRAS*_{12 μm} and *IRAS*_{25 μm} . In the case of II Zw 40, the *Spitzer*/IRS spectrum does not exhibit the PAH features that Madden et al. (2006) detected in the extended emission, since the *Spitzer*/IRS observations were conducted in staring mode. Indeed, this *Spitzer*/IRS observation does not encompass the region where the tail was detected. Thus we prefer to use the *ISO*/CAM data for this galaxy.

3. THE SPECTRAL DECOMPOSITION METHODS

3.1. Inventory of the Physical Components

We restrain our study to the spectral range $5 - 16 \mu\text{m}$, since it is the overlap between the various data sets we have compiled. The main physical components contributing at these

wavelengths are the following.

- The ionic gas emits strong fine-structure ionic lines. The $[\text{Ne III}]_{15.56\mu\text{m}}$, $[\text{Ne II}]_{12.81\mu\text{m}}$, $[\text{S IV}]_{10.51\mu\text{m}}$, $[\text{Ar III}]_{8.99\mu\text{m}}$ and $[\text{Ar II}]_{6.98\mu\text{m}}$ are the brightest lines.
- Several ubiquitous broad features, originating from the molecular modes of stochastically heated PAH molecules. The most prominent of them are centered at 6.2, 7.7, 8.6, 11.3 and 12.7 μm . The $[\text{Ne II}]_{12.81\mu\text{m}}$ line is blended with the 12.7 μm feature.
- Very small grains (VSG), fluctuating in temperature around a few hundred degrees Kelvin, produce a continuum emission. In addition, hot grains in H II regions, at thermal equilibrium with the radiation field, may contribute to this continuum.
- The extinction feature at 9.7 μm , attributed to amorphous silicates, can be seen toward the most embedded sources.
- Molecular lines are also present, especially the H_2 0-0 S(3) $_{9.7\mu\text{m}}$ line. However, they are much weaker than the other components.

Fig. 1 shows the variations of the aromatic feature spectrum among galaxies (top panel), inside one galaxy (middle panel) and from a theoretical point of view (bottom panel). This figure shows that the 6.2, 7.7 and 8.6 μm features are qualitatively tied together, and that most of the variations in the mid-IR aromatic spectrum is a variation of these three features relative to the 11.3 μm band. The lower panel of Fig. 1 suggests that most of these variations could be explained by a variation of the neutral-to-cationic-PAH ratio. In what follows, we quantify these variations in our sample, in order to explore the validity of this explanation.

3.2. Measuring the Intensity of the Aromatic Features

Measuring the intensity of the aromatic features is uncertain, due to the intrinsic width ($\Delta\lambda \simeq 1 \mu\text{m}$) and the complexity of the band profiles. Indeed, contrary to gas lines, a large fraction of the energy of the PAH bands is radiated in the *wings*. These wings extend far outside of the central wavelength and can be difficult to reliably disentangle from the underlying continuum emission. Therefore, a proper extraction of the feature requires an assumed band profile. However, the actual profile of each band is not known. It is asymmetric and varies as a function of environment (e.g. Peeters et al. 2002a; van Dienenhoven et al. 2004). Consequently, several profiles have been used in the literature, motivated by different physical arguments. For example, Boulanger et al. (1998) proposed that the width of the band is a consequence of the continuous redistribution of intramolecular vibrational energy,

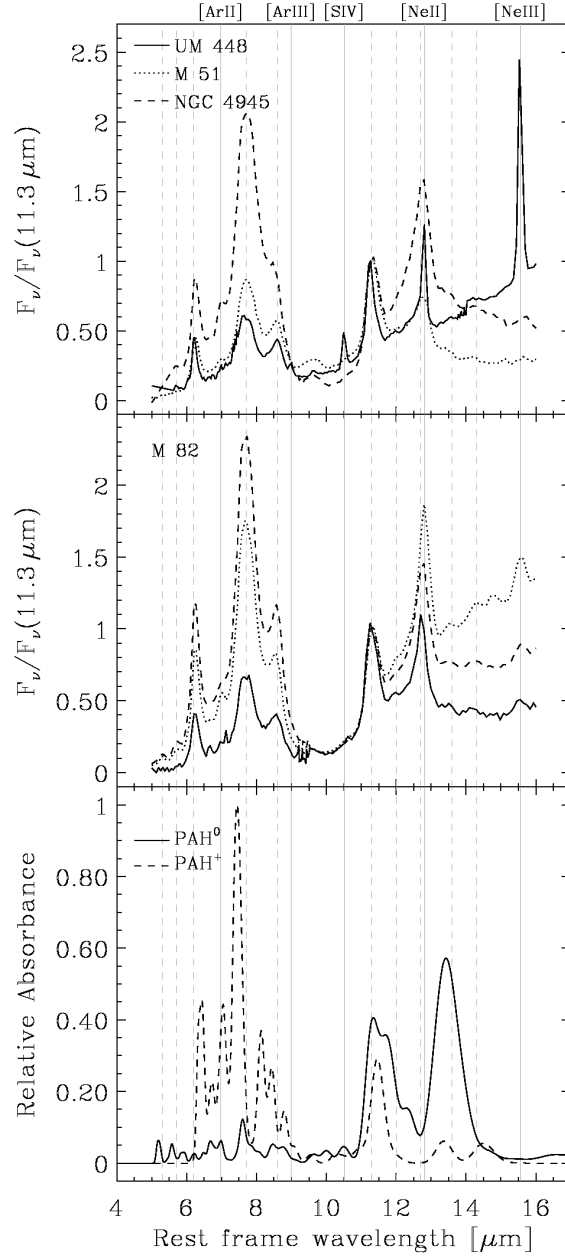


Fig. 1.— Various spectra normalized to the 11.3 μm feature. The top panel shows the total integrated spectra of a low-metallicity galaxy (UM 448), a normal spiral (M 51), and a LIRG (NGC 4945). The middle panel shows the spectra of three different regions inside the starburst galaxy M 82. The bottom panel shows, for comparison, the absorption coefficient of neutral and cationic PAHs measured in laboratory by Allamandola et al. (1999). The solid vertical lines mark the wavelengths of the brightest lines, and the dashed vertical lines mark the wavelengths of the major bands. In this figure and in what follows, $F_\nu(\lambda)$ is the monochromatic flux density at wavelength λ μm .

between different excitation levels, at high temperature. They estimated the transition timescales to be $\lesssim 10^{-13}$ s, and showed that the PAH bands were well represented by Lorentzian profiles. Conversely, a Drude profile was used by Li & Draine (2001). Such a profile describes the electric permeability in a solid or a large molecule. Finally, numerous studies simply measure the tip of the aromatic band, and assumes that the total flux radiated in the band scales with this quantity.

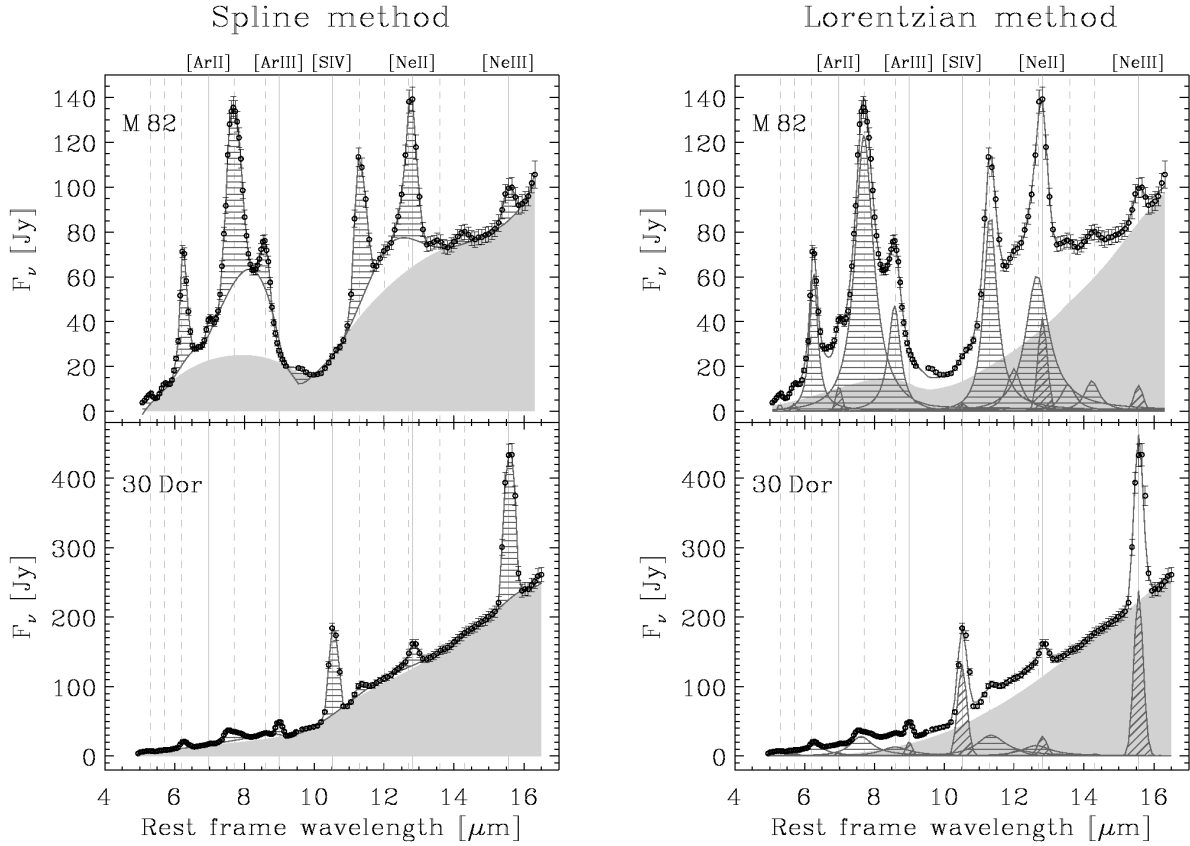


Fig. 2.— Demonstration of the two spectral decomposition methods for the total spectrum of M 82 and 30 Doradus.

In order to take into account the uncertainty of the actual shape of the aromatic bands, we systematically analysed our spectra using two different spectral decomposition methods. These two methods differ in the way the continuum and the aromatic bands are fitted. They are demonstrated in Fig. 2, on a PAH-rich spectrum (M 82), and PAH-poor one (30 Doradus).

The *Spline method* (hereafter identified by the letter \mathcal{S}), used e.g. by Hony et al. (2001) and Vermeij et al. (2002), takes into account only the tip of the aromatic bands when

computing their intensities, as shown in left panels of Fig. 2. The continuum (grey filled curve) is fitted with a spline function, constrained at the wavelengths $\lambda = 5.04, 5.47, 5.84, 9.18, 10.85, 13.82, 14.60, 15.08, 16.00, 16.15 \mu\text{m}$. A second spline function is fitted to the spectrum, corresponding to the previous continuum, plus the “plateau” under the 6.2, 7.7 and 8.6 μm bands, and the plateau under the 11.3 and 12.7 μm bands. In addition to the previous wavelengths, this spline function is also constrained at $\lambda = 6.61, 6.80, 7.13, 8.24, 8.80, 11.85, 12.20, 13.22 \mu\text{m}$. The difference between the total spectrum and this continuum+plateau component defines the lines and features (line filled areas of the left panels of Fig. 2). This method is relatively robust. However, it does not allow us to separate the $[\text{Ne II}]_{12.81\mu\text{m}}$ from the 12.7 μm band (most of our spectra have a low spectral resolution).

The Lorentzian method (hereafter identified by the letter \mathcal{L}), used e.g. by Boulanger et al. (1998), Laurent et al. (2000) and Verstraete et al. (2001), assumes that the aromatic bands have lorentz profiles. The wings of these lorentzians account for the underlying plateau. A variation of this method, implemented by Smith et al. (2007), consists of modeling the PAH features with Drude profiles. We proceed as following.

1. The $[\text{Ne III}]_{15.56\mu\text{m}}$, $[\text{Ne II}]_{12.81\mu\text{m}}$, $[\text{S IV}]_{10.51\mu\text{m}}$, $[\text{Ar III}]_{8.99\mu\text{m}}$, and $[\text{Ar II}]_{6.98\mu\text{m}}$ ionic lines are fitted with gaussian functions (diagonal line filling in the right panels of Fig. 2). For each (number i) of the N_{line} lines, the central frequency, ν_i^{line} , is fixed, the width is fixed by the spectral resolution of the instrument, $\Delta\nu_{\text{spectro}}$, and the total flux of each line, F_i^{line} , is the free parameter.
2. The PAH bands are fitted with lorentzian functions (horizontal line filling in the right panels of Fig. 2). The considered features are centered at: $\lambda = 5.3, 5.7, 6.2, 7.7, 8.6, 11.3, 12.0, 12.7, 13.6$ and $14.3 \mu\text{m}$. For each (number i) of the N_{band} band, the central frequency, ν_i^{band} , the width, $\Delta\nu_i^{\text{band}}$, and the total flux, F_i^{band} , are the free parameters. We emphasize the fact that we fit only one band around 7.7 μm , where there are actually two bands centered at 7.6 μm and 7.8 μm . We proceed this way, in order to keep the number of parameters reasonably low. We will use the variation of the centroid of the 7.7 μm feature, noted $\lambda_{7.7}$, as an indicator of the 7.6 μm to 7.8 μm ratio.
3. The VSG continuum is fitted with the sum of N_{cont} modified black-bodies having the absorption efficiency, $Q_{\text{abs}}(\nu)$, of graphite in the Rayleigh approximation (grey filled area on the right panels of Fig. 2; Laor & Draine 1993). The temperatures, T_i^{cont} , and the total fluxes, F_i^{cont} , are the free parameters. We adopt $N_{\text{cont}} = 2$.
4. The sum of the previous components is multiplied by $\exp(-\tau)$, where $\tau(\nu)$ is the Mathis (1990) extinction law, with the Dudley & Wynn-Williams (1997) silicate

features. The column density is the only free parameter.

All these components are fitted simultaneously as part of one mathematical function:

$$F_\nu(\nu) = (F_\nu^{\text{line}}(\nu) + F_\nu^{\text{band}}(\nu) + F_\nu^{\text{cont}}(\nu)) \times \exp(-\tau(\nu)), \quad (1)$$

with:

$$\left\{ \begin{array}{l} F_\nu^{\text{line}}(\nu) = \sum_{i=1}^{N_{\text{line}}} F_i^{\text{line}} \sqrt{\frac{2}{\pi \Delta \nu_{\text{spectro}}^2}} \exp\left(-2 \frac{(\nu - \nu_i^{\text{line}})^2}{\Delta \nu_{\text{spectro}}^2}\right) \\ F_\nu^{\text{band}}(\nu) = \sum_{i=1}^{N_{\text{band}}} F_i^{\text{band}} \frac{1}{2\pi} \frac{\Delta \nu_i^{\text{band}}}{(\nu - \nu_i^{\text{band}})^2 + (\Delta \nu_i^{\text{band}}/2)^2} \\ F_\nu^{\text{cont}}(\nu) = \sum_{i=1}^{N_{\text{cont}}} F_i^{\text{cont}} \frac{B_\nu(T_i^{\text{cont}}, \nu) Q_{\text{abs}}(\nu)}{\int_{c/(16 \mu\text{m})}^{c/(10 \mu\text{m})} B_\nu(T_i^{\text{cont}}, \nu) Q_{\text{abs}}(\nu) d\nu}, \end{array} \right. \quad (2)$$

the various F_ν being the monochromatic flux densities. An advantage of the *Lorentzian method* over the *Spline method* is that it allows us to separate the $[\text{Ne II}]_{12.81\mu\text{m}}$ line and the $12.7 \mu\text{m}$ feature, and to study the variations of the centroids of the bands. However, when the PAH-to-VSG ratio is very low, as in the case of 30 Doradus (Fig. 2), the width of the features is more uncertain.

In both cases, I_{cont} is defined as the integrated intensity of the continuum between 10 and $16 \mu\text{m}$, and I_{PAH} , the sum of the intensities of all the bands between 5 and $16 \mu\text{m}$. We emphasize that our methods work automatically, without any *by eye* adjustment. This condition prevents systematic effects that could result from arbitrary choices of parameters. These two methods are orthogonal but give similar trends (see §4 and Smith et al. 2007). The *Spline method* is clearly continuum-biased in its assumptions whereas the *Lorentzian method* is a line-biased assumption method.

Our two methods can be applied to an integrated spectrum, or to each pixel of a spectro-image, provided that the signal-to-noise ratio is sufficient. We have systematically applied the two methods to all the spectra presented in Table 1. In our analysis, we will systematically consider the results of the two methods before drawing conclusions on the PAH properties.

4. SYSTEMATIC ANALYSIS OF THE MAJOR BAND RATIOS

4.1. Correlations Exhibited Among Integrated Spectra

Figs. 3-4 show select correlations between band ratios of the integrated spectra of our sample (Table 1), obtained with the two methods presented in §3.2. We focus on the four brightest bands at 6.2, 7.7, 8.6 and 11.3 μm , and study the correlations between the various ratios. The intensities of the features are reported in App. A (Table 4), and the parameters of the various correlations are given in Table 2. As mentioned in §3.2, the two methods are uncertain for very low values of the PAH-to-VSG ratio. Thus we define two subgroups of data.

1. The data that we consider to be reliable are marked with black symbols in Figs. 3-4. We define them as the measurements which have a signal-to-noise ratio, at $\lambda = 7.7 \mu\text{m}$, larger than 6, and $I_{\text{PAH}}/I_{\text{cont}} \geq 0.5$ with the *Lorentzian method*, and $I_{\text{PAH}}/I_{\text{cont}} \geq 0.3$ with the *Spline method*.
2. The fits that we consider to be less certain are the complementary data (grey symbols in Figs. 3-4), having lower signal-to-noise and PAH-to-VSG ratios.

Fig. 3 shows that there is an excellent linear correlation between the ratios $I_{6.2}/I_{11.3}$, $I_{7.7}/I_{11.3}$ and $I_{8.6}/I_{11.3}$, using either of the two methods. The variations of these ratios spread roughly over one order of magnitude, while the ratios $I_{6.2}/I_{7.7}$, and $I_{7.7}/I_{8.6}$ are roughly constant within the error bars (Fig. 4). In general, the measure of the intensity of the 8.6 μm band is less accurate than for the other main bands. Indeed, it is less intense than the 6.2 and 7.7 μm features. In addition, it is merged with the long wavelength wing of the 7.7 μm band. Finally, this particular feature is significantly affected by the silicate extinction feature around 9.7 μm , when the source is deeply embedded. This extinction is not corrected in the case of the *Spline method*, and is corrected very simply in the case of the *Lorentzian method*. That is the reason why correlations involving the 8.6 μm feature are always more dispersed than the others. Quantitatively, the correlation coefficients are around 0.8 for the four panels of Fig. 3, except for that involving the $I_{8.6}$ feature, with the *Spline method*. Most of the outsiders are based on fits that we consider to be uncertain.

Fig. 5 shows the consistency between the two methods. It demonstrates that, whatever method we use to measure the band ratios, the order of the various measures is conserved; i.e. a spectrum \mathcal{A} having a lower $I_{6.2}/I_{11.3}$ ratio than a spectrum \mathcal{B} , using the *Spline method*, will also have a lower ratio than \mathcal{B} using the *Lorentzian method*. Moreover, the fact that both methods give similar trends means that we did not artificially incorporate part of the

continuum flux within the aromatic band intensities. Indeed, it is possible to accidentally account for a fraction of the continuum intensity within the wings of the PAH profile, with the *Lorentzian method*, especially within the $11.3\ \mu\text{m}$ feature. However, this bias is not possible with the *Spline method*, since it integrates only the tip of the band. Therefore, the agreement between the two methods allow us to rule out this bias and claim that the trends of Fig. 3 are not induced by the fitting methods.

These first relations, established on integrated spectra, indicate that the properties of the PAHs throughout different types of galaxies and Galactic regions are remarkably homogeneous. They are consistent with a significant variation of the 6.2 , 7.7 and $8.6\ \mu\text{m}$ features relative to the $11.3\ \mu\text{m}$ band, coupled with an absence of significant variations among the 6.2 , 7.7 and $8.6\ \mu\text{m}$ bands.

Finally, as a consistency check, Fig. 6 shows the variations of the band ratios as a function of distance. The correlation coefficient is 0.23 for the *Lorentzian method*, and 0.20 for the *Spline method*. This absence of correlation shows the uniformity of the sample and rules out the possibility of variations induced by aperture effects.

4.2. Spatial Variations of the Band Properties

We now study the spatial variations of the properties of the mid-IR features, by analyzing the spectral maps of a sub-sample of sources: IC 342, M 17, M 51, M 82, M 83, 30 Doradus, and the Orion bar. These objects are those which are spatially resolved, satisfy the two PAH-to-continuum and signal-to-noise ratio thresholds listed in §4.1, and show significant variations of the band ratios. Similar to §4.1, we systematically compare the results of the two methods, but instead of applying them to integrated spectra, we fit the spectrum of each pixel of the spectral maps. We then degrade the images of each spectral component to the spatial resolution of the longest wavelength of the spectrum ($\text{FWHM} \simeq 9''$). We achieve this by convolving the image of a given component (e.g. $I_{6.2}$), with the PSF at the longest wavelength (i.e. $\lambda = 16\ \mu\text{m}$) deconvolved beforehand by the PSF of the component (i.e. $\lambda = 6.2\ \mu\text{m}$). Figs. 7 to 12 (as well as Figs. 22 to 36 in App. A) show the same correlations as in Figs. 3-5, obtained inside resolved sources, instead of integrated spectra. Each data point represents the fit of the spectrum of one pixel. We selected the points, according to the criterion defined in §4.1: the signal-to-noise ratio at $\lambda = 7.7\ \mu\text{m}$ must be larger than 6, and $I_{\text{PAH}}/I_{\text{cont}} \geq 0.5$ with the *Lorentzian method*, and $I_{\text{PAH}}/I_{\text{cont}} \geq 0.3$ with the *Spline method*. The pixels which do not fall into this category have not been considered here. The parameters and statistical quantities relative to these correlations are given in Table 2. Figs. 13 to 14 (as well as Figs. 37 to 41 in App. A) show the spatial distributions of the

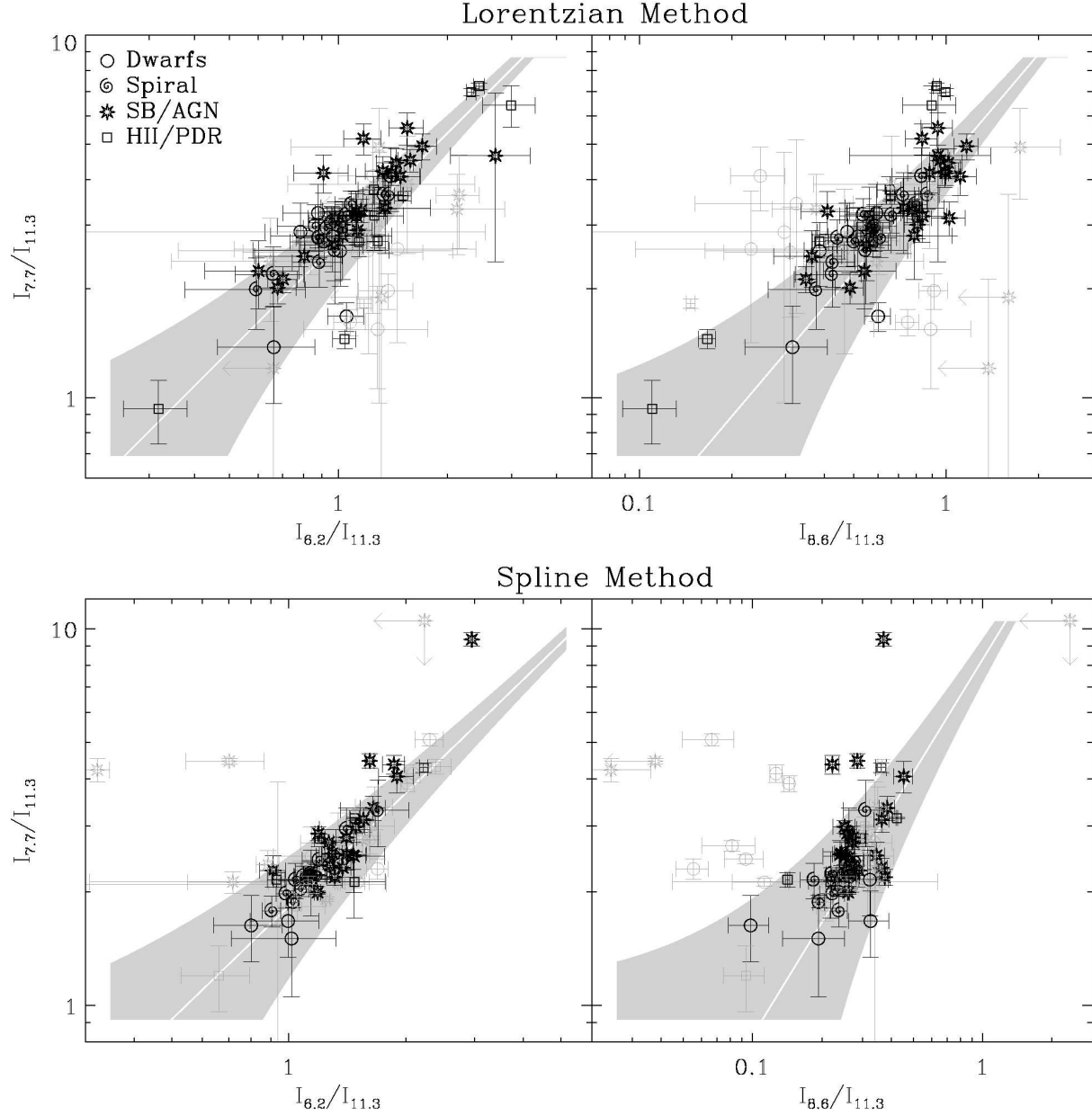


Fig. 3.— PAH properties for integrated spectra. The black error bars are for the measurements that we consider to be reliable, while the grey are more uncertain. In each panel representing a relation Y versus X , the grey filled area is the domain between $Y = a_{Y/X} \times X - 1\sigma_{Y/X}$, and $Y = a_{Y/X} \times X + 1\sigma_{Y/X}$, $Y = a_{Y/X} \times X$ being the linear correlation of the data, and $\sigma_{Y/X}$, the dispersion of the data around this correlation.

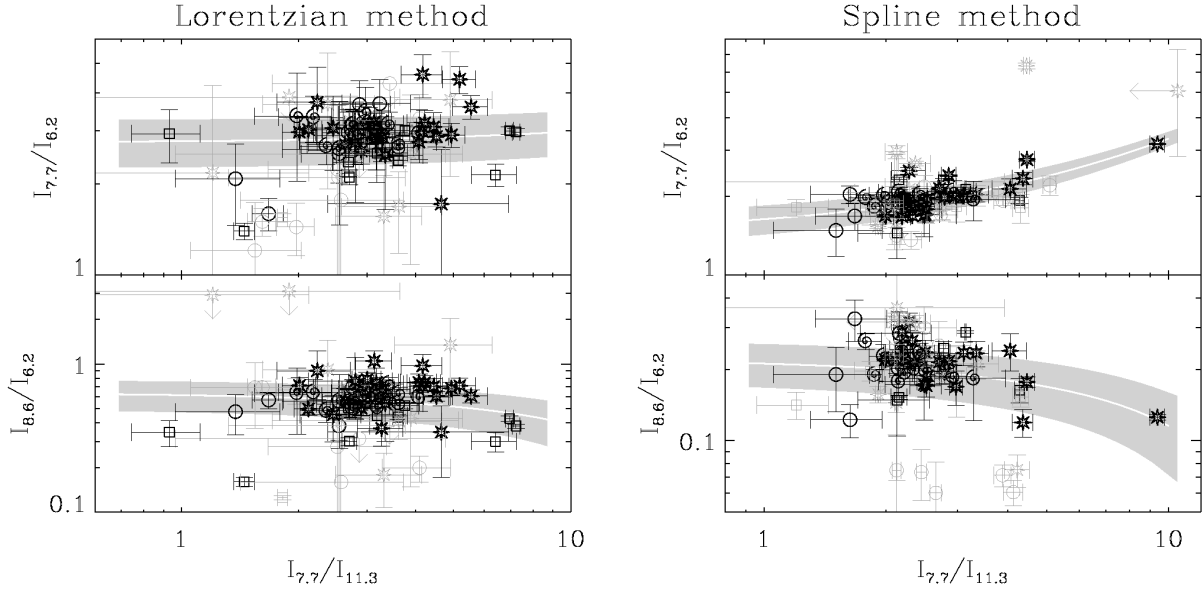


Fig. 4.— PAH properties for integrated spectra (continued). The same symbol conventions are adopted as in Fig. 3.

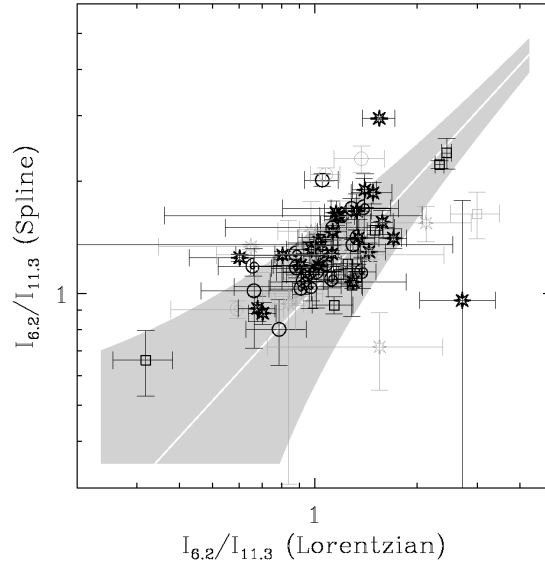


Fig. 5.— Comparison between the two methods. The same symbol conventions are adopted as in Fig. 3.

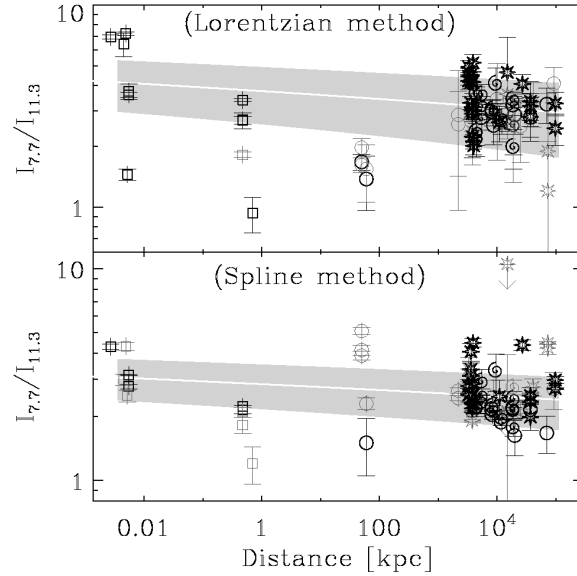


Fig. 6.— Correlation of the band ratio with the distance. The absence of correlation shows the uniformity of the sample. The same symbol conventions are adopted as in Fig. 3.

components.

In general, the correlations presented in Figs. 3-5 still hold inside individual objects as well. Therefore, the variations of the PAH band ratios are independent of the spatial resolution. For example, the pixel size is $\simeq 0.1$ pc in M 17 and the Orion bar, while it is $\simeq 1$ kpc in external galaxies. From the images, we notice that the ratio $I_{6.2}/I_{11.3}$ (as well as the ratios $I_{7.7}/I_{11.3}$ and $I_{8.6}/I_{11.3}$) is roughly correlated with the intensity of the PAH emission, the highest ratios being found in the brightest regions (spiral arms, starburst region, etc.), while the lowest ratios are generally found in the extended, low-luminosity regions. We do not detect any significant variations of the centroid of the $7.7 \mu\text{m}$ feature inside each source. However, the average centroid varies from one source to another.

App. A comments on each individual source. Here we will illustrate the systematic variations within the individual sources by focusing on two extragalactic sources: the edge-on irregular starburst galaxy M 82 and the face-on spiral galaxy M 51. For M 82 (Fig. 13), the maximum values of the $I_{7.7}/I_{11.3}$ ratio are found along the disc, in the star forming region, where the infrared emission is the highest. The value of the band ratio drops by a factor of $\simeq 3$ at $\simeq 200$ pc above and below the disc, in the halo. For M 51 (Fig. 14), the $I_{7.7}/I_{11.3}$ ratio is maximum along the circumnuclear ring. It is somewhat lower in the $10''$ nuclear region. The band ratio is also high along the spiral arms, coinciding with the infrared bright blobs, but can exhibit variations by a factor of $\simeq 2$. Finally, the ratio drops in the interarm region.

The highest values of the $I_{7.7}/I_{11.3} \simeq 7$ ratio (*Lorentzian method*), found in the nuclear star forming regions of M 82 and M 51, are similar to the values found in the compact Galactic H II regions IR 15384 and IR 18317 (Table 4). Intermediate values of $I_{7.7}/I_{11.3} \simeq 3$ (*Lorentzian method*), similar to the Galactic reflection nebula NGC 2023 are found in the halo of M 82 and along spiral arms of M 51. The lowest values of $I_{7.7}/I_{11.3} \lesssim 1$ (*Lorentzian method*), seen in the planetary nebula NGC 7027, correspond to the outermost regions of the two galaxies.

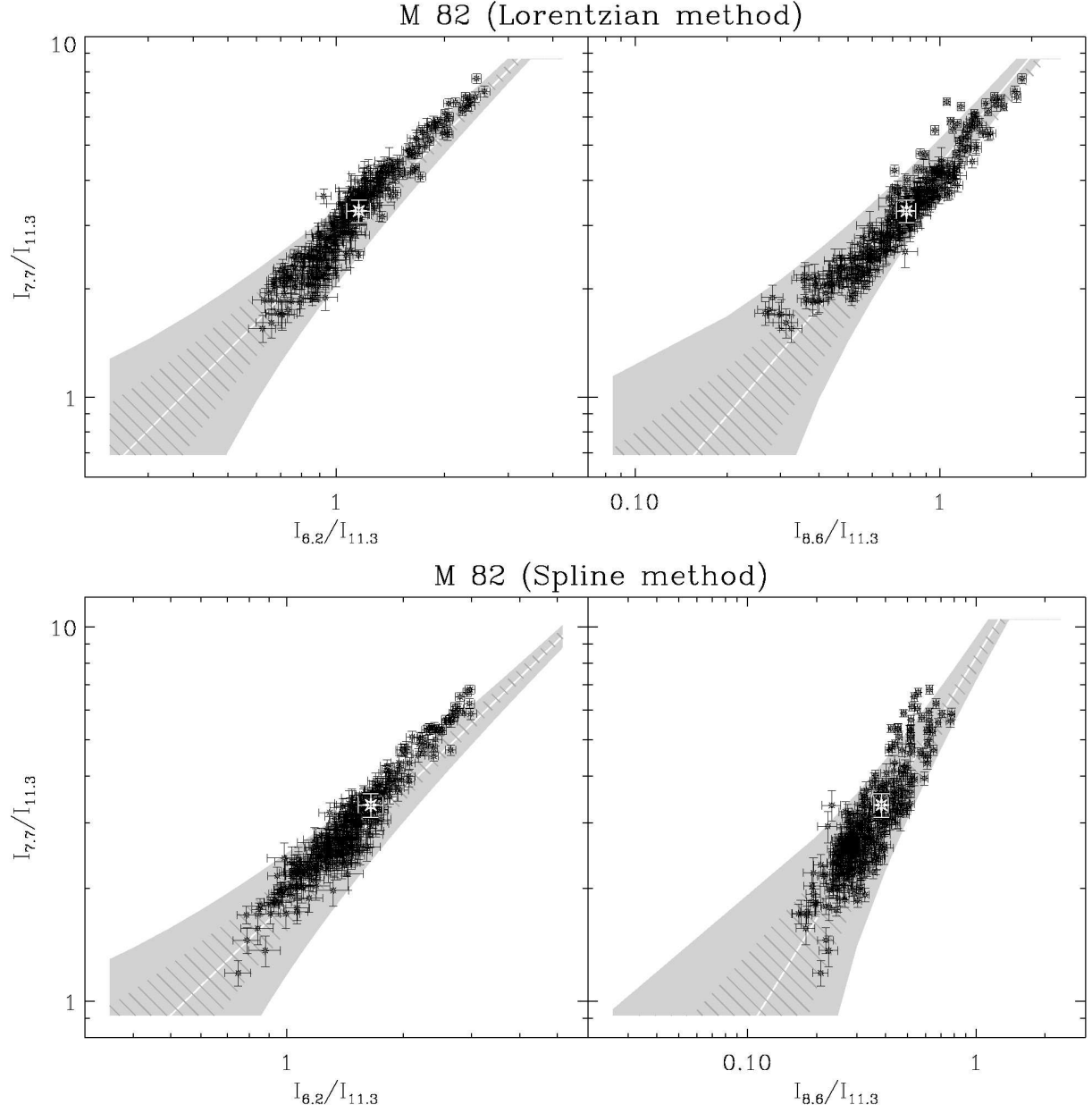


Fig. 7.— PAH band ratios within M 82. The grey filled areas are the correlations obtained for the integrated spectra (Fig. 3). The correlations obtained inside M 82 are represented by the hatched region. The white symbol is the value of the global measurement over the entire galaxy.

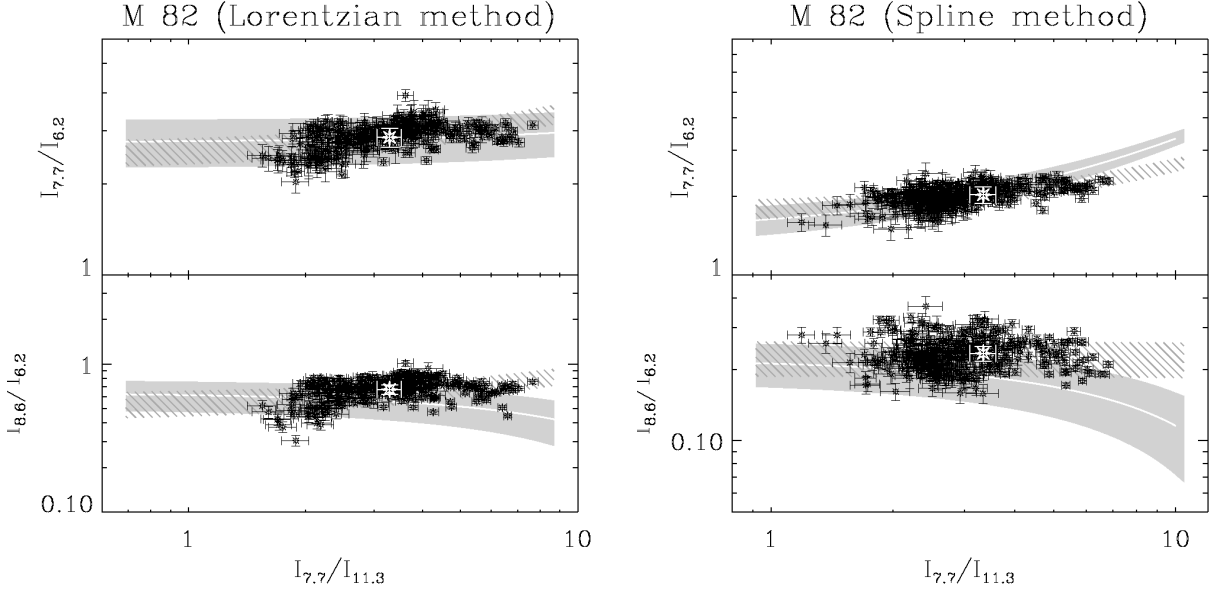


Fig. 8.— PAH band ratios within M 82 (continued).

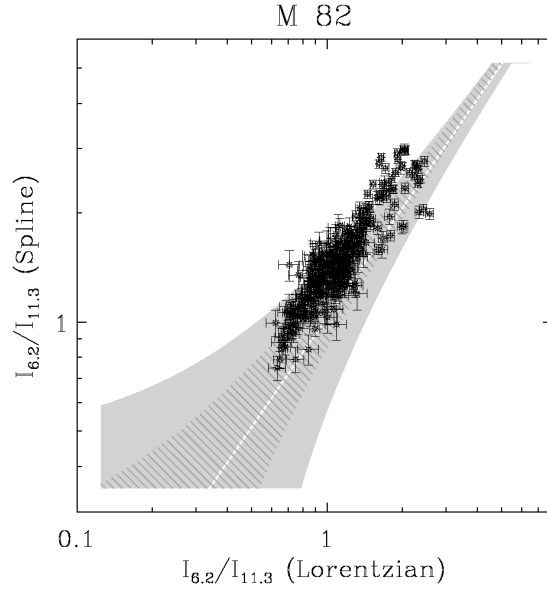


Fig. 9.— Comparison between the two methods in M 82. The same symbol conventions are adopted as in Fig. 7.

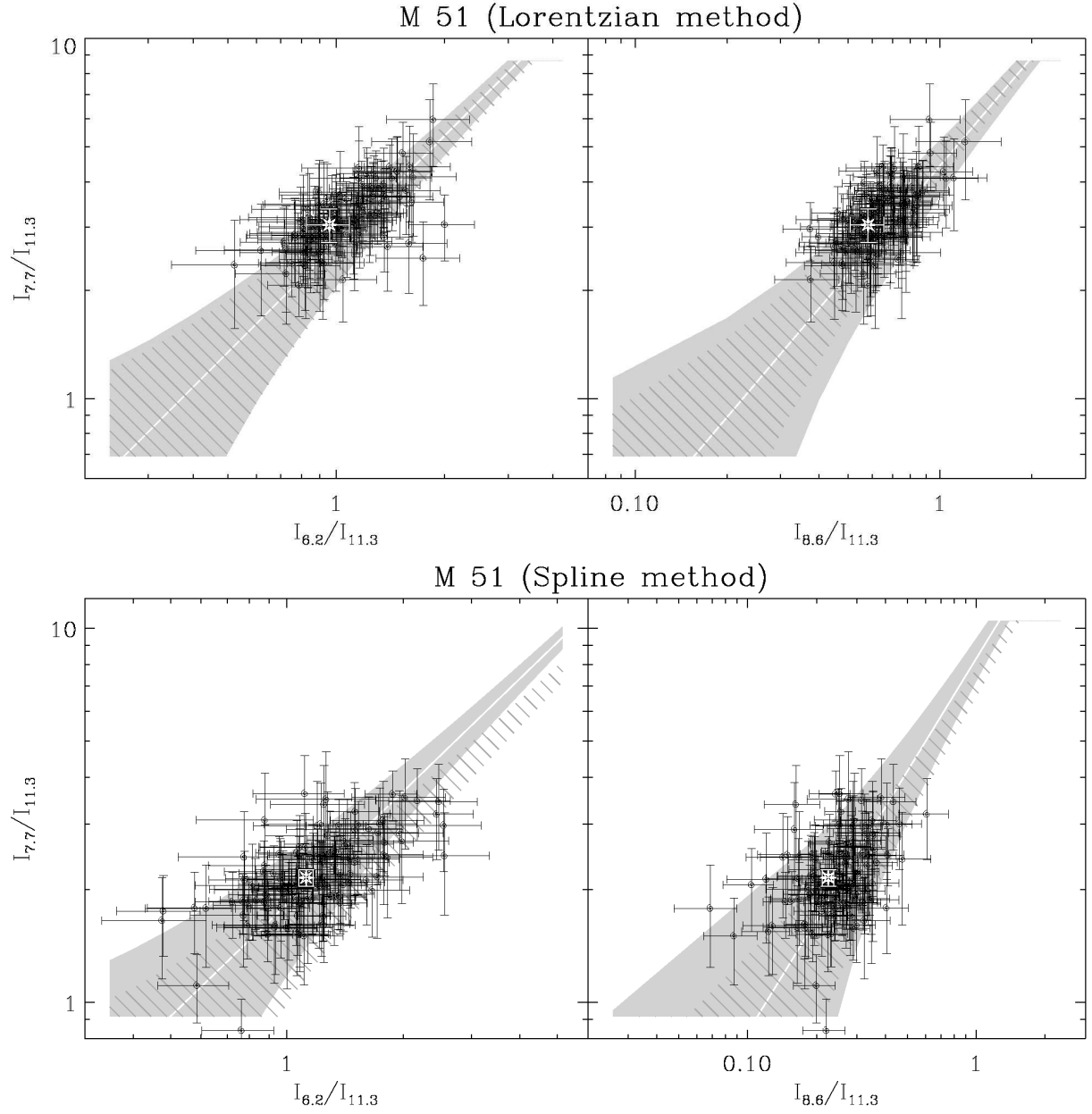


Fig. 10.— PAH band ratios within M 51. The same symbol conventions are adopted as in Fig. 7.

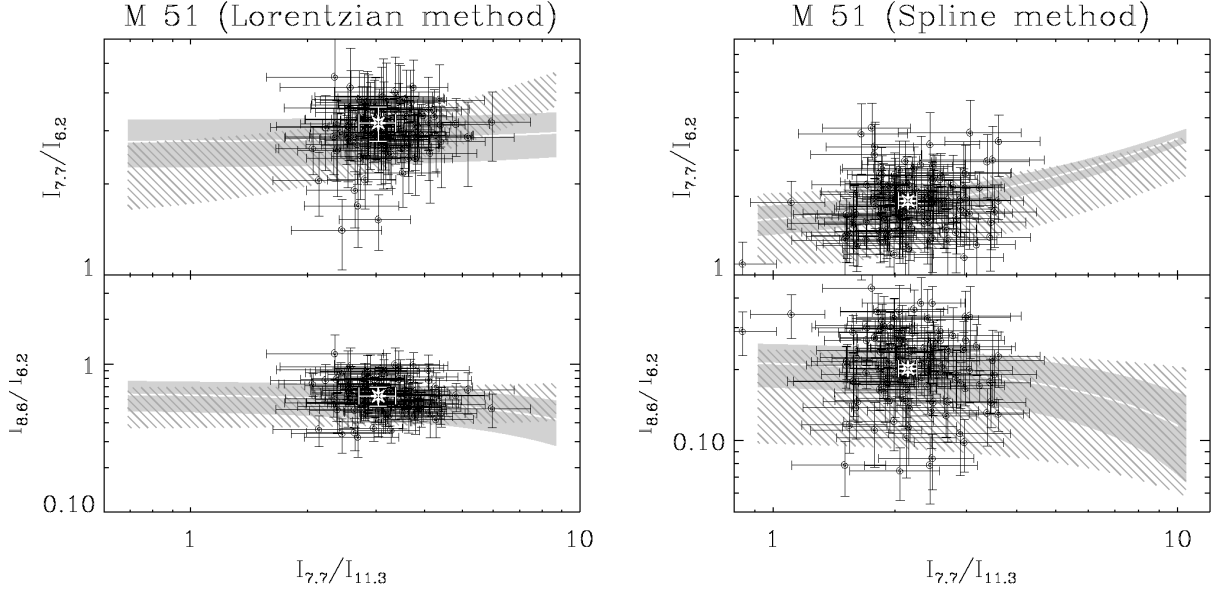


Fig. 11.— PAH band ratios within M 51 (continued).

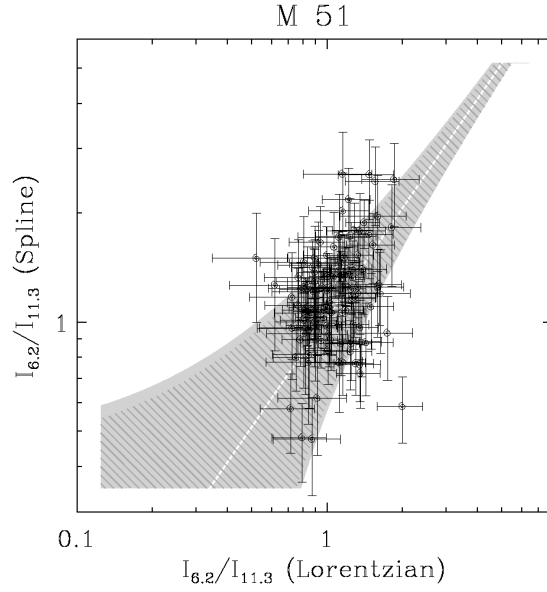


Fig. 12.— Comparison between the two methods in M 51. The same symbol conventions are adopted as in Fig. 7.

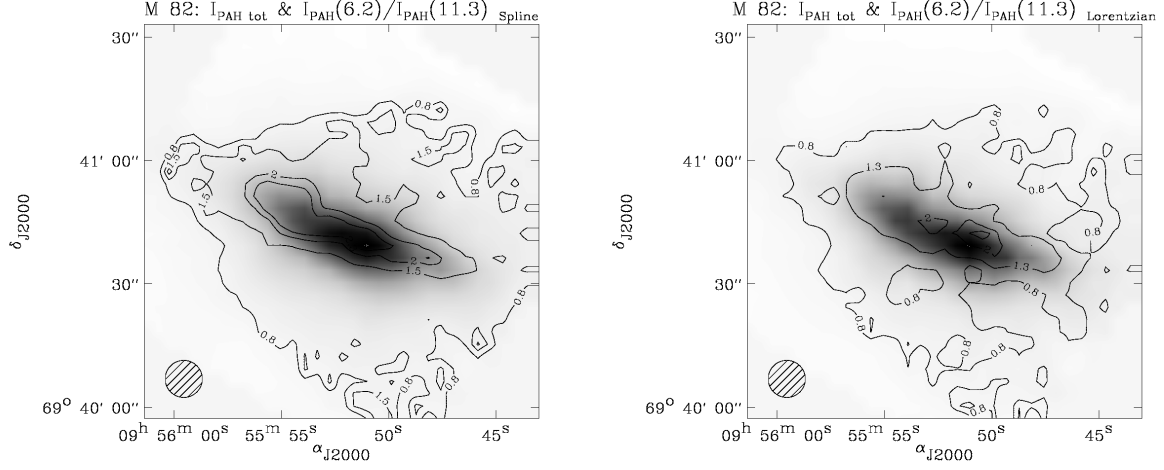


Fig. 13.— Spatial distribution of the PAHs in M 82. For each method, the image is the total PAH intensity, and the contours are the $I_{6.2}/I_{11.3}$ ratio. The shaded circle indicates the beam size.

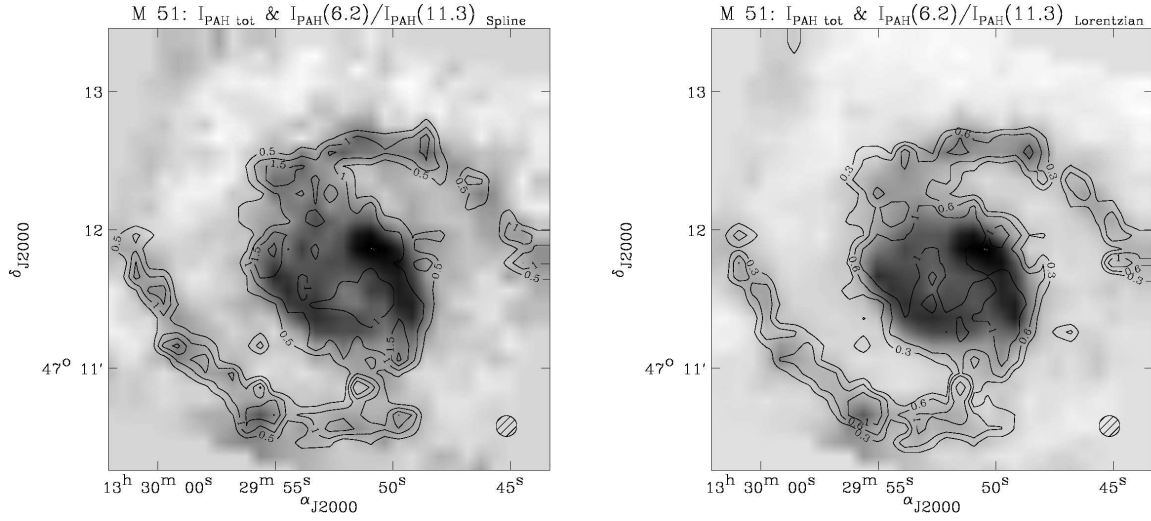


Fig. 14.— Spatial distribution of the PAHs in M 51. For each method, the image is the total PAH intensity, and the contours are the $I_{6.2}/I_{11.3}$ ratio. The shaded circle indicates the beam size.

Table 2. Parameters of the various correlations.

Source	X	Y	Method	$a_{Y/X}$	$b_{Y/X}$	$\sigma_{Y/X}$	$\rho_{Y/X}$
Integrated spectra (Fig. 3)	$I_{6.2}/I_{11.3}$	$I_{7.7}/I_{11.3}$	\mathcal{S}	1.78	0	0.69	0.89
			\mathcal{L}	2.70	0	0.64	0.85
	$I_{8.6}/I_{11.3}$	$I_{7.7}/I_{11.3}$	\mathcal{S}	8.21	0	1.09	0.44
			\mathcal{L}	4.43	0	0.79	0.78
	$I_{6.2}/I_{11.3}$	$I_{6.2}/I_{11.3}$	\mathcal{S}/\mathcal{L}	1.03	0	0.46	0.45
M 82 (Fig. 7)	$I_{6.2}/I_{11.3}$	$I_{7.7}/I_{11.3}$	\mathcal{S}	1.86	0	0.32	0.97
			\mathcal{L}	2.70	0	0.32	0.97
	$I_{8.6}/I_{11.3}$	$I_{7.7}/I_{11.3}$	\mathcal{S}	8.06	0	0.53	0.87
			\mathcal{L}	4.04	0	0.39	0.95
	$I_{6.2}/I_{11.3}$	$I_{6.2}/I_{11.3}$	\mathcal{S}/\mathcal{L}	1.07	0	0.23	0.88
	$I_{7.7}/I_{11.3}$	$\lambda_{7.7} [\mu m]$	\mathcal{L}	0	7.68	0.012	...
IC 342 (Fig. 22)	$I_{6.2}/I_{11.3}$	$I_{7.7}/I_{11.3}$	\mathcal{S}	1.50	0	0.63	0.82
			\mathcal{L}	2.33	0	1.35	0.79
	$I_{8.6}/I_{11.3}$	$I_{7.7}/I_{11.3}$	\mathcal{S}	5.71	0	0.69	0.81
			\mathcal{L}	1.89	0	1.41	0.66
	$I_{6.2}/I_{11.3}$	$I_{6.2}/I_{11.3}$	\mathcal{S}/\mathcal{L}	1.12	0	0.40	0.74
	$I_{7.7}/I_{11.3}$	$\lambda_{7.7} [\mu m]$	\mathcal{L}	0	7.68	0.012	...
M 51 (Fig. 10)	$I_{6.2}/I_{11.3}$	$I_{7.7}/I_{11.3}$	\mathcal{S}	1.49	0	0.50	0.62
			\mathcal{L}	2.59	0	0.58	0.65
	$I_{8.6}/I_{11.3}$	$I_{7.7}/I_{11.3}$	\mathcal{S}	7.19	0	0.62	0.41
			\mathcal{L}	4.55	0	0.56	0.65
	$I_{6.2}/I_{11.3}$	$I_{6.2}/I_{11.3}$	\mathcal{S}/\mathcal{L}	1.01	0	0.42	0.33
	$I_{7.7}/I_{11.3}$	$\lambda_{7.7} [\mu m]$	\mathcal{L}	0	7.72	0.012	...
M 83 (Fig. 25)	$I_{6.2}/I_{11.3}$	$I_{7.7}/I_{11.3}$	\mathcal{S}	1.30	0	0.52	0.62
			\mathcal{L}	2.19	0	0.54	0.67
	$I_{8.6}/I_{11.3}$	$I_{7.7}/I_{11.3}$	\mathcal{S}	7.18	0	0.69	0.43
			\mathcal{L}	3.52	0	0.70	0.66
	$I_{6.2}/I_{11.3}$	$I_{6.2}/I_{11.3}$	\mathcal{S}/\mathcal{L}	1.07	0	0.41	0.39

Table 2—Continued

Source	X	Y	Method	$a_{Y/X}$	$b_{Y/X}$	$\sigma_{Y/X}$	$\rho_{Y/X}$
30 Doradus (Fig. 28)	$I_{7.7}/I_{11.3}$	$\lambda_{7.7} [\mu m]$	\mathcal{L}	0	7.71	0.016	\dots
	$I_{6.2}/I_{11.3}$	$I_{7.7}/I_{11.3}$	\mathcal{S}	1.43	0	0.79	0.78
			\mathcal{L}	2.31	0	0.67	0.68
	$I_{8.6}/I_{11.3}$	$I_{7.7}/I_{11.3}$	\mathcal{S}	11.48	0	1.61	0.35
			\mathcal{L}	2.10	0	0.62	0.49
	$I_{6.2}/I_{11.3}$	$I_{6.2}/I_{11.3}$	\mathcal{S}/\mathcal{L}	2.01	0	0.86	0.44
M 17 (Fig. 34)	$I_{7.7}/I_{11.3}$	$\lambda_{7.7} [\mu m]$	\mathcal{L}	0	7.66	0.016	\dots
	$I_{6.2}/I_{11.3}$	$I_{7.7}/I_{11.3}$	\mathcal{S}	1.96	0	0.33	0.81
			\mathcal{L}	2.41	0	0.45	0.93
	$I_{8.6}/I_{11.3}$	$I_{7.7}/I_{11.3}$	\mathcal{S}	11.91	0	0.81	0.33
			\mathcal{L}	4.04	0	0.84	0.80
	$I_{6.2}/I_{11.3}$	$I_{6.2}/I_{11.3}$	\mathcal{S}/\mathcal{L}	1.01	0	0.25	0.61
Orion bar (Fig. 31)	$I_{7.7}/I_{11.3}$	$\lambda_{7.7} [\mu m]$	\mathcal{L}	0	7.69	0.012	\dots
	$I_{6.2}/I_{11.3}$	$I_{7.7}/I_{11.3}$	\mathcal{S}	1.77	0	0.32	0.83
			\mathcal{L}	2.32	0	0.21	0.95
	$I_{8.6}/I_{11.3}$	$I_{7.7}/I_{11.3}$	\mathcal{S}	8.38	0	0.38	0.91
			\mathcal{L}	3.72	0	0.52	0.86
	$I_{6.2}/I_{11.3}$	$I_{6.2}/I_{11.3}$	\mathcal{S}/\mathcal{L}	1.01	0	0.29	0.40
	$I_{7.7}/I_{11.3}$	$\lambda_{7.7} [\mu m]$	\mathcal{L}	0	7.68	0.011	\dots

Note. — This table gives, for two given measured quantities X and Y , the parameters corresponding to the fit of Y by $a_{Y/X} \times X + b_{Y/X}$. The dispersion of the measures around this correlation is $\sigma_{Y/X} = \sqrt{\langle (Y - a_{Y/X} \times X + b_{Y/X})^2 \rangle}$. In the case where $b_{Y/X} = 0$, $\rho_{Y/X}$ is the linear correlation coefficient.

5. INTERPRETATION OF THE AROMATIC FEATURE VARIATIONS

5.1. Origin of the Band Ratio Variations

The main conclusions of §4 are that *(i)* the ratios $I_{6.2}/I_{11.3}$, $I_{7.7}/I_{11.3}$ and $I_{8.6}/I_{11.3}$ are correlated and span one order of magnitude throughout our sample, and *(ii)* the ratios $I_{7.7}/I_{6.2}$ and $I_{8.6}/I_{6.2}$ are not significantly anticorrelated with the $I_{7.7}/I_{11.3}$ ratio, and do not show significant variations within the sources which have the best signal-to-noise ratios (especially M 82). As explained in §1 and demonstrated in Fig. 1, the intensity of the features between 6 and 9 μm relative to the 11.3 μm band are one order of magnitude higher for PAH^+ than for PAH^0 . Therefore, the universal correlations displayed from Fig. 3 to Fig. 33 can be attributed to variations of the charge of the carriers of the aromatic features. However, before concluding, we first need to explore the ability of other physical processes to reproduce these trends.

First, dehydrogenation of the PAHs have an effect similar to ionization, on the mid-IR spectrum, as shown by several laboratory studies (Allamandola et al. 1989; Allain et al. 1996; Jochims et al. 1999). However, as reported by Allain et al. (1996), only PAHs containing less than $N_C \simeq 50$ carbon atoms can be considerably dehydrogenated. At the same time, this threshold corresponds to the minimum size of PAHs that can survive in most PDRs (Allain et al. 1996). For comparison, the PAH size distribution derived by Zubko et al. (2004), for the diffuse Galactic ISM, has a lower cut-off of $N_C^{\text{min}} = 20$. Their emission is dominated by PAHs of $N_C \simeq 50 - 500$, depending on their excitation rate. This conclusion is supported by the observed linear correlation of the 3.3 μm band with the 11.3 μm band in Galactic sources (Hony et al. 2001). If dehydrogenation were important then a non-linear relation would be expected as duo and trio groups (with bands longwards of 11.3 μm) were converted into solo groups (with a 11.3 μm band; Schutte et al. 1993; Hony et al. 2001). Likewise, if dehydrogenation were important, then the decrease in the $I_{11.3}/I_{6.2}$ ratio (decreasing H coverage) would be expected to be accompanied by a decreasing $I_{12.7}/I_{11.3}$ ratio (conversion of duo/trio's into solo's) in contrast to the observations (Hony et al. 2001). Therefore, we can neglect the effect of dehydrogenation on our mid-IR spectra.

Second, deep extinction by the silicate feature at 9.7 μm can cause variations of the band ratios, as proposed by Peeters et al. (2002b), Spoon et al. (2002) or Brandl et al. (2006). Indeed, the 11.3 μm feature is more absorbed than the 7.7 μm band. This effect would also cause the 8.6 μm feature to suffer from the same amount of extinction as the 11.3 μm band, and these two bands should be correlated. However, this is not what Figs. 3 to Fig. 35 show. Moreover, the *Lorentzian method* corrects the bands for extinction (§3). The good agreement between the *Lorentzian method* and the *Spline method* tells us that extinction can

not explain the majority of the observed band ratio variations. Finally, there is no evidence for silicate absorption in the spectra of the Orion bar. Indeed, the total gas and dust column along the line of sight for this source is insufficient to produce noticeable $10\ \mu\text{m}$ absorption.

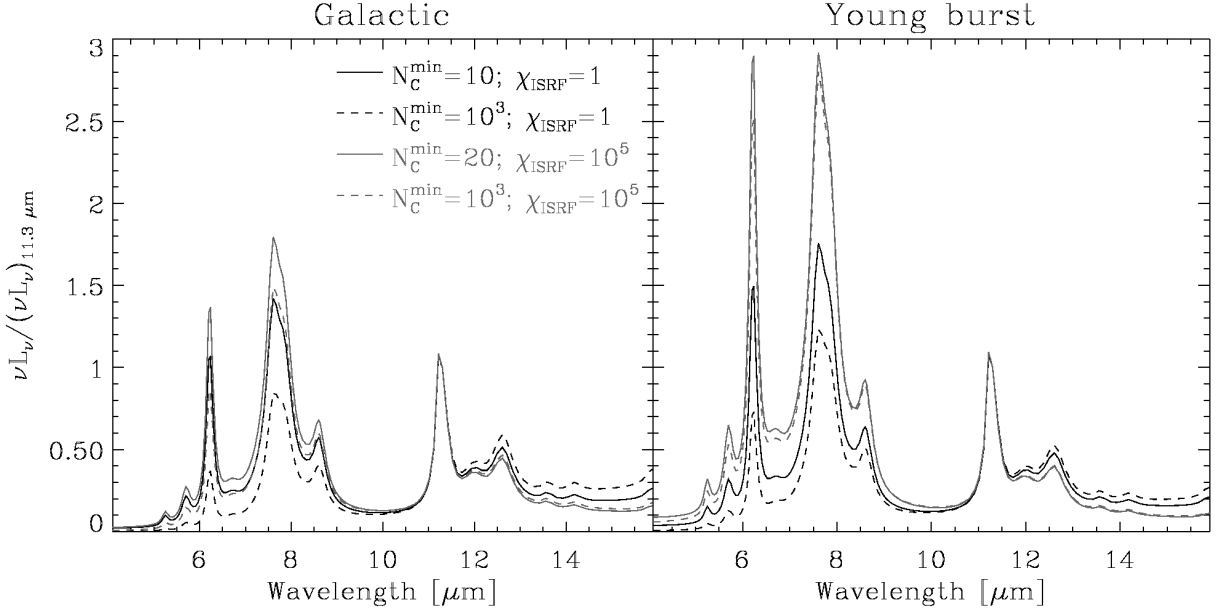


Fig. 15.— Effects of the temperature distribution on the PAH spectra. The various curves are the theoretical emission spectra, varying the shape (Galactic or young starburst) and the intensity of the ISRF (χ_{ISRF}), as well as the lower cut-off of the size distribution (N_C^{min}). The size distribution is the BARE-GR-S of Zubko et al. (2004). The absorption efficiencies are taken from Draine & Li (2007).

Third, a modification of the temperature distribution of the PAHs can affect the relative weight of the aromatic features. For example, truncating the highest temperatures would have the effect of decreasing the intensity of the short wavelength bands relative to the long wavelength ones. There are essentially two ways of modifying the temperature distribution of the molecules: (i) by varying the interstellar radiation field (ISRF) intensity or shape, and (ii) by changing their size distribution. The latter effect could happen in the vicinity of a very hard radiation source, like an AGN, where the smallest PAHs could undergo photosublimation, as proposed by Smith et al. (2007).

We performed theoretical modeling of the PAH emission spectra, in order to study the latter effects. These spectra, which take into account the stochastic heating of the particles, are shown in Fig. 15. We adopted the PAH size distribution by Zubko et al. (2004, bare grains, solar abundance constraints; BARE-GR-S), and the absorption efficiencies by Draine & Li (2007), with an ionization fraction of 50%. We consider successively two classes

of ISRF, in order to explore the effect of the hardness of the radiation on the PAH emission: (i) the Galactic ISRF of Mathis et al. (1983) and (ii) a very hard ISRF, corresponding to an instantaneous burst of star formation with a Salpeter IMF, synthesized with the stellar evolutionary model PÉGASE (Fioc & Rocca-Volmerange 1997). The latter is normalised to the intensity of the Mathis et al. (1983) ISRF. We also vary the intensity of each ISRF, by multiplying them by a factor $\chi_{\text{ISRF}} = 1 - 10^5$. In addition, we explore the effect of a possible small PAH segregation, by varying the value of the lower cut-off of the PAH size distribution. This lower cut-off is $N_{\text{C}}^{\text{min}} = 20$ carbon atoms, for the Zubko et al. (2004) model. We vary it up to $N_{\text{C}}^{\text{min}} = 10^3$. Finally, we apply a screen extinction to the modeled spectra by multiplying them by a factor $\exp[-\tau(\lambda, A_V)]$. We adopt the Zubko et al. (2004) optical depth, $\tau(\lambda, A_V)$, and plot the results using two values of the V band attenuation: $A_V = 0$ (no extinction) and $A_V = 10$.

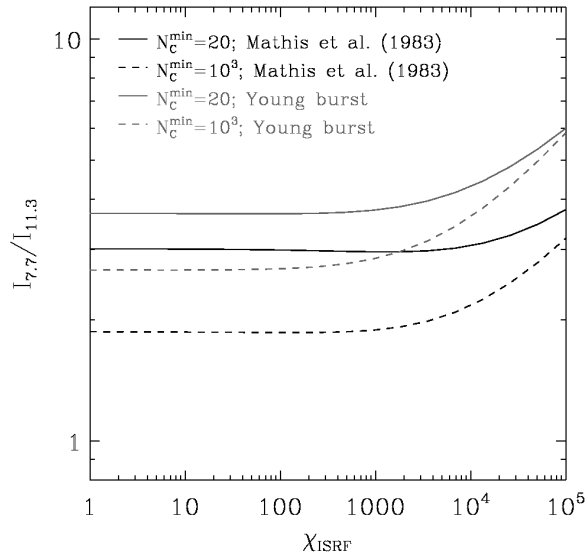


Fig. 16.— Theoretical modeling of the effect of the PAH temperature distribution on their band ratios, with a fixed ionization fraction (50%). No extinction is applied.

Figs. 16-17 synthesize the results of this modeling. Fig. 16 demonstrates that effect of the radiation field intensity on the $I_{7.7}/I_{11.3}$ band ratio, for the two types of radiation fields and the two extreme PAH size cut-offs. This figure shows that, for a given size distribution and ISRF type, the $I_{7.7}/I_{11.3}$ ratio is independent of the intensity of the ISRF, up to $\chi_{\text{ISRF}} \simeq 10^4$. Indeed, the PAHs are stochastically heated below $\chi_{\text{ISRF}} \simeq 10^4$, therefore the shape of their emission spectrum is independent of the ISRF. However, when $\chi_{\text{ISRF}} \gtrsim 10^4$, the largest PAHs reach thermal equilibrium, and the temperature fluctuation range shrinks significantly enough to affect the ratio between the bands. Fig. 17 shows how every effect considered here

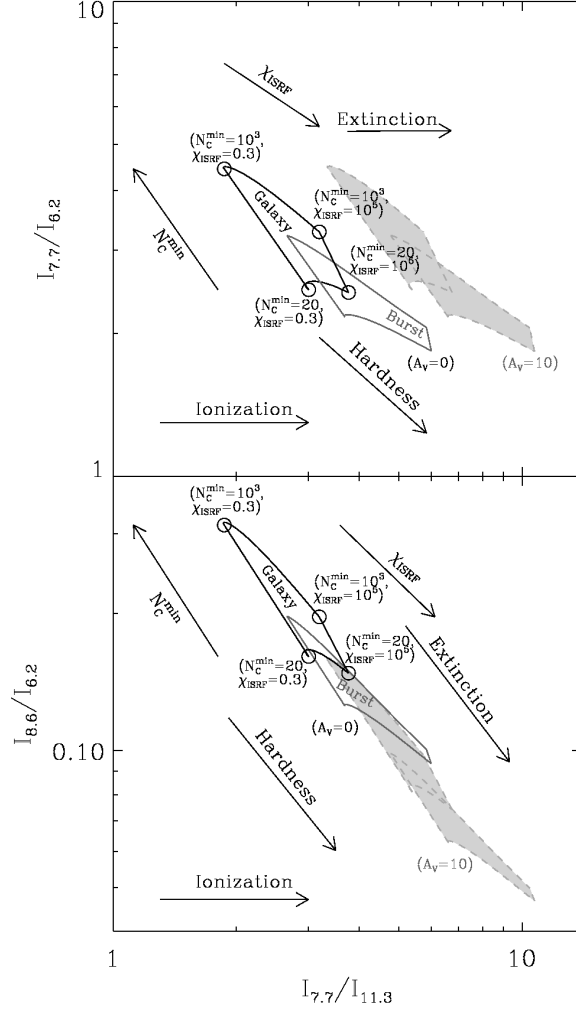


Fig. 17.— The two panels present the results of the same modeling as in Fig. 16, the only difference being that the top panel shows the resulting $I_{7.7}/I_{6.2}$, while the bottom panel shows the $I_{8.6}/I_{6.2}$. To read this figure, first look at the black empty polygon with the circled corners. This polygon shows the effect of varying both the minimum cut-off PAH size, N_C^{\min} , and the ISRF intensity, χ_{ISRF} , with the Galactic ISRF (labeled *Galaxy*) and with no extinction. The values between parenthesis, close to each corners are the values of these two parameters at the corner. Second, the grey empty polygon is the analog of the previous one, except that the ISRF is now the Starburst one (labeled *Burst*). Finally, the two grey filled polygons are the analog of the two previous ones, except that we applied a screen extinction with $A_V = 10$. As a summary, the various arrows show the sense of variation of the band ratios with each parameter, including the ionization degree of the PAHs.

affects the relation between $I_{7.7}/I_{11.3}$ and $I_{7.7}/I_{6.2}$ and $I_{8.6}/I_{6.2}$. The arrows indicate the direction toward which these parameters affect the relation. This figure shows that the combination of all the effects affecting the PAH temperature distribution (ISRF intensity, ISRF hardness and size distribution) can not explain a variation of the $I_{7.7}/I_{11.3}$ ratio by more than a factor $\simeq 3$. Moreover, it shows that if these effects were responsible for the variation of the $I_{7.7}/I_{11.3}$ ratio, then the $I_{7.7}/I_{6.2}$ ratio would also be anticorrelated with it. The ratio $I_{7.7}/I_{6.2}$ is particularly very sensitive to N_C^{\min} . According to Fig. 17, an increase of the $I_{7.7}/I_{11.3}$ ratio by a factor $\simeq 3$ would imply a decrease of the $I_{7.7}/I_{6.2}$ ratio by a factor of $\simeq 2$.

One of the strong results of §4.1 and §4.2 is that the ratios $I_{7.7}/I_{6.2}$ do not show any trend with $I_{7.7}/I_{11.3}$. Therefore, the correlations discussed in §4 can not be attributed to a modification of the temperature distribution. In particular, we can rule out an interpretation of the variation of the $I_{7.7}/I_{11.3}$ in terms of destruction of the smallest PAHs. These results are in good agreement with those by Hony et al. (2001), who studied a wide sample of Galactic sources and showed that the $I_{3.3}/I_{11.3}$ ratio was not varying significantly, while the $I_{6.2}/I_{11.3}$ ratio was varying by a factor of 5. In addition, Fig. 17 shows that the effect of extinction do not account for our observed trends. Indeed, the bottom panel of Fig. 17 shows that the 8.6 μm and 11.3 μm bands would be correlated if extinction was the main cause of variation of the aromatic bands. Consequently, our work shows that the variation of the PAH band ratios, throughout different environments, and at different spatial scales, is primarily controlled by the ionization fraction of the molecules. In addition, it appears that the mixture of PAH molecules, in all these environments, is remarkably universal.

We emphasize that our sample contains only a few AGNs. Therefore, our results reflect primarily the properties of star forming regions. Observations of AGN environments by Smith et al. (2007) and Kaneda et al. (2007) show PAH properties that differ from our trends, suggesting that the AGN could alter the PAH composition.

5.2. Relating the Band Ratios to the Physical Conditions

In §5.1, we showed that the band ratio variations were essentially due to a variation of the fraction of ionized PAHs in the beam. The mid-IR feature ratios are therefore related to the physical conditions where the emission is originating. Indeed, the fraction of ionized PAHs, in a given region, depends on the quantity $G_0/n_e \times \sqrt{T_{\text{gas}}}$ (Tielens 2005, for a review), where G_0 , is the UV radiation field density, n_e , the electron density, and T_{gas} , the gas temperature. The UV field density is the integration between $\lambda = 0.09 \mu\text{m}$ and $\lambda = 0.2 \mu\text{m}$ of the

monochromatic mean intensity, J_λ , and is normalised to the solar neighborhood value:

$$G_0 = \frac{\int_{0.09 \mu\text{m}}^{0.2 \mu\text{m}} 4\pi J_\lambda d\lambda}{1.6 \times 10^{-6} \text{ W m}^{-2}}. \quad (3)$$

We emphasize that, although §5.1 showed that the intensity of the ISRF was not responsible for the observed variations of the aromatic band ratios, the intensity of the ISRF is likely to vary significantly within and among our sources. In this section, we use the most well-studied Galactic regions of our sample, in order to derive an empirical relation between the $I_{6.2}/I_{11.3}$ band ratio and the quantity $G_0/n_e \times \sqrt{T_{\text{gas}}}$.

Region	G_0	T_{gas} [K]	n_{H} [cm ⁻³]	Reference
NGC 2023	1.5×10^4	750	10^5	Steiman-Cameron et al. (1997)
NGC 7027	6×10^5	2000	10^7	Justtanont et al. (1997)
Orion bar (position 4)	4×10^4	500	5×10^4	Tauber et al. (1994)

Table 3: Physical conditions in select regions. The last columns refers to the study where these quantities have been derived.

Bregman & Temi (2005) gave such a calibration, from the spectro-images of three reflection nebulae. In order to derive the physical conditions in their nebulae, they made several hypotheses. They *(i)* assumed a constant electronic density throughout their regions, *(ii)* they neglected dust extinction, and *(iii)* they derived the relative geometry of the star and nebula from the profile of the scattered light. In our analysis, we have adopted a slightly different strategy. We have made the conscious decision to include only the sources for which the physical conditions have been reliably determined, using PDR models, constrained by several gas lines. The sources of our sample which have been modeled in detail are NGC 2023, NGC 7027 and position 4 of the Orion bar (Roche et al. 1989). Their properties are summarized in Table 3.

We adopt the values given in Table 3 and assume that the electrons result from photo-ionization of carbon and that all the gas phase carbon is ionized in PDRs, so that:

$$n_e \simeq \left(\frac{\text{C}}{\text{H}}\right) \times n_{\text{H}} \simeq 1.6 \times 10^{-4} n_{\text{H}}, \quad (4)$$

where we have adopted the carbon abundance by Sofia et al. (2004). For NGC 2023 and NGC 7027, we do not have reliable spatial information, hence we will only use the global values of the ratios. In the Orion bar, we study the spatial variations by proceeding as follows.

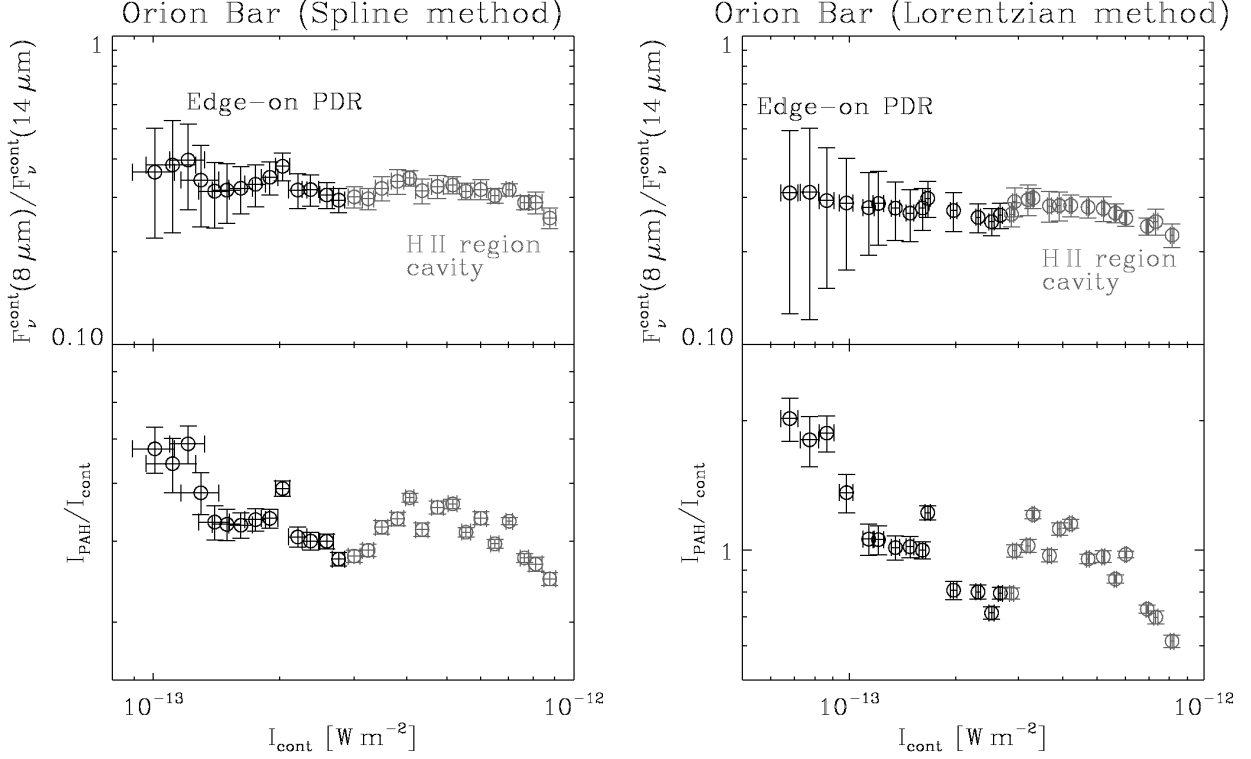


Fig. 18.— **Top panels:** variation of the color of the VSG continuum (ratio of the flux at 8 and $14 \mu\text{m}$) as a function of the intensity of the VSG continuum, inside the Orion bar. These figures show that the color of the VSG continuum is virtually independent of its intensity, since these grains are stochastically heated. **Bottom panels:** variation of the PAH-to-VSG ratio as a function of the intensity. These figures show that the relative strength of the PAHs in the PDR decreases slightly toward the H II region (when I_{cont} increases), as an effect of their photo-depletion.

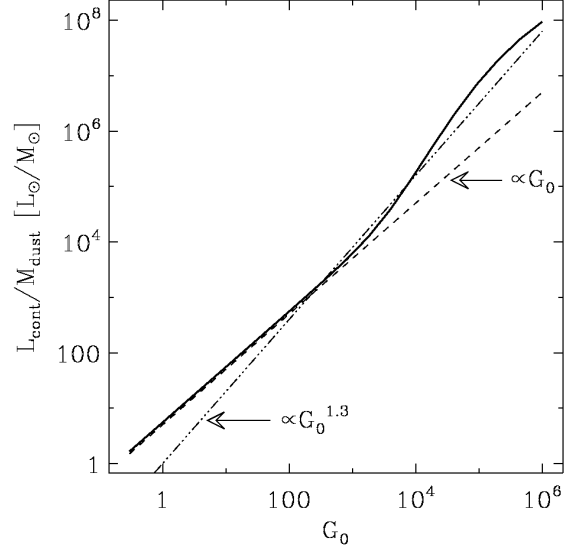


Fig. 19.— Theoretical modeling of the continuum intensity as a function of the UV radiation field, G_0 , in black. $L_{\text{cont}}/M_{\text{dust}}$ is the luminosity of the graphite component of Zubko et al. (2004), integrated between 10 and 16 μm , and normalized to the dust mass. The dotted line varies as G_0 . The dashed-dotted line is a power-law fit to the black line, in the range $10^2 < G_0 < 10^4$.

1. We exclude the region north of the bar (see Fig. 40), which is the location of the H II region cavity. Indeed, the PAH-to-continuum ratio is very low there, thus the fits are uncertain. Moreover, the spherical geometry of the region causes confusion along the lines of sight. To the contrary, the region south of the bar, is an edge-on PDR, where the conditions are believed to be roughly homogeneous along each line of sight. Indeed, it is observed to be well stratified in the main PDR tracers (CO data as well as H₂, C I, C II and PAH data; Tielens et al. 1993; Tauber et al. 1994; Wyrowski et al. 1997; and HCN data by Fuente et al. 1996).
2. We assume that the column density is homogeneous in the edge-on PDR, so that we can use the intensity of the VSG continuum, in order to scale the intensity of the UV radiation field, G_0 . Indeed, the top panels of Fig. 18 show that the VSGs are stochastically heated. Therefore, their intensity scales with the radiation field density. Moreover, the intensity of the VSG continuum is probably a better tracer of the radiation density than the PAHs, since the latter are gradually depleted in direction of the H II region (bottom panels of Fig. 18). Fig. 19 illustrates this fact by showing the theoretical variation of the integrated intensity of the VSG continuum between 10 and 16 μm , as a function of G_0 . To perform this simulation, we used the radiation field defined in Eq. (3), and the Galactic graphite size distribution of Zubko et al. (2004, with solar abundance constraints). For $G_0 \lesssim 10^3$, the mid-IR continuum intensity scales perfectly with G_0 , since the grains are out of thermal equilibrium. At higher G_0 , the relation between G_0 and I_{cont} becomes non-linear due to temperature effects. In the range $10^2 \lesssim G_0 \lesssim 10^4$, which are the conditions in the Orion bar, the UV radiation field is very well approximated by $G_0 \propto I_{\text{cont}}^{1/1.3}$. This method has the advantage of taking into account the actual variations of G_0 , with both the distance from the star cluster, and the dust extinction.
3. In order to improve the signal-to-noise ratio of our spectra, we average the pixels into 30 bins of energy (I_{cont}). The two top panels of Fig. 20 show the variation of the $I_{6.2}/I_{11.3}$ ratio, as a function of the continuum intensity, with the two methods.
4. Finally, we assume a constant electron density and temperature throughout the PDR.

The two bottom panels of Fig. 20 shows the final calibration of the band ratio, with the two methods. As found by Bregman & Temi (2005), the ratio $I_{6.2}/I_{11.3}$ (or $I_{7.7}/I_{11.3}$) increases in

the range $10^2 \lesssim G_0/n_e \lesssim 10^3$. The grey stripes are the following linear fits:

$$\begin{cases} \frac{I_{6.2}}{I_{11.3}} \simeq \left(\frac{G_0}{n_e [\text{cm}^{-3}]} \sqrt{\frac{T_{\text{gas}}}{10^3 \text{ K}}} \right) / 3040 + 0.53 \pm 0.10 & (\text{Spline method}), \\ \frac{I_{6.2}}{I_{11.3}} \simeq \left(\frac{G_0}{n_e [\text{cm}^{-3}]} \sqrt{\frac{T_{\text{gas}}}{10^3 \text{ K}}} \right) / 1990 + 0.26 \pm 0.16 & (\text{Lorentzian method}), \end{cases} \quad (5)$$

valid in the range $400 \lesssim \frac{G_0}{n_e [\text{cm}^{-3}]} \sqrt{\frac{T_{\text{gas}}}{10^3 \text{ K}}} \lesssim 4000$.

5.3. Diagnosing Galaxies Using PAH Band Ratios

In principle, Eq. (5) can be used to derive the ratio $G_0/n_e \times \sqrt{T_{\text{gas}}}$ from any mid-IR spectrum. However, if several regions with different physical conditions are encompassed within the spectrograph’s beam, the situation is more complex. The band ratio is then averaged over these various environments and its global value does not reflect a single $G_0/n_e \times \sqrt{T_{\text{gas}}}$.

In the case of the global spectrum of a star forming region, we can expect the $I_{7.7}/I_{11.3}$ ratio to depend on the age and initial mass function of the stellar cluster, that will determine the G_0 at the edge of the PDR, as well as on the geometry of the ISM (clumpiness, densities), that will determine the transfer of the UV light into the PDR, and the electron density. If this hypothesis is correct, the value of $I_{7.7}/I_{11.3}$ can potentially be used in combination with other PDR tracers, like the $[\text{C II}]_{158\mu\text{m}}$, $[\text{O I}]_{63\mu\text{m}}$, $[\text{Si II}]_{34.82\mu\text{m}}$ and H_2 mid-IR rotational lines, to determine the geometry and physical conditions of an unresolved star forming region. Fig. 21 demonstrates the relation between the observed band ratios and the averaged $G_0/n_e \times \sqrt{T_{\text{gas}}}$ quantity.

It has long been surmised that the IR emission features provide a clear mid-IR signature of the interaction of FUV photons with cloud surfaces and hence a probe of the importance of (massive) star formation in a region (Genzel et al. 1998; Peeters et al. 2004b). The present study has extended this by developing the observed 6.2 to 11.3 μm band ratio as a quantitative tool to probe the physical conditions (e.g. $G_0/n_e \times \sqrt{T_{\text{gas}}}$) in the emitting regions. We expect that this study will be of fundamental value for the interpretation of *Spitzer* data as well as future *Sofia* and *JWST* observations of galaxies in the nearby and early universe.

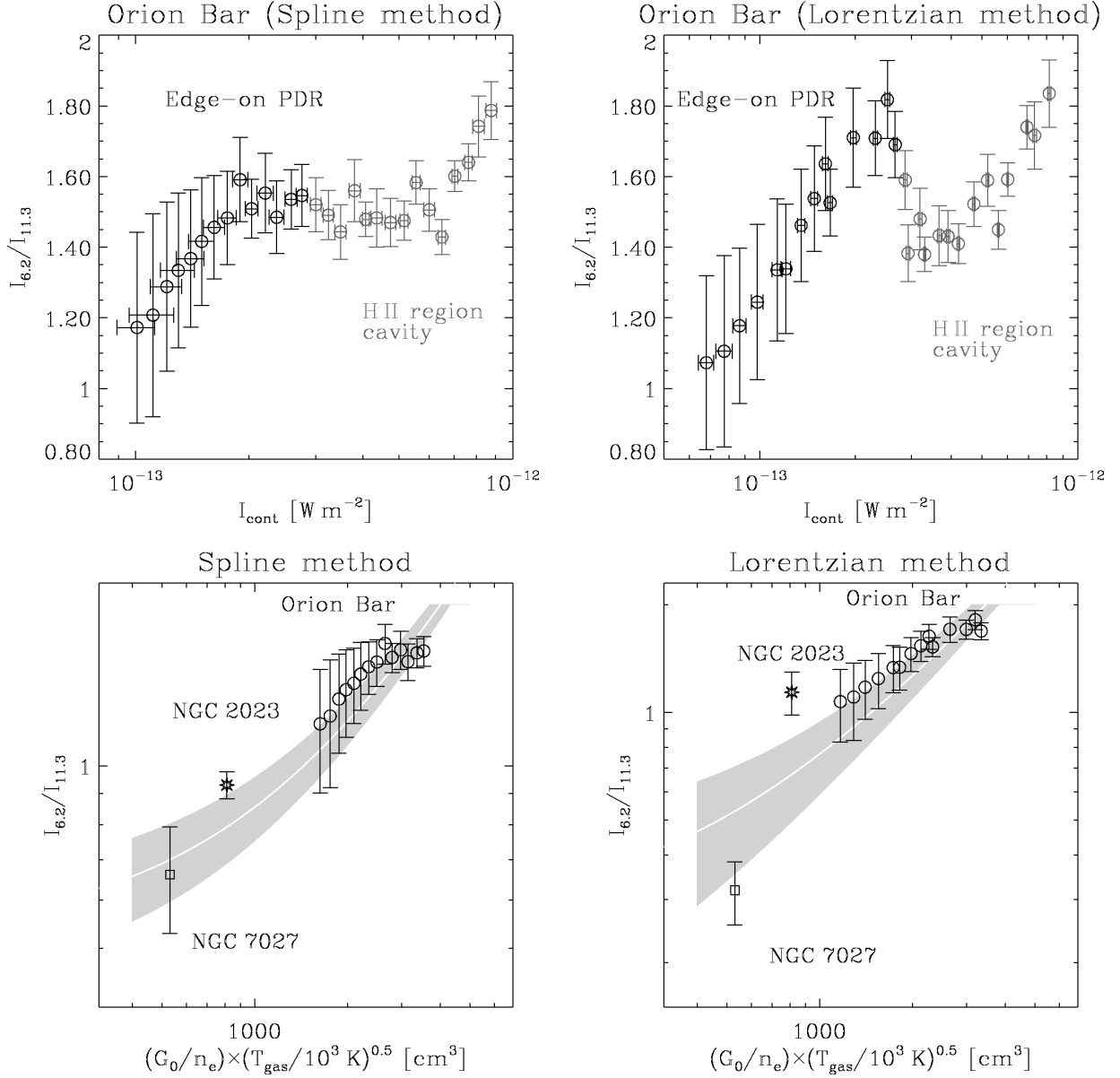


Fig. 20.— Empirical calibration of the band ratio. The two upper panels show the variation of the band ratio inside the Orion bar, as a function of the VSG intensity. The black error bars correspond to the edge-on PDR, and the grey error bars, to the H II region cavity. The two lower panels show the final calibration, including NGC 2023 and NGC 7027. We kept only the edge-on PDR measurements, in the Orion bar.

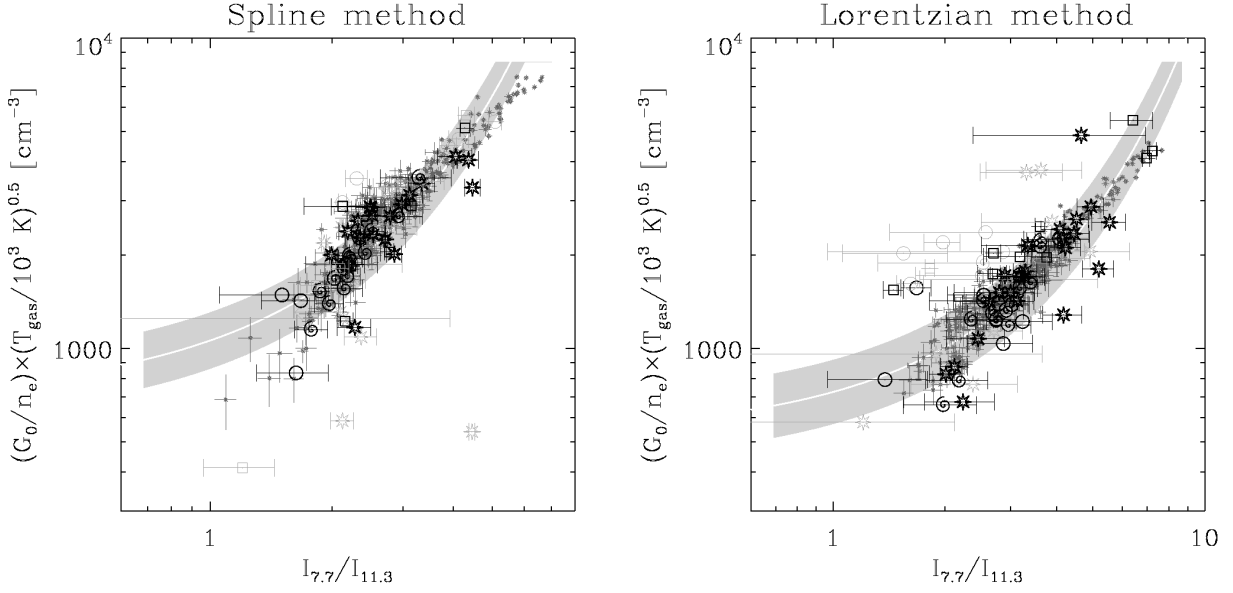


Fig. 21.— Determination of $G_0/n_e \times \sqrt{T_{\text{gas}}}$ for the sources in our sample. These figures are similar to Fig. 3, where the $I_{6.2}/I_{11.3}$ has been converted into $G_0/n_e \times \sqrt{T_{\text{gas}}}$ using Eq. (5). The same symbol conventions are adopted as in Fig. 3. The small additional symbols are the spatial variations within M 82.

6. SUMMARY AND CONCLUSION

We presented the results of a systematic study aimed at understanding the main properties of the mid-IR features in different astrophysical environments. It is based on observations of Galactic regions and galaxies of various types, observed by the satellites *ISO* and *Spitzer*. We have developed two distinct methods of spectral decomposition with different hypotheses, in order to test the robustness of our trends, and overcome eventual biases. These two methods have shown similar trends between the physical quantities that we have studied. We explored the variations of the different mid-IR features between the wavelengths 5 and 16 μm , among integrated spectra of galaxies, and inside galaxies and Galactic regions. Our main results are the followings.

1. We find that the 6.2, 7.7, 8.6 μm features are essentially tied together, while the ratio of these bands to the 11.3 μm feature can vary by one order of magnitude, in our sample. These variations are seen both inside individual sources (like M 82, M 17, the Orion bar, 30 Doradus, etc.), as well as among integrated spectra. In general, the $I_{6.2}/I_{11.3}$ ratio is spatially correlated with the power radiated by the PAHs. It indicates that the ratio $I_{6.2}/I_{11.3}$ is higher in regions of intense star formation.

2. With the help of a stochastic heating model and realistic absorption efficiencies, we show that the variations of the mid-IR features are essentially due to the variation of the fraction of ionized PAHs. We conclude that the properties of the PAHs, throughout our sample, are remarkably universal. In particular, we rule out both the modification of the grain size distribution, and the extinction by the $9.7 \mu\text{m}$ silicate feature, as an explanation of these variations. Indeed, we show that a modification of the size distribution could explain the observed variation of the $I_{6.2}/I_{11.3}$ ratio. However, it would cause the $I_{6.2}/I_{7.7}$ and $I_{6.2}/I_{8.6}$ (and $I_{3.3}/I_{11.3}$) ratios to vary significantly and to be correlated with the $I_{6.2}/I_{11.3}$, contradicting our observations. Similarly, a deep absorption by the silicate feature would vary the $I_{6.2}/I_{11.3}$ ratio, but it would decouple the $8.6 \mu\text{m}$ from the 6.2 and $7.7 \mu\text{m}$ features at the same time.
3. The universality of the properties of the PAHs and the fact that the band ratios are mainly sensitive to the charge of the molecules allow us to use these band ratios as a tracer of the physical conditions inside the emitting region. Using a few well-studied Galactic regions (including the spectral image of the Orion bar), we give an empirical relation between $I_{6.2}/I_{11.3}$ and the ratio $G_0/n_e \times \sqrt{T_{\text{gas}}}$.
4. In the case where several regions with different physical conditions are integrated, the band ratios are dependent on the morphology of the ISM, as well as on the evolutionary properties of the illuminating stellar cluster. Thus, we find that the $I_{6.2}/I_{11.3}$ band ratios in the star forming nuclei of M 51 and M 82 are very similar to those in the galactic compact H II regions, IR 15384 and IR 18317, while the halo of M 82 and the spiral arms of M 51 are similar to those in the Galactic reflection nebula NGC 2023. These differences in band ratio reflect differences in the ionization over recombination rate and hence trace back to variations in the ratio of the ionizing radiation field to the electron density.

A. ADDITIONAL TABLE AND FIGURES

Notes on Individual Sources

M 82. (Figs. 7-8) Fig. 7 shows that the correlations inside M 82 are remarkably well articulated. The correlation coefficients (Table 2) are 0.97, for the correlations between $I_{6.2}/I_{11.3}$ and $I_{7.7}/I_{11.3}$. The band ratios inside M 82 follow the general trends observed for the integrated spectra very well. The centroid of the $7.7 \mu\text{m}$ feature is essentially fixed throughout M 82 (Table 2). The ratio $I_{6.2}/I_{11.3}$ follows the spatial distribution of the PAH emission very well, which is maximum in the central bar, where the star

formation occurs. With good confidence ($S/N > 6$), we detect low ratios in the outer regions.

IC 342. (Figs. 22-23) The morphology of the PAH emission (Fig. 37) follows the $^{12}\text{CO}(J=1\rightarrow 0)_{2.6\text{mm}}$ emission which traces out the nuclear ring and ridge associated with the stellar bar Sakamoto et al. (1999). The spectra of this galaxy are much noisier than those of M 82. The correlations are very well defined, with a linear correlation coefficient of $\simeq 0.8$ (Table 2). The deviation of the relation involving the $8.6\ \mu\text{m}$ feature with the *Lorentzian method* (middle right panel of Fig. 22), compared to the general correlation, is due to a systematic over-estimation of the attenuation, in the central region. The average centroid of the $7.7\ \mu\text{m}$ feature is identical for IC 342 and M 82 ($\langle\lambda_{7.7}\rangle \simeq 7.68\ \mu\text{m}$; Table 2).

M 51. (Figs. 10-11) This galaxy is more quiescent than M 82 and IC 342. Its band ratios show less variation (Fig. 10) throughout the galaxy, although they are in good agreement with the general correlations of Fig. 3. The correlation coefficients are $\simeq 0.6$ (Table 2) slightly lower than those for M 82 and IC 342, essentially because of the lower signal-to-noise ratio of the spectra. The spatial distribution of the $I_{6.2}/I_{11.3}$ ratio (Fig. 14) follows the PAH emission remarkably well enhanced along the spiral arms and the bulge. This band ratio reaches its maximum on the central ring and decreases somewhat in the center.

M 83. (Figs. 25-26) M 83 is a spiral galaxy which is similar in several aspects to M 51. Its band ratios (Fig. 25) and the spatial distribution of its PAH emission (Fig. 38) have the same properties qualitatively. The average centroid of the $7.7\ \mu\text{m}$ is identical to that for M 51 and M 83 ($\langle\lambda_{7.7}\rangle \simeq 7.72\ \mu\text{m}$; Table 2).

30 Doradus. (Figs. 28-29) The band ratio correlations measured inside 30 Doradus are significantly dispersed (Fig. 28). The results of the 2 different feature extraction methods are not particularly consistent. This is certainly due to the very low PAH-to-continuum ratio. Indeed, Fig. 39 shows that the spatial distribution of the PAH emission, obtained with the *Lorentzian method*, is different from that obtained with the *Spline method*. In particular, the right panel of Fig. 39 shows 3 bright spots along the bar of 30 Doradus, that are not seen on the left panel. After verification, these are fits of such low PAH-to-continuum ratio pixels that the widths of the PAH bands are not constrained at all. The *Lorentzian method* determines very wide bands whose integrated intensities are significantly overestimated. For the same reason, the highest values of the $I_{6.2}/I_{11.3}$ ratio, with the *Spline method* ($\simeq 2$; Fig. 39), correspond to low values, with the *Lorentzian method* ($\lesssim 0.3$).

M 17. (Figs. 34-35) We encounter the same trouble in the H II region part of M 17 (upper left corner of the images in Fig. 41), as in 30 Doradus. For the same reasons, the $I_{6.2}/I_{11.3}$ ratio is maximum in this region with the *Spline method* ($\simeq 2.5$; Fig. 41), while it is minimum with the *Lorentzian method* ($\lesssim 0.7$). However, the PDR part has relatively high PAH-to-continuum ratios. The band ratio correlations are well defined inside M 17, except for $8.6 \mu\text{m}$, with the *Spline method* (Fig. 34).

The Orion bar. (Figs. 31-32) The PAH-to-continuum ratio is on average higher in this region than in M 17. Thus the fits are better, even along the ionization front. The correlation between band ratios (Fig. 31) are relatively good with linear correlation coefficients around 0.9 (Table 2). The plot of the consistency between the two methods (Fig. 33) shows a few outlying points. These fits are those of the pixels located inside the H II region (upper part of the images in Fig. 40). The spatial distribution of the $I_{6.2}/I_{11.3}$ band ratio decreases on average from the north, where the ionizing stars are located, to the south with the two methods. The average centroid of the $7.7 \mu\text{m}$ feature is similar in M 17 and the Orion bar ($\langle\lambda_{7.7}\rangle \simeq 7.68 \mu\text{m}$; Table 2).

Table 4. Results of the spectral decomposition.

Name		$I_{6.2}$ [10^{-15} W m $^{-2}$]	$I_{7.7}$ [10^{-15} W m $^{-2}$]	$I_{8.6}$ [10^{-15} W m $^{-2}$]	$I_{11.3}$ [10^{-15} W m $^{-2}$]	I_{PAH} [10^{-15} W m $^{-2}$]	I_{cont} [10^{-15} W m $^{-2}$]	$\lambda_{7.7}$ [μ m]	Relia- bility
Haro 11	\mathcal{S}	0.90 \pm 0.09	1.81 \pm 0.18	0.23 \pm 0.02	3.78 \pm 2.15	3.84 \pm 2.15	51.1 \pm 5.1	...	Low
	\mathcal{L}	1.59 \pm 0.16	5.23 \pm 0.52	0.32 \pm 0.03	1.28 \pm 0.13	11.2 \pm 0.6	59.8 \pm 6.0	7.634 \pm 0.025	Low
SMC B1#1	\mathcal{S}	16.2 \pm 2.4	24.1 \pm 3.6	3.09 \pm 0.46	16.0 \pm 2.4	73.8 \pm 35.7	76.8 \pm 11.5	...	High
	\mathcal{L}	33.8 \pm 5.1	70.2 \pm 1.1	16.1 \pm 2.4	51.0 \pm 7.6	205 \pm 14	15.1 \pm 2.3	7.647 \pm 0.025	High
NGC 253	\mathcal{S}	148 \pm 4	293 \pm 11	28.5 \pm 3.7	105 \pm 4	604 \pm 346	(1.74 \pm 0.09) $\times 10^3$...	High
	\mathcal{L}	532 \pm 28	(1.54 \pm 0.06) $\times 10^3$	36.4 \pm 1.7	313 \pm 13	(3.42 \pm 0.08) $\times 10^3$	(1.49 \pm 0.07) $\times 10^3$	7.707 \pm 0.025	High
NGC 253 p	\mathcal{S}	48.5 \pm 2.2	98.0 \pm 6.3	10.2 \pm 0.2	29.1 \pm 1.9	195 \pm 114	823 \pm 44	...	Low
	\mathcal{L}	15.1 \pm 8.3	481 \pm 22	113 \pm 6	114 \pm 6	(1.09 \pm 0.03) $\times 10^3$	(1.00 \pm 0.05) $\times 10^3$	7.702 \pm 0.025	High
NGC 253 e	\mathcal{S}	102 \pm 3	199 \pm 8	19.1 \pm 0.6	78.6 \pm 2.6	420 \pm 238	974 \pm 66	...	High
	\mathcal{L}	324 \pm 22	(1.00 \pm 0.05) $\times 10^3$	228 \pm 13	225 \pm 11	(2.21 \pm 0.06) $\times 10^3$	689 \pm 40	7.711 \pm 0.025	High
SMC N 66	\mathcal{S}	10.3 \pm 0.5	14.0 \pm 0.6	0.34 \pm 0.05	6.09 \pm 0.11	37.0 \pm 19.1	290 \pm 41	...	Low
	\mathcal{L}	82.7 \pm 20.6	99.7 \pm 19.1	57.5 \pm 12.9	64.5 \pm 8.0	340 \pm 34	203 \pm 28	7.619 \pm 0.025	Low
NGC 520	\mathcal{S}	8.38 \pm 0.37	19.6 \pm 0.7	1.00 \pm 0.05	4.50 \pm 0.10	36.6 \pm 22.0	45.4 \pm 4.3	...	High
	\mathcal{L}	38.9 \pm 2.9	107 \pm 5	29.2 \pm 1.9	26.3 \pm 1.7	240 \pm 7	72.3 \pm 5.2	7.748 \pm 0.025	High
NGC 613	\mathcal{S}	7.92 \pm 0.26	13.5 \pm 1.0	1.49 \pm 0.01	4.89 \pm 0.05	30.2 \pm 16.5	74.0 \pm 31.9	...	Low
	\mathcal{L}	19.3 \pm 9.2	40.4 \pm 10.4	7.41 \pm 3.16	15.9 \pm 3.6	112 \pm 18	55.4 \pm 26.4	7.693 \pm 0.025	Low
NGC 613 p	\mathcal{S}	4.03 \pm 0.12	8.35 \pm 0.48	0.72 \pm 0.05	3.88 \pm 0.20	18.3 \pm 10.1	35.9 \pm 10.0	...	High
	\mathcal{L}	12.4 \pm 3.5	32.4 \pm 5.2	6.94 \pm 1.67	12.7 \pm 1.6	79.8 \pm 7.5	33.9 \pm 10.8	7.703 \pm 0.025	High
NGC 891	\mathcal{S}	93.1 \pm 9.3	181 \pm 18	17.0 \pm 1.7	55.0 \pm 5.5	361 \pm 212	304 \pm 30	...	High
	\mathcal{L}	207 \pm 21	605 \pm 61	124 \pm 12	148 \pm 15	(1.34 \pm 0.07) $\times 10^3$	87.1 \pm 8.7	7.705 \pm 0.025	High
NGC 1068	\mathcal{S}	55.5 \pm 5.9	126 \pm 35	20.1 \pm 6.1	59.3 \pm 33.6	287 \pm 152	(4.80 \pm 0.37) $\times 10^3$...	Low
	\mathcal{L}	181 \pm 10	586 \pm 85	131 \pm 16	216 \pm 11	(1.33 \pm 0.09) $\times 10^3$	(4.75 \pm 0.23) $\times 10^3$	7.706 \pm 0.025	Low
NGC 1068 p	\mathcal{S}	\lesssim 10.2	\lesssim 45	5.1 \pm 4.8	\lesssim 31	573 \pm 274	(3.59 \pm 0.34) $\times 10^3$...	Low
	\mathcal{L}	209 \pm 15	352 \pm 80	86.0 \pm 15.0	97.3 \pm 6.0	902 \pm 83	(3.52 \pm 0.19) $\times 10^3$	7.699 \pm 0.025	Low
NGC 1068 e	\mathcal{S}	48.9 \pm 7.1	101 \pm 35	14.3 \pm 6.0	51.1 \pm 36.4	237 \pm 125	(1.01 \pm 0.30) $\times 10^3$...	Low
	\mathcal{L}	313 \pm 43	537 \pm 202	108 \pm 40	115 \pm 13	(1.28 \pm 0.21) $\times 10^3$	859 \pm 136	7.699 \pm 0.025	High
NGC 1097	\mathcal{S}	27.7 \pm 0.1	50.6 \pm 0.01	5.25 \pm 0.15	27.0 \pm 0.8	116 \pm 64	229 \pm 32	...	High
	\mathcal{L}	56.4 \pm 6.9	166 \pm 12	31.0 \pm 3.1	61.7 \pm 4.7	410 \pm 18	127 \pm 18	7.707 \pm 0.025	High
NGC 1097 p	\mathcal{S}	18.7 \pm 0.15	37.7 \pm 1.2	4.25 \pm 0.32	19.1 \pm 1.0	82.8 \pm 46.4	156 \pm 13.8	...	High
	\mathcal{L}	42.8 \pm 3.2	134 \pm 7	29.5 \pm 2.0	48.4 \pm 3.1	319 \pm 9	88.9 \pm 8.0	7.703 \pm 0.025	High
NGC 1140	\mathcal{S}	0.92 \pm 0.05	1.31 \pm 0.01	0.07 \pm 0.02	0.62 \pm 0.01	3.34 \pm 1.73	6.96 \pm 2.16	...	Low
	\mathcal{L}	1.63 \pm 0.66	3.65 \pm 0.81	0.45 \pm 0.13	1.45 \pm 0.17	8.29 \pm 1.17	5.57 \pm 1.71	7.684 \pm 0.025	Low
NGC 1365	\mathcal{S}	38.0 \pm 0.5	76.5 \pm 2.4	9.21 \pm 0.27	34.9 \pm 1.3	177 \pm 94	367 \pm 31	...	High
	\mathcal{L}	89.3 \pm 7.1	253 \pm 13	52.7 \pm 3.8	79.5 \pm 4.4	566 \pm 16	242 \pm 20	7.710 \pm 0.025	High
NGC 1365 p	\mathcal{S}	26.7 \pm 1.1	54.1 \pm 1.9	6.22 \pm 0.21	22.3 \pm 1.2	117 \pm 65	253 \pm 15	...	High
	\mathcal{L}	57.7 \pm 3.1	182 \pm 8	42.3 \pm 2.2	53.2 \pm 2.5	148 \pm 10	71.1 \pm 16.2	7.713 \pm 0.025	High
NGC 1365 e	\mathcal{S}	11.4 \pm 0.02	22.4 \pm 1.0	2.98 \pm 0.10	12.6 \pm 0.7	60.5 \pm 29.6	113 \pm 24	...	High
	\mathcal{L}	18.3 \pm 4.9	61.2 \pm 7.6	11.7 \pm 2.4	30.8 \pm 3.1	148 \pm 10	71.1 \pm 16.2	7.708 \pm 0.025	High
IC 342	\mathcal{S}	36.8 \pm 0.7	62.1 \pm 1.6	9.69 \pm 0.27	26.7 \pm 0.8	141 \pm 78	270 \pm 15	...	High
	\mathcal{L}	62.2 \pm 3.9	182 \pm 8	48.9 \pm 2.6	60.7 \pm 2.6	441 \pm 10	158 \pm 8	7.686 \pm 0.025	High
IC 342 p	\mathcal{S}	16.5 \pm 0.6	28.3 \pm 1.1	3.90 \pm 0.16	11.3 \pm 0.5	62.9 \pm 34.9	135 \pm 6	...	High
	\mathcal{L}	30.4 \pm 1.6	78.0 \pm 3.2	15.2 \pm 0.8	26.9 \pm 1.2	188 \pm 4	87.5 \pm 3.9	7.678 \pm 0.025	High
IC 342 e	\mathcal{S}	20.2 \pm 0.3	33.8 \pm 0.7	5.79 \pm 0.14	15.4 \pm 0.4	78.4 \pm 42.7	135 \pm 12	...	High
	\mathcal{L}	32.8 \pm 3.3	105 \pm 6	34.4 \pm 2.5	33.5 \pm 1.8	257 \pm 8	70.1 \pm 5.4	7.692 \pm 0.025	High
NGC 1569	\mathcal{S}	6.82 \pm 0.03	13.2 \pm 0.1	0.50 \pm 0.08	5.38 \pm 0.12	28.1 \pm 15.8	114 \pm 24	...	Low
	\mathcal{L}	20.2 \pm 9.8	35.7 \pm 10.3	3.21 \pm 1.35	13.9 \pm 2.2	102 \pm 29	91.4 \pm 14.9	7.669 \pm 0.025	Low
NGC 1569 e	\mathcal{S}	5.43 \pm 0.03	10.7 \pm 0.1	0.33 \pm 0.08	4.02 \pm 0.10	22.5 \pm 12.7	55.8 \pm 23.9	...	Low
	\mathcal{L}	13.3 \pm 9.6	29.5 \pm 12.3	3.06 \pm 1.98	10.3 \pm 2.5	69.7 \pm 38.2	46.2 \pm 15.2	7.679 \pm 0.025	Low
NGC 1808	\mathcal{S}	86.8 \pm 8.7	147 \pm 15	15.0 \pm 1.5	59.1 \pm 5.9	321 \pm 181	497 \pm 50	...	High

Table 4—Continued

Name		$I_{6.2}$ [10^{-15} W m $^{-2}$]	$I_{7.7}$ [10^{-15} W m $^{-2}$]	$I_{8.6}$ [10^{-15} W m $^{-2}$]	$I_{11.3}$ [10^{-15} W m $^{-2}$]	I_{PAH} [10^{-15} W m $^{-2}$]	I_{cont} [10^{-15} W m $^{-2}$]	$\lambda_{7.7}$ [μm]	Relia- bility
Orion bar D8	\mathcal{L}	180 \pm 18	487 \pm 49	102 \pm 10	185 \pm 19	(1.24 \pm 0.06) $\times 10^3$	274 \pm 27	7.710 \pm 0.025	High
	\mathcal{S}	338 \pm 3	632 \pm 7	77.8 \pm 4.4	301 \pm 12	(1.45 \pm 0.78) $\times 10^3$	(9.80 \pm 0.11) $\times 10^3$...	Low
	\mathcal{L}	590 \pm 13	912 \pm 5	73.8 \pm 0.8	501 \pm 12	(2.79 \pm 0.03) $\times 10^3$	(9.25 \pm 0.08) $\times 10^3$	7.645 \pm 0.025	Low
Orion bar D5	\mathcal{S}	532 \pm 3	(1.05 \pm 0.01) $\times 10^3$	131 \pm 2	470 \pm 3	(2.33 \pm 1.28) $\times 10^3$	(5.84 \pm 0.13) $\times 10^3$...	High
	\mathcal{L}	981 \pm 18	(2.49 \pm 0.02) $\times 10^3$	580 \pm 7	737 \pm 7	(5.97 \pm 0.04) $\times 10^3$	(4.94 \pm 0.07) $\times 10^3$	7.670 \pm 0.025	High
Orion bar D2	\mathcal{S}	107 \pm 10	186 \pm 1	21.0 \pm 0.1	102 \pm 8	468 \pm 240	(2.67 \pm 0.12) $\times 10^3$...	Low
	\mathcal{L}	233 \pm 10	491 \pm 8	70.1 \pm 1.6	182 \pm 5	(1.58 \pm 0.03) $\times 10^3$	(2.18 \pm 0.10) $\times 10^3$	7.680 \pm 0.025	High
30 Doradus	\mathcal{S}	205 \pm 1	405 \pm 8	12.4 \pm 0.3	98.2 \pm 3.5	78.4 \pm 46.6	(1.39 \pm 0.06) $\times 10^4$...	Low
	\mathcal{L}	(1.12 \pm 0.07) $\times 10^3$	(1.68 \pm 0.07) $\times 10^3$	781 \pm 36	(1.04 \pm 0.04) $\times 10^3$	(5.73 \pm 0.13) $\times 10^3$	(1.23 \pm 0.05) $\times 10^4$	7.616 \pm 0.025	Low
30 Doradus p	\mathcal{S}	25.3 \pm 1.2	56.0 \pm 0.1	0.73 \pm 0.16	11.0 \pm 0.4	99.7 \pm 62.6	(2.84 \pm 0.11) $\times 10^3$...	Low
	\mathcal{L}	184 \pm 23	264 \pm 18	122 \pm 8	134 \pm 6	873 \pm 36	(2.61 \pm 0.10) $\times 10^3$	7.711 \pm 0.025	Low
30 Doradus e	\mathcal{S}	164 \pm 1	315 \pm 4	11.7 \pm 0.2	81.2 \pm 2.9	624 \pm 366	(9.62 \pm 0.40) $\times 10^3$...	Low
	\mathcal{L}	839 \pm 61	(1.34 \pm 0.07) $\times 10^3$	479 \pm 26	798 \pm 33	(4.30 \pm 0.12) $\times 10^3$	(8.49 \pm 0.35) $\times 10^3$	7.624 \pm 0.025	High
NGC 2023	\mathcal{S}	54.1 \pm 2.3	125 \pm 5	8.25 \pm 0.11	58.2 \pm 0.5	263 \pm 149	263 \pm 55	...	High
	\mathcal{L}	120 \pm 9	284 \pm 8	60.9 \pm 3.7	106 \pm 7	705 \pm 19	99.7 \pm 14	7.743 \pm 0.025	High
He 2-10	\mathcal{S}	6.74 \pm 0.67	14.7 \pm 1.5	2.01 \pm 0.20	5.90 \pm 0.59	31.1 \pm 17.4	109 \pm 11	...	Low
	\mathcal{L}	14.4 \pm 1.4	36.1 \pm 3.6	5.50 \pm 0.55	14.2 \pm 1.4	85.9 \pm 4.3	125 \pm 13	7.662 \pm 0.025	High
M 82	\mathcal{S}	992 \pm 36	(2.01 \pm 0.07) $\times 10^3$	231 \pm 8	602 \pm 22	(4.09 \pm 2.34) $\times 10^3$	(6.74 \pm 0.29) $\times 10^3$...	High
	\mathcal{L}	(2.68 \pm 0.10) $\times 10^3$	(7.62 \pm 0.27) $\times 10^3$	(1.80 \pm 0.07) $\times 10^3$	(2.23 \pm 0.09) $\times 10^3$	(1.72 \pm 0.03) $\times 10^4$	(5.82 \pm 0.24) $\times 10^3$	7.697 \pm 0.025	High
M 82 p	\mathcal{S}	369 \pm 18	790 \pm 33	88.4 \pm 3.5	195 \pm 11	(1.53 \pm 0.90) $\times 10^3$	(3.16 \pm 0.12) $\times 10^3$...	High
	\mathcal{L}	983 \pm 42	(2.92 \pm 0.11) $\times 10^3$	697 \pm 26	701 \pm 27	(6.35 \pm 0.12) $\times 10^3$	(3.02 \pm 0.11) $\times 10^3$	7.695 \pm 0.025	High
M 82 e	\mathcal{S}	819 \pm 30	(1.64 \pm 0.06) $\times 10^3$	192 \pm 7	527 \pm 20	(3.39 \pm 1.93) $\times 10^3$	(5.22 \pm 0.24) $\times 10^3$...	High
	\mathcal{L}	(1.99 \pm 0.08) $\times 10^3$	(5.71 \pm 0.21) $\times 10^3$	(1.21 \pm 0.04) $\times 10^3$	(1.26 \pm 0.05) $\times 10^3$	(1.21 \pm 0.02) $\times 10^4$	(2.82 \pm 0.13) $\times 10^3$	7.701 \pm 0.025	High
NGC 3256	\mathcal{S}	24.7 \pm 0.3	45.5 \pm 4.2	5.29 \pm 0.02	19.4 \pm 0.2	97.4 \pm 55.6	193 \pm 27	...	High
	\mathcal{L}	65.0 \pm 8.9	183 \pm 14	48.6 \pm 5.9	57.9 \pm 4.5	411 \pm 19	181 \pm 20	7.701 \pm 0.025	High
NGC 3256 p	\mathcal{S}	6.16 \pm 0.40	11.0 \pm 0.3	1.05 \pm 0.02	4.37 \pm 0.25	23.1 \pm 13.4	52.1 \pm 10.2	...	High
	\mathcal{L}	18.3 \pm 3.9	45.4 \pm 5.8	9.88 \pm 2.31	13.6 \pm 1.7	105 \pm 10	51.7 \pm 7.3	7.703 \pm 0.025	High
NGC 3256 e	\mathcal{S}	14.5 \pm 1.5	24.5 \pm 0.1	3.19 \pm 0.01	12.3 \pm 0.1	55.7 \pm 32.1	101 \pm 26	...	High
	\mathcal{L}	38.0 \pm 9.3	104 \pm 13	29.2 \pm 6.0	37.1 \pm 4.6	245 \pm 19	89.8 \pm 18.8	7.699 \pm 0.025	High
Mrk 33	\mathcal{S}	2.51 \pm 0.25	5.12 \pm 0.51	0.31 \pm 0.03	3.14 \pm 0.31	11.6 \pm 6.5	27.8 \pm 2.8	...	High
	\mathcal{L}	3.88 \pm 0.39	14.2 \pm 0.14	2.35 \pm 0.24	4.94 \pm 0.49	30.4 \pm 1.6	25.4 \pm 2.5	7.721 \pm 0.025	High
Arp 299	\mathcal{S}	9.42 \pm 0.72	16.8 \pm 1.0	1.93 \pm 0.01	6.10 \pm 0.20	37.2 \pm 20.4	223 \pm 27	...	Low
	\mathcal{L}	28.0 \pm 6.6	43.7 \pm 5.7	4.99 \pm 0.82	13.2 \pm 1.6	147 \pm 18	413 \pm 36	7.669 \pm 0.025	Low
UM 448	\mathcal{S}	0.83 \pm 0.08	1.39 \pm 0.14	0.27 \pm 0.03	0.83 \pm 0.08	3.59 \pm 1.85	11.4 \pm 1.1	...	High
	\mathcal{L}	1.34 \pm 0.13	4.92 \pm 0.49	0.90 \pm 0.09	1.52 \pm 0.15	10.0 \pm 0.6	9.95 \pm 1.0	7.670 \pm 0.025	High
IR 12331	\mathcal{S}	38.0 \pm 4.2	69.4 \pm 1.9	7.11 \pm 1.20	23.2 \pm 0.7	160 \pm 84	869 \pm 62	...	Low
	\mathcal{L}	115 \pm 7	247 \pm 6	34.5 \pm 3.2	38.5 \pm 4.1	624 \pm 20	765 \pm 28	7.696 \pm 0.025	High
NGC 4945	\mathcal{S}	65.7 \pm 1.3	182 \pm 7	11.6 \pm 0.3	40.7 \pm 0.3	310 \pm 198	393 \pm 35	...	High
	\mathcal{L}	260 \pm 16	(1.15 \pm 0.05) $\times 10^3$	186 \pm 11	222 \pm 12	(2.15 \pm 0.05) $\times 10^3$	389 \pm 29	7.713 \pm 0.025	High
NGC 4945 p	\mathcal{S}	29.6 \pm 0.1	94.2 \pm 3.9	3.72 \pm 0.03	10.0 \pm 0.1	149 \pm 100	156 \pm 12	...	High
	\mathcal{L}	322 \pm 15	(1.15 \pm 0.05) $\times 10^3$	195 \pm 11	208 \pm 13	(2.22 \pm 0.05) $\times 10^3$	370 \pm 23	7.709 \pm 0.025	High
NGC 4945 e	\mathcal{S}	36.5 \pm 0.7	87.7 \pm 3.6	7.89 \pm 0.19	30.7 \pm 1.1	164 \pm 100	237 \pm 31	...	High
	\mathcal{L}	90.1 \pm 9.6	413 \pm 23	87.5 \pm 7.7	99.1 \pm 6.4	826 \pm 28	136 \pm 16	7.713 \pm 0.025	High
Centaurus A	\mathcal{S}	17.0 \pm 0.2	26.0 \pm 0.1	2.66 \pm 0.14	13.6 \pm 0.2	61.1 \pm 34.0	219 \pm 33	...	Low
	\mathcal{L}	30.2 \pm 5.8	112 \pm 13	27.2 \pm 1.3	50.3 \pm 5.0	282 \pm 16	219 \pm 30	7.696 \pm 0.025	High
Centaurus A e	\mathcal{S}	14.3 \pm 0.1	22.7 \pm 0.1	2.07 \pm 0.12	10.7 \pm 0.1	51.3 \pm 29.0	97.2 \pm 32.0	...	Low
	\mathcal{L}	23.8 \pm 7.4	87.3 \pm 14.3	21.8 \pm 5.8	36.7 \pm 5.7	219 \pm 19	64.3 \pm 20.4	7.695 \pm 0.025	Low
M 51	\mathcal{S}	64.1 \pm 0.9	123 \pm 3	12.9 \pm 0.4	57.2 \pm 1.7	264 \pm 151	435 \pm 49	...	High
	\mathcal{L}	125 \pm 10	398 \pm 20	76.0 \pm 5.1	131 \pm 8	843 \pm 25	251 \pm 35	7.716 \pm 0.025	High

Table 4—Continued

Name		$I_{6.2}$ [10^{-15} W m $^{-2}$]	$I_{7.7}$ [10^{-15} W m $^{-2}$]	$I_{8.6}$ [10^{-15} W m $^{-2}$]	$I_{11.3}$ [10^{-15} W m $^{-2}$]	I_{PAH} [10^{-15} W m $^{-2}$]	I_{cont} [10^{-15} W m $^{-2}$]	$\lambda_{7.7}$ [μ m]	Relia- bility
M 51 p	<i>S</i>	22.6 \pm 0.5	42.7 \pm 0.8	4.93 \pm 0.1	21.0 \pm 0.5	93.6 \pm 52.9	161 \pm 17	...	High
	<i>L</i>	46.0 \pm 3.9	145 \pm 8	28.8 \pm 2.1	49.5 \pm 2.7	326 \pm 10	82.4 \pm 10.6	7.721 \pm 0.025	High
M 51 e	<i>S</i>	34.9 \pm 0.4	68.4 \pm 1.0	6.76 \pm 0.19	30.7 \pm 0.8	145 \pm 83	231 \pm 41	...	High
	<i>L</i>	61.6 \pm 8.4	212 \pm 15	41.7 \pm 4.4	71.5 \pm 5.4	436 \pm 19	141 \pm 32	7.713 \pm 0.025	High
M 83	<i>S</i>	152 \pm 3	291 \pm 9	33.9 \pm 1.4	130 \pm 5	656 \pm 357	901 \pm 174	...	High
	<i>L</i>	304 \pm 22	810 \pm 48	147 \pm 14	343 \pm 30	(1.79 \pm 0.06) $\times 10^3$	622 \pm 154	7.708 \pm 0.025	High
M 83 p	<i>S</i>	60.4 \pm 2.8	117 \pm 5	14.2 \pm 0.5	52.9 \pm 2.7	260 \pm 143	458 \pm 28	...	High
	<i>L</i>	163 \pm 8	430 \pm 18	103 \pm 5	119 \pm 5	931 \pm 22	311 \pm 19	7.707 \pm 0.025	High
M 83 e	<i>S</i>	99.4 \pm 1.9	187 \pm 6	21.1 \pm 0.9	84.3 \pm 3.2	426 \pm 230	501 \pm 156	...	High
	<i>L</i>	163 \pm 16	540 \pm 40	105 \pm 14	247 \pm 28	(1.21 \pm 0.06) $\times 10^3$	180 \pm 94	7.712 \pm 0.025	High
Circinus	<i>S</i>	79.1 \pm 0.5	211 \pm 6	24.8 \pm 0.6	89.4 \pm 5.5	421 \pm 244	(22.8 \pm 1.0) $\times 10^3$...	Low
	<i>L</i>	347 \pm 18	(1.05 \pm 0.04) $\times 10^3$	173 \pm 8	494 \pm 20	(2.55 \pm 0.05) $\times 10^3$	(3.58 \pm 0.14) $\times 10^3$	7.684 \pm 0.025	High
Circinus e	<i>S</i>	64.2 \pm 0.4	161 \pm 4	20.4 \pm 0.4	70.5 \pm 5.1	330 \pm 188	945 \pm 67	...	Low
	<i>L</i>	261 \pm 19	774 \pm 38	187 \pm 11	385 \pm 19	(1.95 \pm 0.05) $\times 10^3$	(1.13 \pm 0.06) $\times 10^3$	7.688 \pm 0.025	High
Arp 220	<i>S</i>	0.48 \pm 0.03	6.33 \pm 0.37	(3.63 \pm 1.72) $\times 10^{-2}$	1.50 \pm 0.02	11.5 \pm 7.1	531 \pm 214	...	Low
	<i>L</i>	\lesssim 59	68.5 \pm 23.7	43.7 \pm 32.4	36.2 \pm 21.1	259 \pm 76	258 \pm 62	7.704 \pm 0.025	Low
Arp 220 p	<i>S</i>	0.63 \pm 0.14	4.00 \pm 0.05	\lesssim 4.4 $\times 10^{-2}$	0.90 \pm 0.01	6.64 \pm 4.23	34.9 \pm 9.9	...	Low
	<i>L</i>	31.6 \pm 21.7	68.7 \pm 17.6	78.3 \pm 38.7	57.0 \pm 28.8	334 \pm 73	247 \pm 41	7.715 \pm 0.025	Low
IR 15384	<i>S</i>	315 \pm 2	608 \pm 6	51.4 \pm 2.8	142 \pm 3	(1.22 \pm 0.70) $\times 10^3$	(3.60 \pm 0.07) $\times 10^3$...	High
	<i>L</i>	711 \pm 13	(2.13 \pm 0.02) $\times 10^3$	304 \pm 0.07	305 \pm 4	(4.32 \pm 0.03) $\times 10^3$	(2.89 \pm 0.03) $\times 10^3$	7.674 \pm 0.025	High
NGC 6240	<i>S</i>	4.22 \pm 0.06	9.05 \pm 0.01	0.91 \pm 0.05	3.33 \pm 0.04	18.2 \pm 10.6	51.2 \pm 6.1	...	High
	<i>L</i>	14.1 \pm 2.6	43.2 \pm 4.0	6.42 \pm 1.05	17.6 \pm 1.5	104 \pm 6	96.0 \pm 8.5	7.725 \pm 0.025	High
NGC 6240 p	<i>S</i>	2.88 \pm 0.13	5.78 \pm 0.17	0.49 \pm 0.05	1.94 \pm 0.02	11.4 \pm 6.8	32.6 \pm 3.0	...	High
	<i>L</i>	10.3 \pm 1.3	30.1 \pm 2.0	3.78 \pm 0.43	9.21 \pm 0.63	66.3 \pm 2.8	59.4 \pm 4.4	7.722 \pm 0.025	High
IR 18317	<i>S</i>	292 \pm 17	527 \pm 4	44.7 \pm 0.1	122 \pm 5	(1.07 \pm 0.62) $\times 10^3$	(3.70 \pm 0.87) $\times 10^3$...	Low
	<i>L</i>	671 \pm 14	(1.99 \pm 0.02) $\times 10^3$	256 \pm 3	275 \pm 4	(4.18 \pm 0.03) $\times 10^3$	(2.93 \pm 0.05) $\times 10^3$	7.681 \pm 0.025	High
NGC 6946	<i>S</i>	81.4 \pm 2.8	156 \pm 6	16.0 \pm 0.5	62.1 \pm 2.4	322 \pm 188	433 \pm 47	...	High
	<i>L</i>	173 \pm 9	527 \pm 24	88.7 \pm 5.6	165 \pm 11	(1.10 \pm 0.03) $\times 10^3$	192 \pm 24	7.713 \pm 0.025	High
NGC 6946 p	<i>S</i>	24.8 \pm 1.8	51.7 \pm 3.3	4.62 \pm 0.04	17.6 \pm 1.3	100 \pm 60	162 \pm 10	...	High
	<i>L</i>	77.9 \pm 4.1	211 \pm 8	42.3 \pm 2.1	58.4 \pm 4.3	462 \pm 11	85.5 \pm 4.6	7.714 \pm 0.025	High
NGC 6946 e	<i>S</i>	56.8 \pm 1.8	105 \pm 4	11.4 \pm 0.4	44.6 \pm 1.8	222 \pm 128	273 \pm 39	...	High
	<i>L</i>	105 \pm 6	327 \pm 17	52.6 \pm 4.0	119 \pm 9	687 \pm 21	122 \pm 22	7.712 \pm 0.025	High
NGC 7027	<i>S</i>	1.00 \pm 0.10	1.82 \pm 0.18	0.14 \pm 0.02	1.52 \pm 0.15	6.84 \pm 0.68	33.4 \pm 3.3	...	Low
	<i>L</i>	1.38 \pm 0.14	4.05 \pm 0.41	0.48 \pm 0.05	4.34 \pm 0.43	17.0 \pm 0.7	27.0 \pm 2.7	7.774 \pm 0.025	High
IR 22308	<i>S</i>	102 \pm 2	236 \pm 3	25.0 \pm 1.0	85.1 \pm 1.3	485 \pm 273	906 \pm 75	...	High
	<i>L</i>	191 \pm 5	572 \pm 10.9	100 \pm 2	153 \pm 10	(1.31 \pm 0.02) $\times 10^3$	629 \pm 26	7.684 \pm 0.025	High
IR 23030	<i>S</i>	75.4 \pm 8.7	136 \pm 3	17.4 \pm 0.4	54.0 \pm 2.3	301 \pm 166	(1.36 \pm 0.06) $\times 10^3$...	Low
	<i>L</i>	135 \pm 5	188 \pm 5	21.5 \pm 0.6	129 \pm 5	736 \pm 15	(1.13 \pm 0.03) $\times 10^3$	7.649 \pm 0.025	High
IR 23133	<i>S</i>	233 \pm 6	496 \pm 2	66.8 \pm 0.4	158 \pm 1	997 \pm 575	(2.88 \pm 0.10) $\times 10^3$...	High
	<i>L</i>	493 \pm 16	(1.18 \pm 0.02) $\times 10^3$	216 \pm 2	(2.71 \pm 0.03) $\times 10^3$	(2.71 \pm 0.03) $\times 10^3$	(2.46 \pm 0.04) $\times 10^3$	7.674 \pm 0.025	High
IR 23128	<i>S</i>	0.82 \pm 0.18	2.43 \pm 0.12	0.27 \pm 0.09	1.14 \pm 0.02	6.35 \pm 3.09	26.4 \pm 5.5	...	Low
	<i>L</i>	5.24 \pm 1.95	13.1 \pm 2.6	2.24 \pm 0.63	3.38 \pm 0.54	35.7 \pm 5.2	35.4 \pm 5.5	7.681 \pm 0.025	Low
IR 23128 p	<i>S</i>	0.79 \pm 0.02	1.69 \pm 0.07	0.25 \pm 0.01	0.74 \pm 0.01	4.23 \pm 2.10	11.9 \pm 2.6	...	Low
	<i>L</i>	1.91 \pm 0.56	7.23 \pm 1.06	2.57 \pm 0.56	1.47 \pm 0.20	20.8 \pm 1.6	6.66 \pm 0.90	7.688 \pm 0.025	Low
NGC 7714	<i>S</i>	3.17 \pm 0.32	6.00 \pm 0.60	0.90 \pm 0.09	2.78 \pm 0.28	13.8 \pm 7.4	43.5 \pm 4.4	...	High
	<i>L</i>	5.15 \pm 0.51	14.9 \pm 1.5	2.75 \pm 0.28	5.34 \pm 0.53	34.8 \pm 1.7	36.4 \pm 3.6	7.681 \pm 0.025	High

Note. — We consider that a given fit has a “high” reliability, if $S/N \geq 6$ at $\lambda = 7.7 \mu\text{m}$, and $I_{\text{PAH}}/I_{\text{cont}} \geq 0.3$ with the *Spline method*, and $I_{\text{PAH}}/I_{\text{cont}} \geq 0.5$ with the *Lorentzian method*. Otherwise, the reliability is “low”.

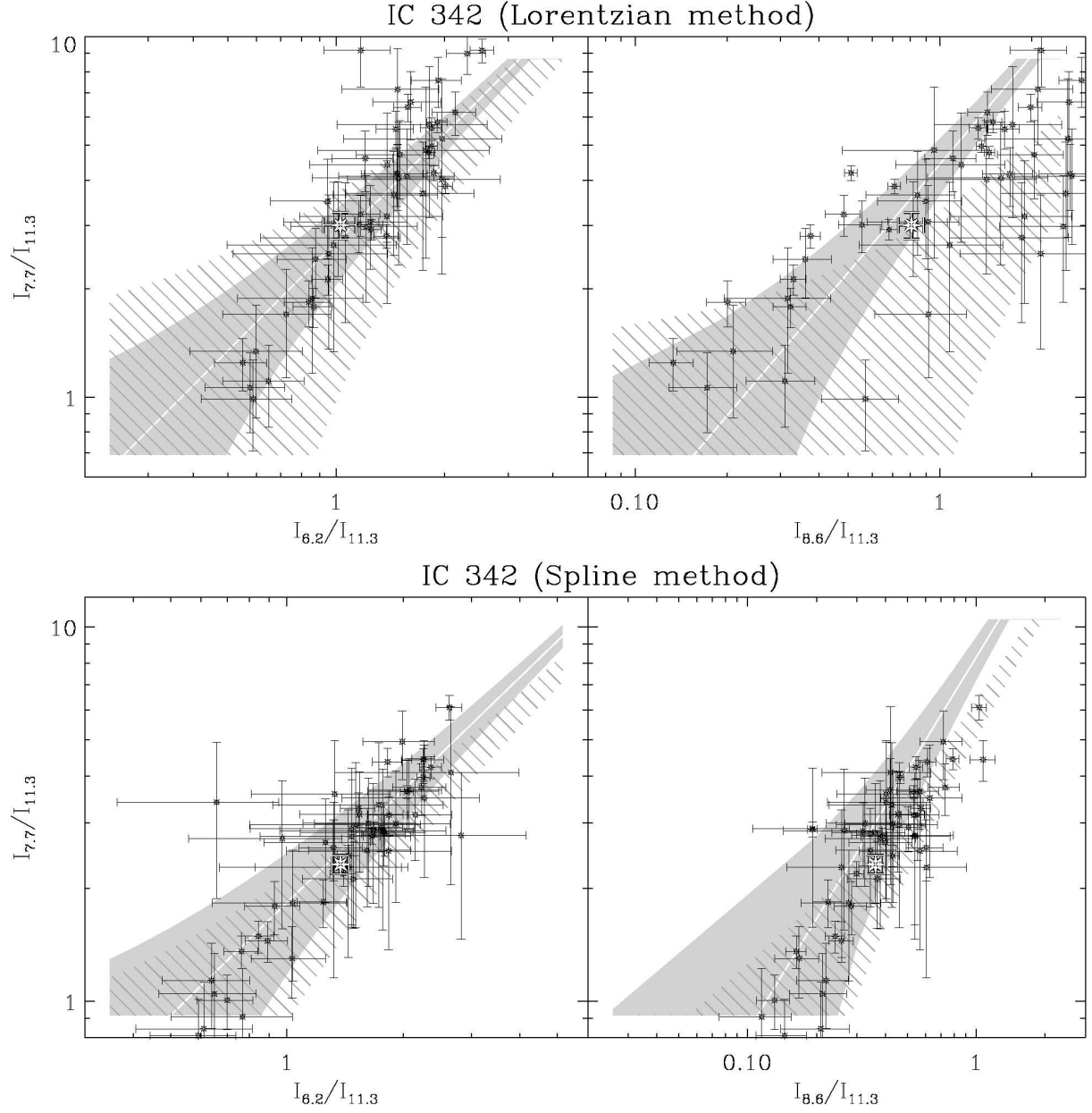


Fig. 22.— PAH band ratios within IC 342. The same symbol conventions are adopted as in Fig. 7.

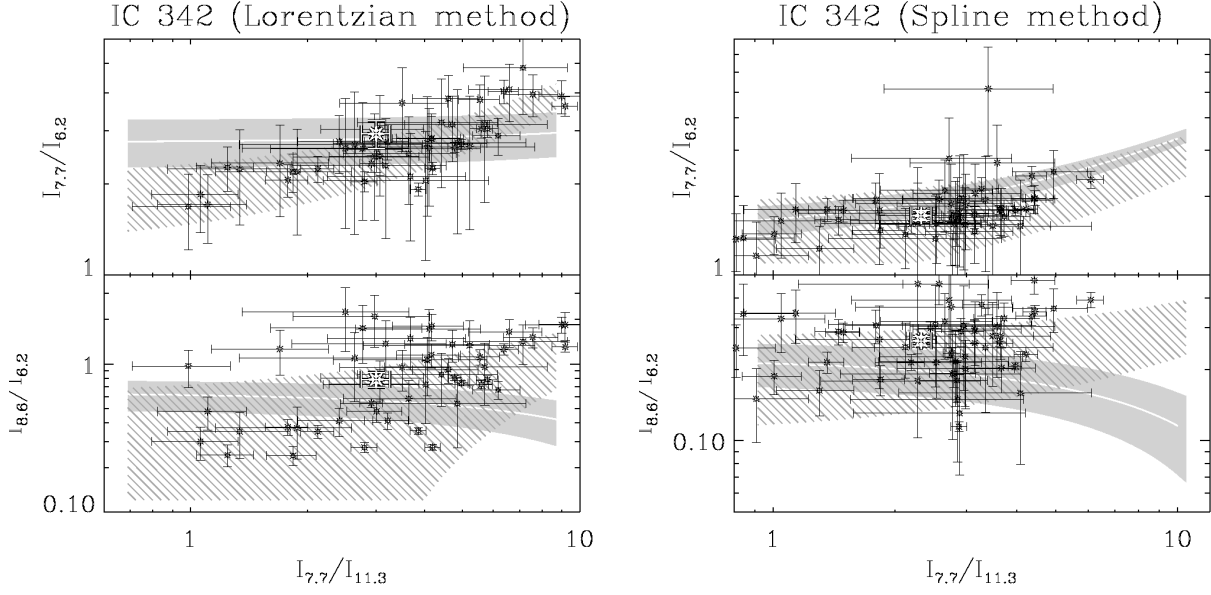


Fig. 23.— PAH band ratios within IC 342 (continued).

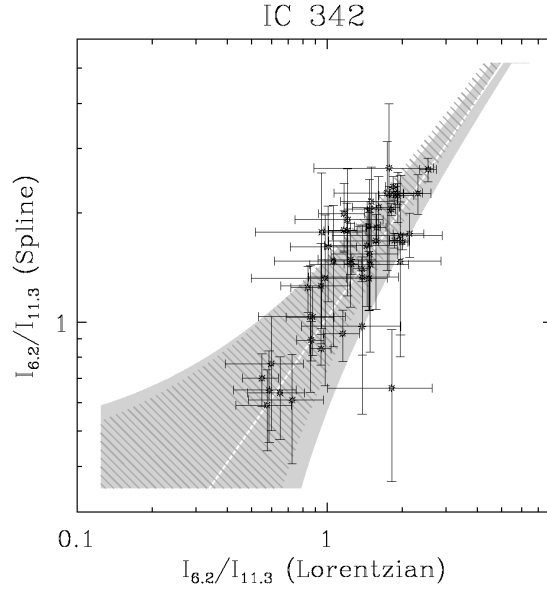


Fig. 24.— Comparison between the two methods in IC 342. The same symbol conventions are adopted as in Fig. 7.

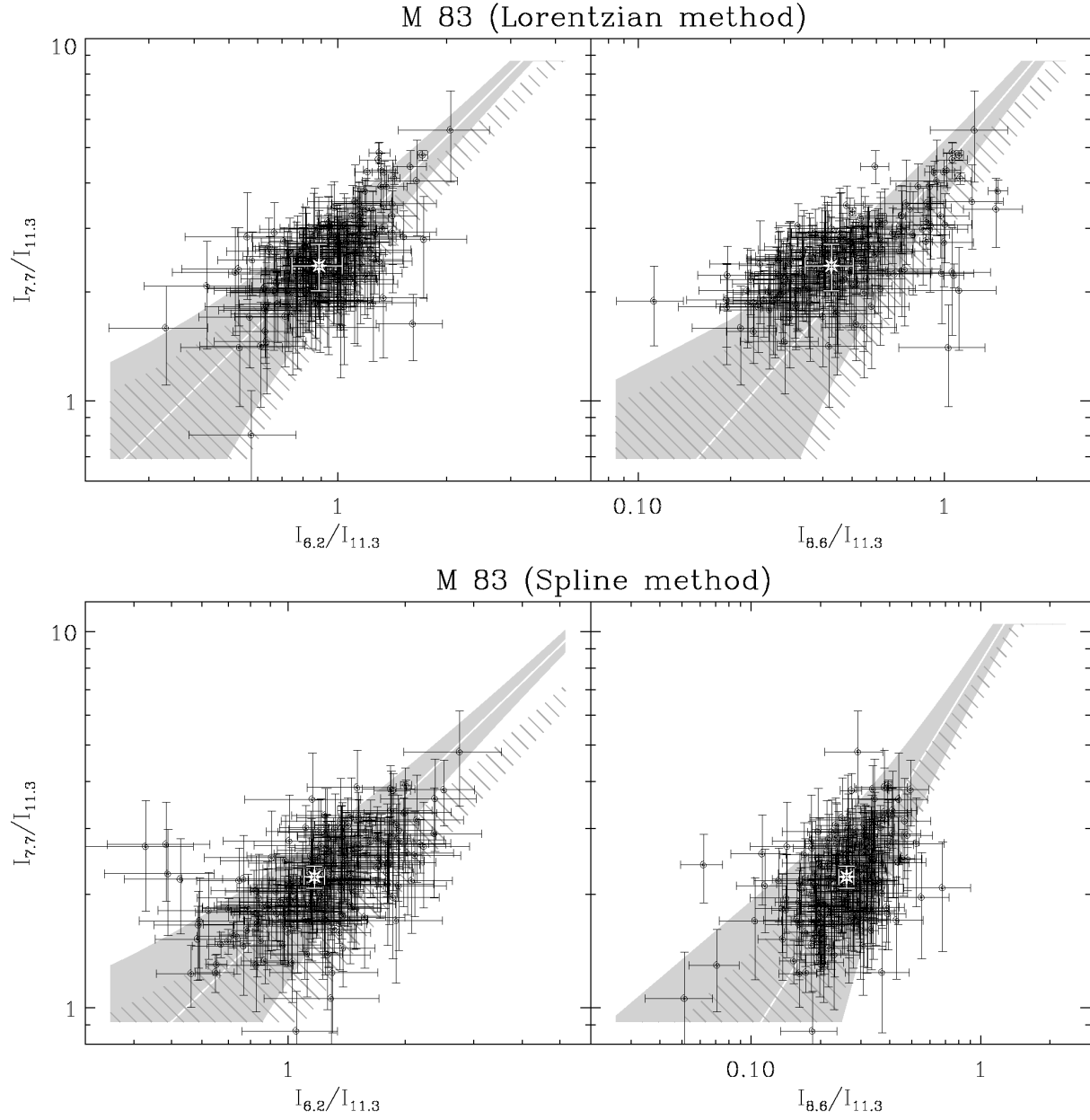


Fig. 25.— PAH band ratios within M 83. The same symbol conventions are adopted as in Fig. 7.

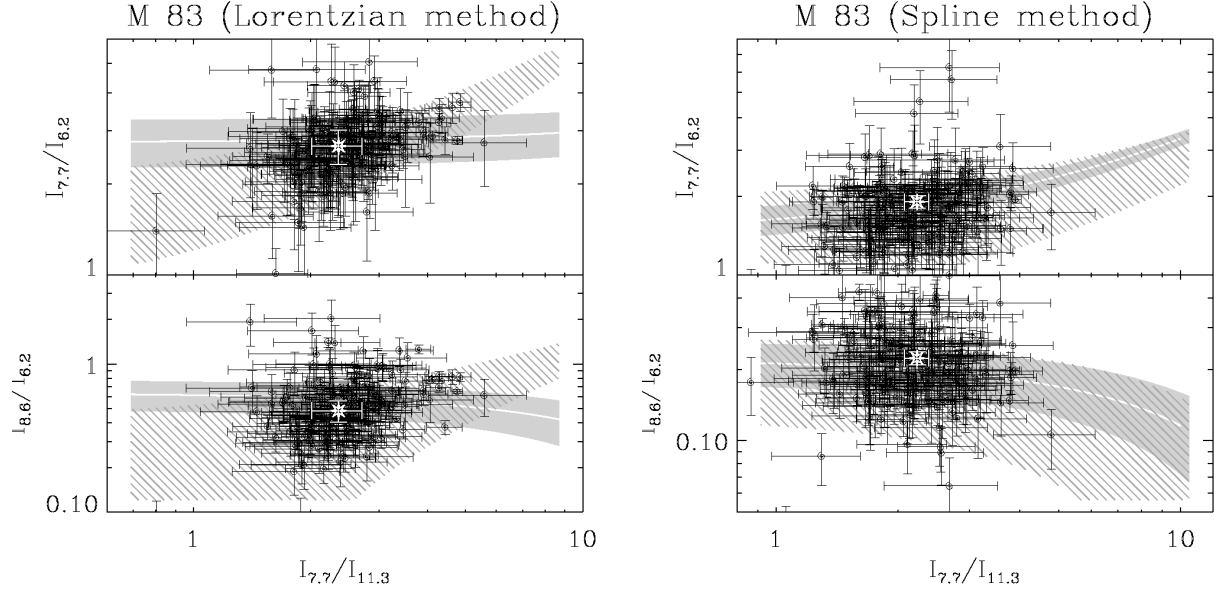


Fig. 26.— PAH band ratios within M 83 (continued).

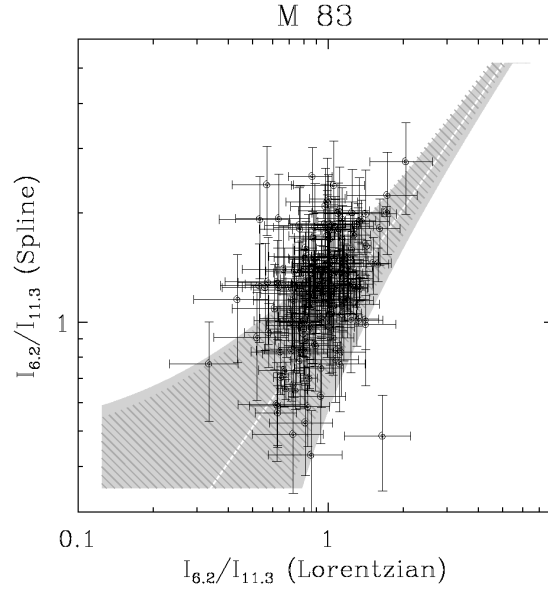


Fig. 27.— Comparison between the two methods in M 83. The same symbol conventions are adopted as in Fig. 7.

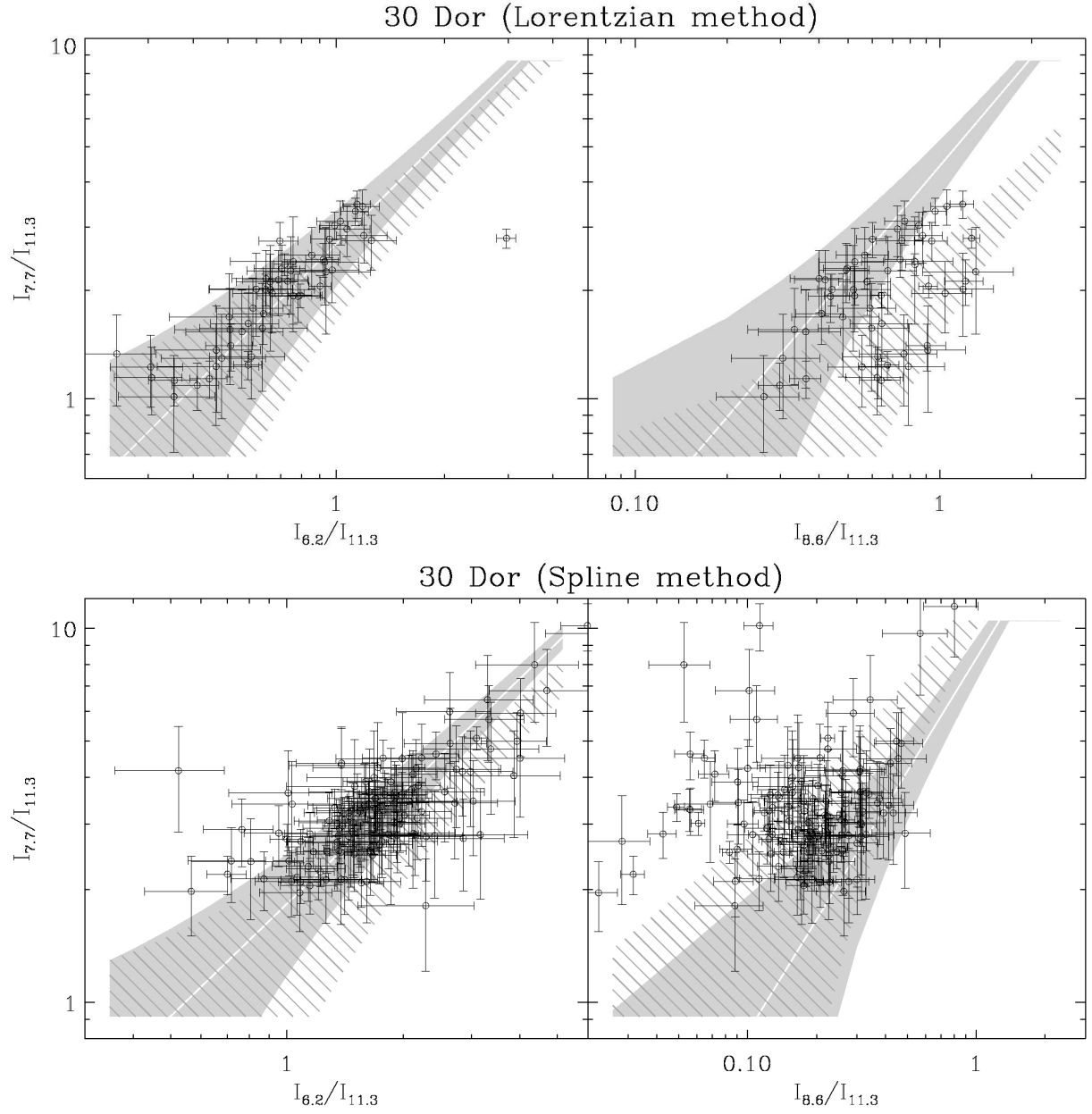


Fig. 28.— PAH band ratios within 30 Doradus. The same symbol conventions are adopted as in Fig. 7.

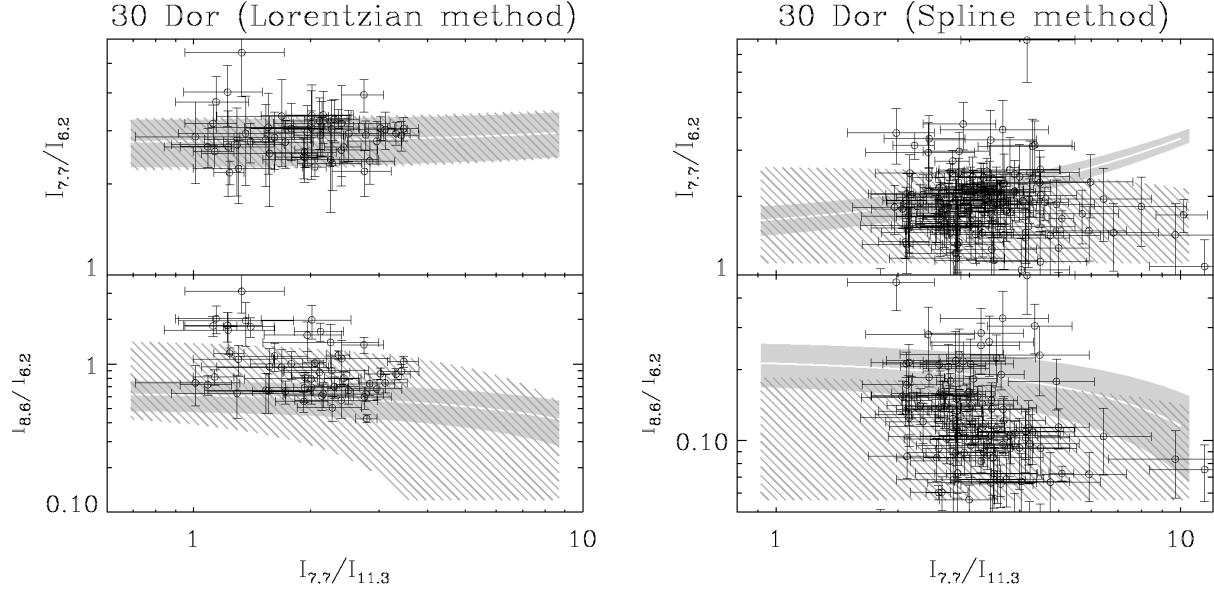


Fig. 29.— PAH band ratios within 30 Doradus (continued).

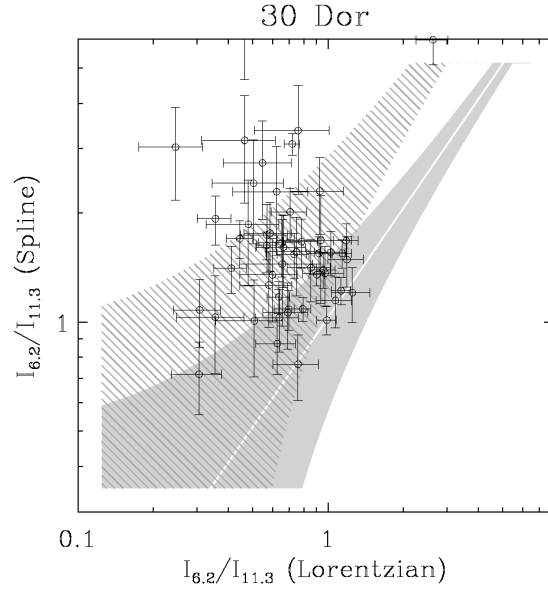


Fig. 30.— Comparison between the two methods in 30 Doradus. The same symbol conventions are adopted as in Fig. 7.

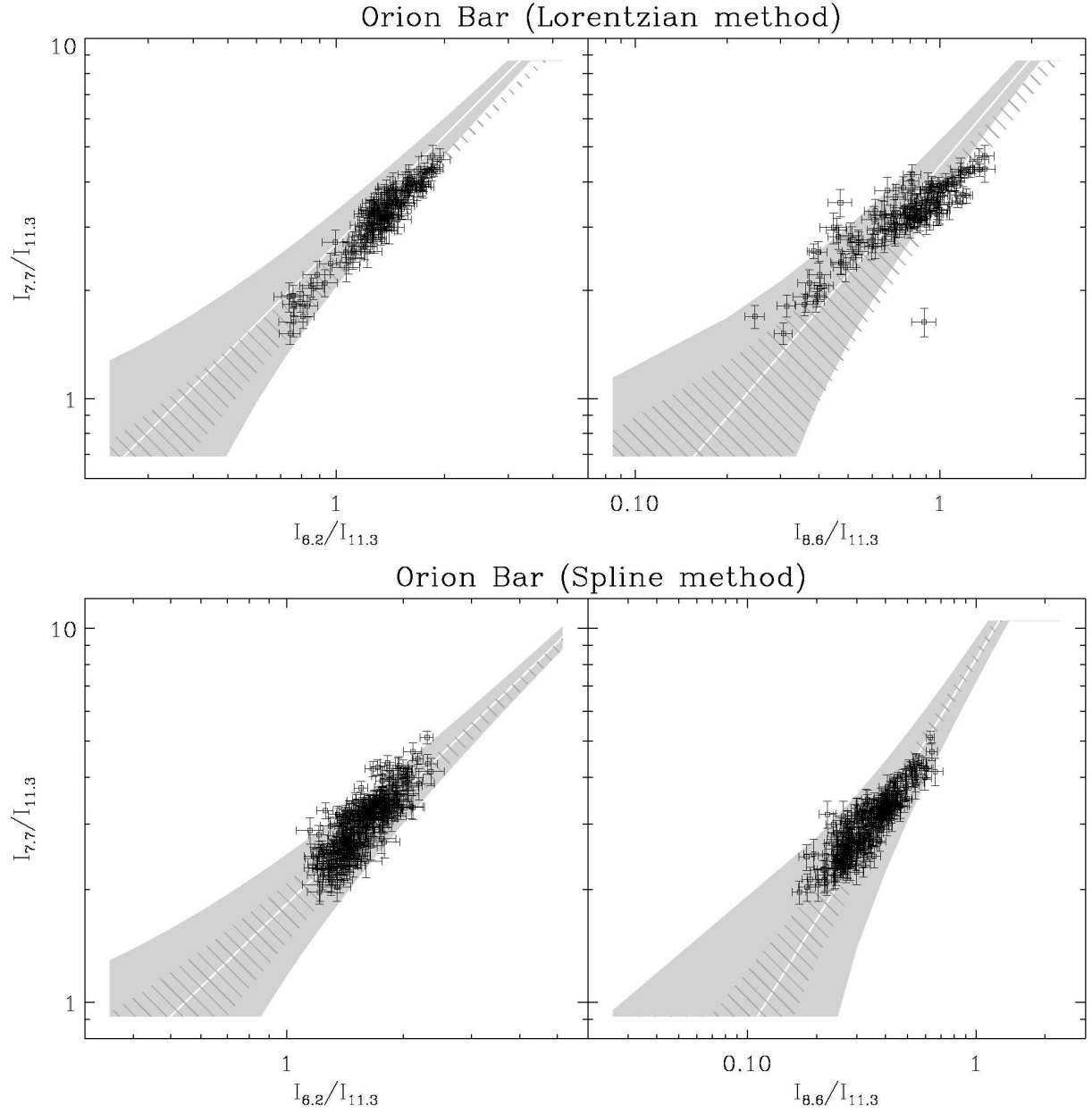


Fig. 31.— PAH band ratios within the Orion bar. The same symbol conventions are adopted as in Fig. 7.

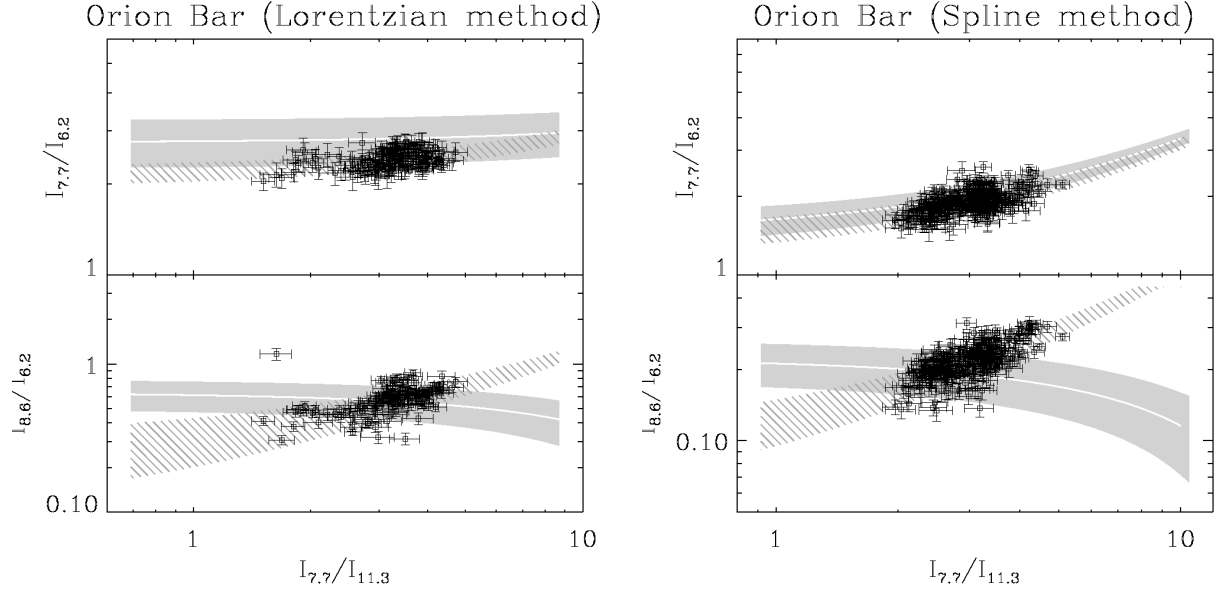


Fig. 32.— PAH band ratios within Orion bar (continued).

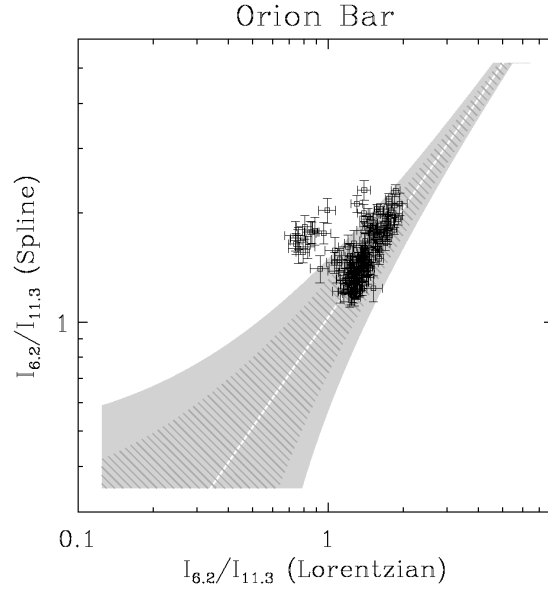


Fig. 33.— Comparison between the two methods in Orion bar. The same symbol conventions are adopted as in Fig. 7.

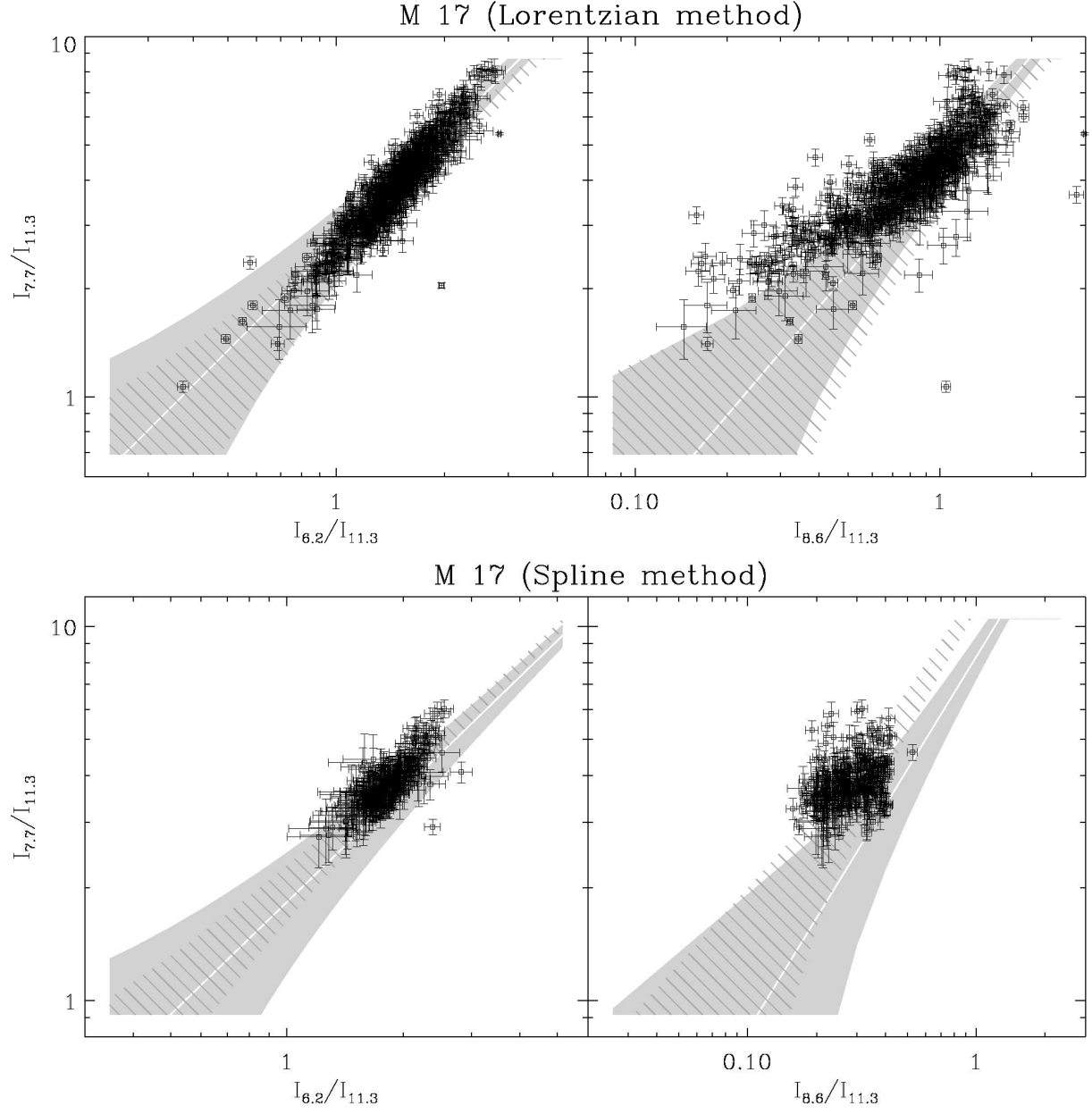


Fig. 34.— PAH band ratios within M 17. The same symbol conventions are adopted as in Fig. 7.

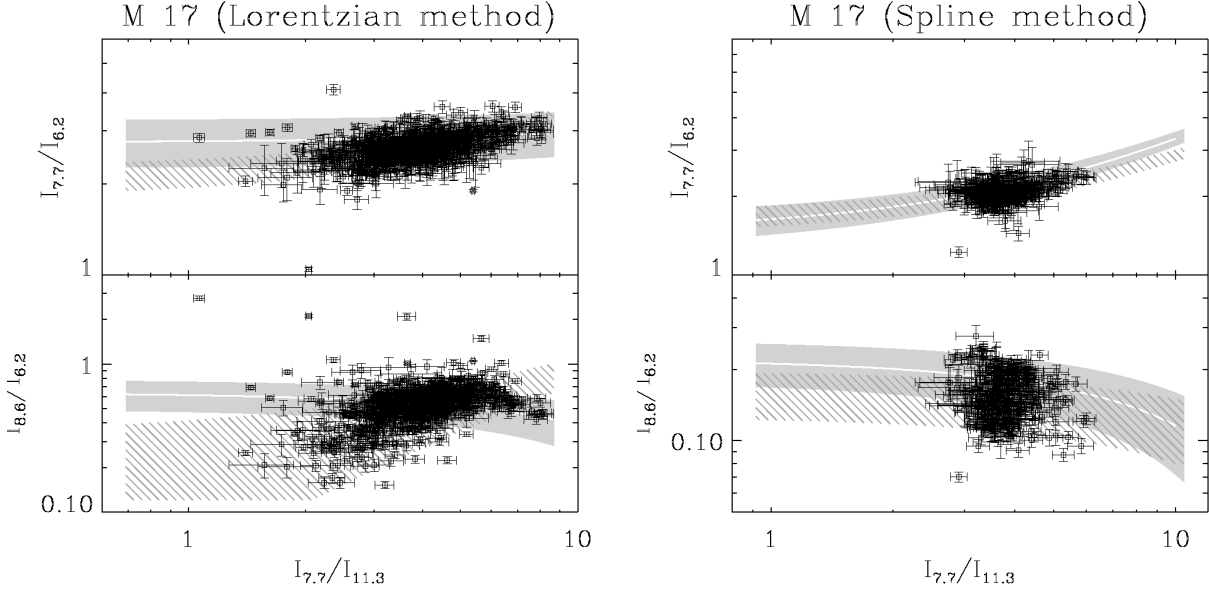


Fig. 35.— PAH band ratios within M 17 (continued).

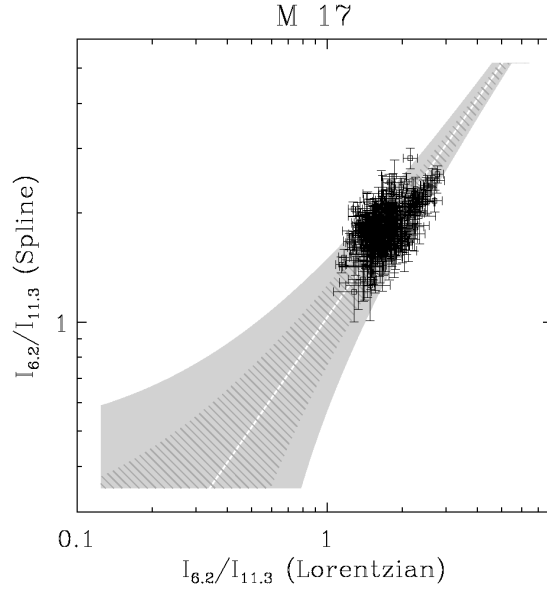


Fig. 36.— Comparison between the two methods in M 17. The same symbol conventions are adopted as in Fig. 7.

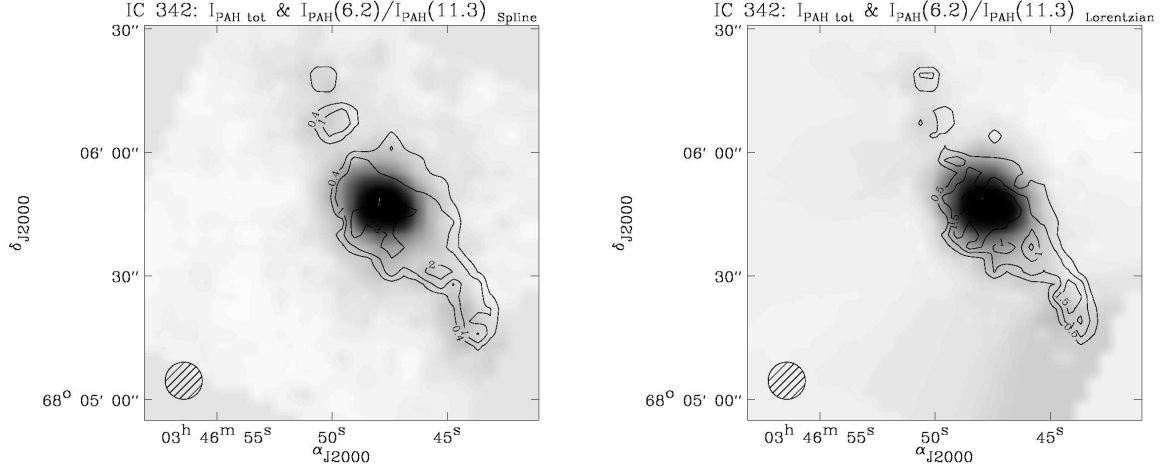


Fig. 37.— Spatial distribution of the PAHs in IC 342. For each method, the image is the total PAH intensity, and the contours are the $I_{6.2}/I_{11.3}$ ratio. The shaded circle indicates the beam size.

We are grateful to Lou Allamandola and Henrik Spoon for in-depth useful discussions and detailed comments on our work. We thank the anonymous referee of this paper for comments that improved its quality. This work was performed, while F. G. held a National Research Council research associateship award at NASA GSFC, and later a NASA Postdoctoral Program fellowship at NASA GSFC. This study is based essentially on observations made with ISO, an ESA project with instruments funded by ESA Member States (especially the PI countries: France, Germany, the Netherlands and the United Kingdom) and with the participation of ISAS and NASA. It is also based in part on observations made with the *Spitzer Space Telescope*, which is operated by the Jet Propulsion Laboratory, California Institute of Technology under a contract with NASA.

Facilities: ISO (CAM), ISO (SWS), Spitzer (IRS).

REFERENCES

- Abergel, A., Bernard, J. P., Boulanger, F., et al. 2002, *A&A*, 389, 239
- Abergel, A., Verstraete, L., Joblin, C., Laureijs, R., & Miville-Deschênes, M.-A. 2005, *Space Science Reviews*, 119, 247
- Allain, T., Leach, S., & Sedlmayr, E. 1996, *A&A*, 305, 616

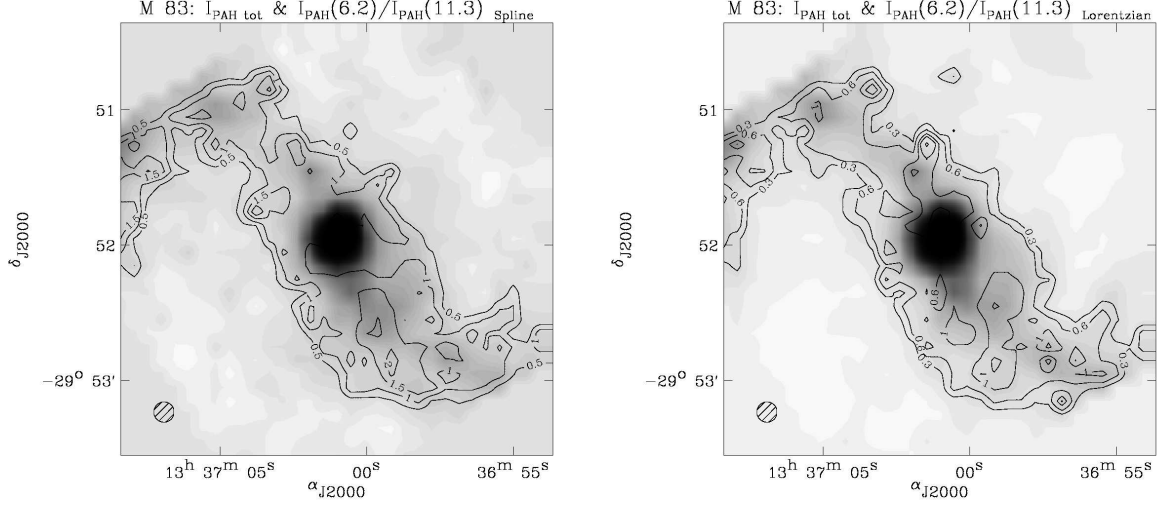


Fig. 38.— Spatial distribution of the PAHs in M 83. For each method, the image is the total PAH intensity, and the contours are the $I_{6.2}/I_{11.3}$ ratio. The shaded circle indicates the beam size.

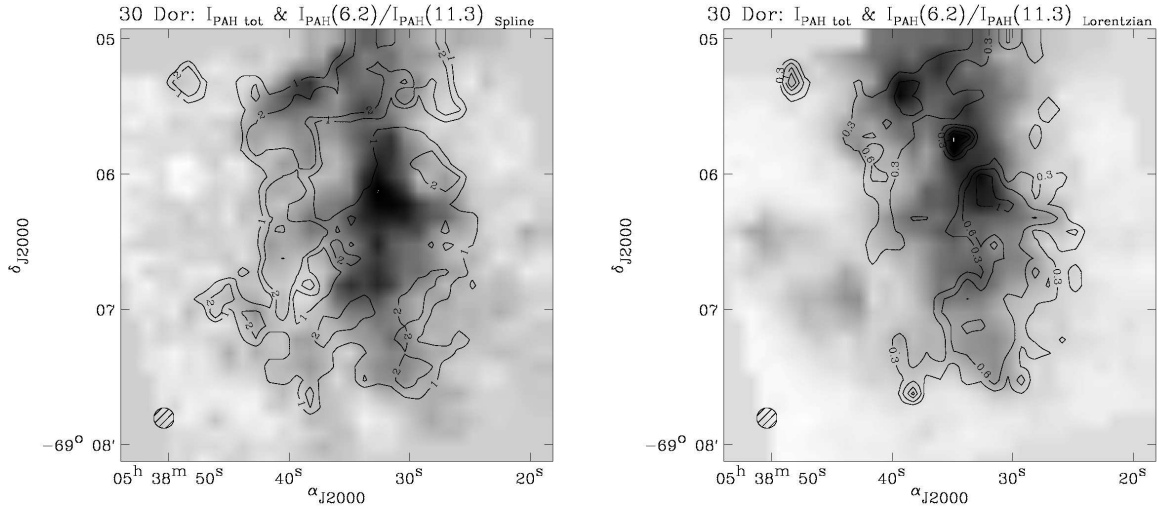


Fig. 39.— Spatial distribution of the PAHs in 30 Doradus. For each method, the image is the total PAH intensity, and the contours are the $I_{6.2}/I_{11.3}$ ratio. The shaded circle indicates the beam size.

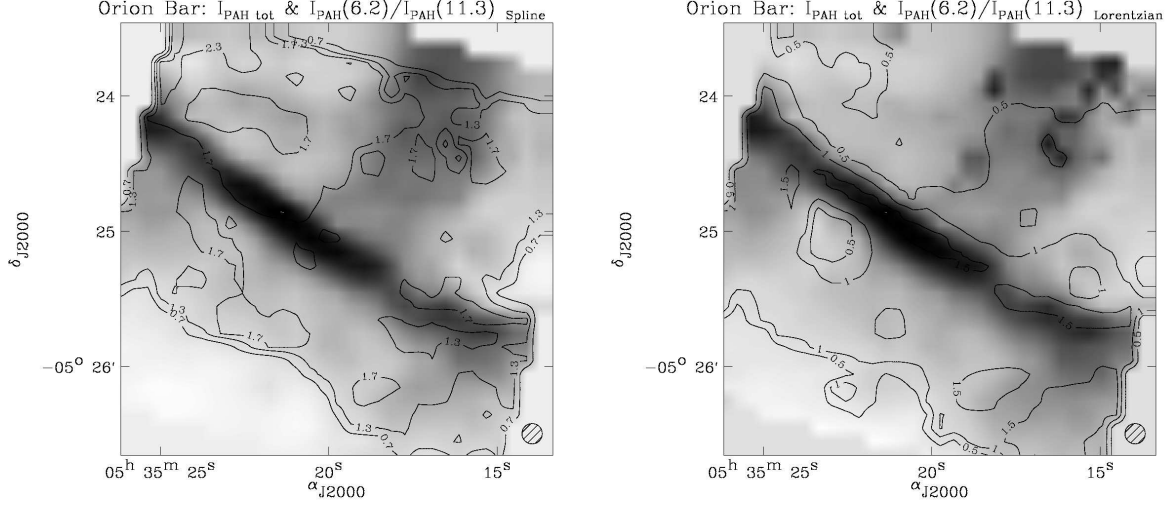


Fig. 40.— Spatial distribution of the PAHs in Orion bar. For each method, the image is the total PAH intensity, and the contours are the $I_{6.2}/I_{11.3}$ ratio. The shaded circle indicates the beam size.

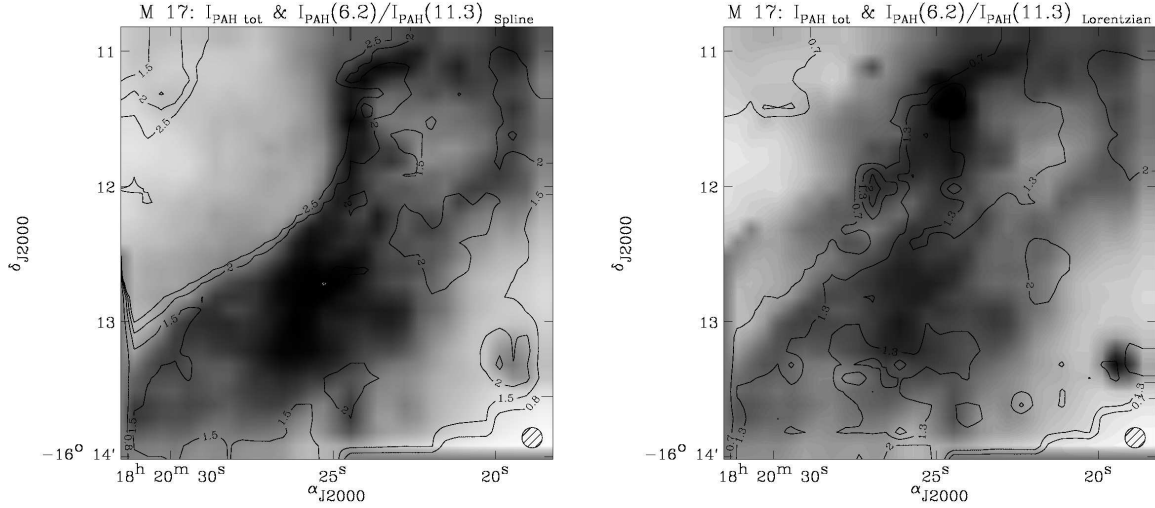


Fig. 41.— Spatial distribution of the PAHs in M 17. For each method, the image is the total PAH intensity, and the contours are the $I_{6.2}/I_{11.3}$ ratio. The shaded circle indicates the beam size.

- Allamandola, L. J., Hudgins, D. M., & Sandford, S. A. 1999, *ApJ*, 511, L115
- Allamandola, L. J., Tielens, A. G. G. M., & Barker, J. R. 1985, *ApJ*, 290, L25
- Allamandola, L. J., Tielens, G. G. M., & Barker, J. R. 1989, *ApJS*, 71, 733
- Alloin, D., Collin-Souffrin, S., & Joly, M. 1979, *A&AS*, 37, 361
- Bakes, E. L. O. & Tielens, A. G. G. M. 1994, *ApJ*, 427, 822
- Bauschlicher, Jr., C. W. 2002, *ApJ*, 564, 782
- Beirão, P., Brandl, B. R., Devost, D., et al. 2006, *ApJ*, 643, L1
- Bergvall, N., Masegosa, J., Östlin, G., & Cernicharo, J. 2000, *A&A*, 359, 41
- Biviano, A., Sauvage, M., Gallais, P., et al. 1998, The ISOCAM dark current calibration report, Tech. rep., ESA/ISO Data Centre
- Blommaert, J. A. D. L., Cami, J., Szczerba, R., & Barlow, M. J. 2005, *Space Science Reviews*, 119, 215
- Boselli, A., Lequeux, J., & Gavazzi, G. 2002, *A&A*, 384, 33
- Boulanger, F., Boissel, P., Cesarsky, D., & Ryter, C. 1998, *A&A*, 339, 194
- Brandl, B. R., Bernard-Salas, J., Spoon, H. W. W., et al. 2006, *ApJ*, 653, 1129
- Brandl, B. R., Devost, D., Higdon, S. J. U., et al. 2004, *ApJS*, 154, 188
- Bregman, J. & Temi, P. 2005, *ApJ*, 621, 831
- Bresolin, F., Garnett, D. R., & Kennicutt, Jr., R. C. 2004, *ApJ*, 615, 228
- Cesarsky, C. J., Abergel, A., Agnese, P., et al. 1996a, *A&A*, 315, L32
- Cesarsky, D., Jones, A. P., Lequeux, J., & Verstraete, L. 2000, *A&A*, 358, 708
- Cesarsky, D., Lequeux, J., Abergel, A., et al. 1996b, *A&A*, 315, L309
- Chanial, P. 2003, PhD thesis, University of Paris VII
- Cherchneff, I., Le Teuff, Y. H., Williams, P. M., & Tielens, A. G. G. M. 2000, *A&A*, 357, 572
- Compiègne, M., Abergel, A., Verstraete, L., et al. 2007, *A&A*, 471, 205

- Coulais, A. & Abergel, A. 2000, *A&AS*, 141, 533
- Dartois, E., Muñoz Caro, G. M., Deboffle, D., Montagnac, G., & D’Hendecourt, L. 2005, *A&A*, 432, 895
- Désert, F.-X., Boulanger, F., & Puget, J. L. 1990, *A&A*, 237, 215
- Draine, B. T., Dale, D. A., Bendo, G., et al. 2007, *ApJ*, 663, 866
- Draine, B. T. & Li, A. 2001, *ApJ*, 551, 807
- Draine, B. T. & Li, A. 2007, *ApJ*, 657, 810
- Dudley, C. C. & Wynn-Williams, C. G. 1997, *ApJ*, 488, 720
- Dufour, R. J., Shields, G. A., & Talbot, Jr., R. J. 1982, *ApJ*, 252, 461
- Duley, W. W. & Williams, D. A. 1981, *MNRAS*, 196, 269
- Dutil, Y. & Roy, J.-R. 1999, *ApJ*, 516, 62
- Dwek, E., Arendt, R. G., Fixsen, D. J., et al. 1997, *ApJ*, 475, 565
- Elbaz, D., Le Floc’h, E., Dole, H., & Marcillac, D. 2005, *A&A*, 434, L1
- Engelbracht, C. W., Gordon, K. D., Rieke, G. H., et al. 2005, *ApJ*, 628, L29
- Fioc, M. & Rocca-Volmerange, B. 1997, *A&A*, 326, 950
- Flagey, N., Boulanger, F., Verstraete, L., et al. 2006, *A&A*, 453, 969
- Fuente, A., Rodriguez-Franco, A., & Martin-Pintado, J. 1996, *A&A*, 312, 599
- Galliano, F. 2004, PhD thesis, University of Paris XI, <http://tel.archives-ouvertes.fr/tel-00122609>
- Galliano, F. 2007, in *Studying Galaxy Evolution with Spitzer and Herschel*, astro-ph/0610852, in press
- Galliano, F., Dwek, E., & Chianal, P. 2008, *ApJ*, 672, 214
- Galliano, F., Madden, S. C., Jones, A. P., Wilson, C. D., & Bernard, J.-P. 2005, *A&A*, 434, 867
- Galliano, F., Madden, S. C., Jones, A. P., et al. 2003, *A&A*, 407, 159

- Genzel, R., Lutz, D., Sturm, E., et al. 1998, *ApJ*, 498, 579
- Gonzalez-Delgado, R. M., Perez, E., Diaz, A. I., et al. 1995, *ApJ*, 439, 604
- Heckman, T. M., Robert, C., Leitherer, C., Garnett, D. R., & van der Rydt, F. 1998, *ApJ*, 503, 646
- Higdon, S. J. U., Devost, D., Higdon, J. L., et al. 2004, *PASP*, 116, 975
- Hollenbach, D. J. & Tielens, A. G. G. M. 1997, *ARA&A*, 35, 179
- Hony, S., Van Kerckhoven, C., Peeters, E., et al. 2001, *A&A*, 370, 1030
- Houck, J. R., Charmandaris, V., Brandl, B. R., et al. 2004a, *ApJS*, 154, 211
- Houck, J. R., Roellig, T. L., van Cleve, J., et al. 2004b, *ApJS*, 154, 18
- Houck, J. R., Soifer, B. T., Weedman, D., et al. 2005, *ApJ*, 622, L105
- Izotov, Y. I. & Thuan, T. X. 1998, *ApJ*, 500, 188
- Joblin, C., Leger, A., & Martin, P. 1992, *ApJ*, 393, L79
- Joblin, C., Tielens, A. G. G. M., Geballe, T. R., & Wooden, D. H. 1996, *ApJ*, 460, L119
- Jochims, H. W., Baumgärtel, H., & Leach, S. 1999, *ApJ*, 512, 500
- Justtanont, K., Tielens, A. G. G. M., Skinner, C. J., & Haas, M. R. 1997, *ApJ*, 476, 319
- Kaneda, H., Onaka, T., & Sakon, I. 2007, *ApJ*, 666, L21
- Kessler, M. F., Steinz, J. A., Anderegg, M. E., et al. 1996, *A&A*, 315, L27
- Kim, H.-S. & Saykally, R. J. 2002, *ApJS*, 143, 455
- Kobulnicky, H. A. & Johnson, K. E. 1999, *ApJ*, 527, 154
- Kobulnicky, H. A. & Skillman, E. D. 1997, *ApJ*, 489, 636
- Kraemer, K. E., Sloan, G. C., Bernard-Salas, J., et al. 2006, *ApJ*, 652, L25
- Langhoff, S. 1996, *Journal of Physical Chemistry*, 100, 2819
- Laor, A. & Draine, B. T. 1993, *ApJ*, 402, 441
- Laurent, O., Mirabel, I. F., Charmandaris, V., et al. 2000, *A&A*, 359, 887

- Léger, A. & Puget, J. L. 1984, *A&A*, 137, L5
- Li, A. & Draine, B. T. 2001, *ApJ*, 554, 778
- Madden, S. C., Galliano, F., Jones, A. P., & Sauvage, M. 2006, *A&A*, 446, 877
- Mallocci, G., Joblin, C., & Mulas, G. 2007, *A&A*, 462, 627
- Mas-Hesse, J. M. & Kunth, D. 1999, *A&A*, 349, 765
- Mathis, J. S. 1990, *ARA&A*, 28, 37
- Mathis, J. S., Mezger, P. G., & Panagia, N. 1983, *A&A*, 128, 212
- Mattioda, A. L., Allamandola, L. J., & Hudgins, D. M. 2005a, *ApJ*, 629, 1183
- Mattioda, A. L., Hudgins, D. M., & Allamandola, L. J. 2005b, *ApJ*, 629, 1188
- O’Halloran, B., Satyapal, S., & Dudik, R. P. 2006, *ApJ*, 641, 795
- Otte, B., Reynolds, R. J., Gallagher, III, J. S., & Ferguson, A. M. N. 2001, *ApJ*, 560, 207
- Peeters, E., Allamandola, L. J., Hudgins, D. M., Hony, S., & Tielens, A. G. G. M. 2004a, in ASP Conf. Ser. 309: *Astrophysics of Dust*, ed. A. N. Witt, G. C. Clayton, & B. T. Draine, 141
- Peeters, E., Hony, S., Van Kerckhoven, C., et al. 2002a, *A&A*, 390, 1089
- Peeters, E., Martín-Hernández, N. L., Damour, F., et al. 2002b, *A&A*, 381, 571
- Peeters, E., Spoon, H. W. W., & Tielens, A. G. G. M. 2004b, *ApJ*, 613, 986
- Pérez-Montero, E. & Díaz, A. I. 2003, *MNRAS*, 346, 105
- Persi, P., Cesarsky, D., Marenzi, A. R., et al. 1999, *A&A*, 351, 201
- Pilyugin, L. S., Vílchez, J. M., & Contini, T. 2004, *A&A*, 425, 849
- Povich, M. S., Stone, J. M., Churchwell, E., et al. 2007, *ApJ*, 660, 346
- Ravindranath, S. & Prabhu, T. P. 2001, *Ap&SS*, 276, 593
- Reach, W. T., Boulanger, F., Contursi, A., & Lequeux, J. 2000, *A&A*, 361, 895
- Roche, P. F., Aitken, D. K., & Smith, C. H. 1989, *MNRAS*, 236, 485
- Roussel, H., Vigroux, L., Bosma, A., et al. 2001, *A&A*, 369, 473

- Roy, J.-R. & Walsh, J. R. 1997, MNRAS, 288, 715
- Sakamoto, K., Okumura, S. K., Ishizuki, S., & Scoville, N. Z. 1999, ApJS, 124, 403
- Schaerer, D., Guseva, N. G., Izotov, Y. I., & Thuan, T. X. 2000, A&A, 362, 53
- Schutte, W. A., Tielens, A. G. G. M., & Allamandola, L. J. 1993, ApJ, 415, 397
- Sellgren, K. 1984, ApJ, 277, 623
- Smith, J. D. T., Draine, B. T., Dale, D. A., et al. 2007, ApJ, 656, 770
- Sofia, U. J., Lauroesch, J. T., Meyer, D. M., & Cartledge, S. I. B. 2004, ApJ, 605, 272
- Spoon, H. W. W., Keane, J. V., Tielens, A. G. G. M., et al. 2002, A&A, 385, 1022
- Starck, J. L., Abergel, A., Aussel, H., et al. 1999, A&AS, 134, 135
- Steiman-Cameron, T. Y., Haas, M. R., Tielens, A. G. G. M., & Burton, M. G. 1997, ApJ, 478, 261
- Storchi-Bergmann, T., Kinney, A. L., & Challis, P. 1995, ApJS, 98, 103
- Tauber, J. A., Tielens, A. G. G. M., Meixner, M., & Foldsmith, P. F. 1994, ApJ, 422, 136
- Tielens, A. G. G. M. 2005, The Physics and Chemistry of the Interstellar Medium (The Physics and Chemistry of the Interstellar Medium, by A. G. G. M. Tielens, pp. . ISBN 0521826349. Cambridge, UK: Cambridge University Press, 2005.)
- Tielens, A. G. G. M. & Allamandola, L. J. 1987, in ASSL Vol. 134: Interstellar Processes, ed. D. J. Hollenbach & H. A. Thronson, Jr., 397–469
- Tielens, A. G. G. M., Meixner, M. M., van der Werf, P. P., et al. 1993, Science, 262, 86
- van Diedenhoven, B., Peeters, E., Van Kerckhoven, C., et al. 2004, ApJ, 611, 928
- Verma, A., Charmandaris, V., Klaas, U., Lutz, D., & Haas, M. 2005, Space Science Reviews, 119, 355
- Vermeij, R., Peeters, E., Tielens, A. G. G. M., & van der Hulst, J. M. 2002, A&A, 382, 1042
- Verstraete, L., Pech, C., Moutou, C., et al. 2001, A&A, 372, 981
- Webster, B. L. & Smith, M. G. 1983, MNRAS, 204, 743
- Werner, M. W., Roellig, T. L., Low, F. J., et al. 2004, ApJS, 154, 1

- Wu, Y., Charmandaris, V., Hao, L., et al. 2006, ApJ, 639, 157
- Wyrowski, F., Schilke, P., Hofner, P., & Walmsley, C. M. 1997, ApJ, 487, L171+
- Yan, L., Chary, R., Armus, L., et al. 2005, ApJ, 628, 604
- Zaritsky, D., Kennicutt, Jr., R. C., & Huchra, J. P. 1994, ApJ, 420, 87
- Zubko, V., Dwek, E., & Arendt, R. G. 2004, ApJS, 152, 211